MSc. Francis Twumasi-Boateng

Real-time radiography for observation of crack growth during welding

Die vorliegende Arbeit entstand an der Bundesanstalt für Materialforschung und -prüfung (BAM).

Real-time radiography for observation of crack growth during welding

Dissertation

zur Erlangung des akademischen Grades

Doktoringenieur

(Dr.-Ing.)

von M.Sc. Francis Twumasi-Boateng

geb. am 24. Juli 1979

aus Kumasi, Ghana

genehmigt durch die Fakultät für Maschinenbau
der Otto-von-Guericke-Universität Magdeburg

Gutachter:
Prof. Dr.-Ing. habil. Thomas Kannengießer
Prof. Dr.-Ing. Christian Boller
Dr. rer. nat. Uwe Zscherpel

Promotionskolloquium am 11. Juni 2021

Boateng, Francis Twumasi:
Real-time radiography for observation of crack growth during welding
Otto-von-Guericke-Universität Magdeburg, 2021

Learn from yesterday, live for today, hope for tomorrow.
The important thing is to not stop questioning.

Albert Einstein.

Dedicated to my parent

Abbreviations and Symbols

Symbols	Units	Parameter
$\boldsymbol{E}$	*keV*	X-ray photon energy
$\boldsymbol{I}$	*Gy*	Transmitted X-ray Intensity (dose)
$\boldsymbol{I_o}$	*Gy*	Initial X-ray intensity (dose)
$\boldsymbol{\mu}$	mm^{-1}	Linear attenuation coefficient
$\boldsymbol{\mu_{eff}}$	mm^{-1}	Effective attenuation coefficient
$\boldsymbol{l}$	mm	Wall thickness
$\boldsymbol{t}$	sec	Time
$\boldsymbol{\rho}$	kgm^{-3}	Material Density
$\frac{\boldsymbol{\mu}}{\boldsymbol{\rho}}$	m^2kg^{-1}	Mass attenuation coefficient
$\boldsymbol{U_i}$	mm	Inherent detector unsharpness
$\boldsymbol{U_g}$	mm	Geometric unsharpness (Penumbra)
$\boldsymbol{U_T}$	mm	Total image unsharpness of detector
$\boldsymbol{U_{Im}}$	mm	Image unsharpness of object
HI	*kJ/mm*	Heat Input
$\boldsymbol{ODD}$	mm	Object Detector Distance
$\boldsymbol{SDD}$	mm	Source Detector Distance
$\boldsymbol{SOD}$	mm	Source Object Distance
BTR	*K*	Brittle Temperature Range
$\boldsymbol{SR_b^{image}}$	*mm*	Image spatial basic resolution
$\boldsymbol{SR_b^{detector}}$	*mm*	Detector spatial basic resolution
$\boldsymbol{SR_b}$	*mm*	Basic spatial resolution
$\boldsymbol{f}$	*mm*	Focal spot size
AC	*A*	Alternating current
G	*K*	Thermal gradient
V	*m/s*	*Crack g*rowth rate
$\Delta\boldsymbol{T}$	*K*	Solidification temperature range

$\overline{V}_n$	*m/s*	*Crack* growth rate at the liquid-solid interface
$\overline{G}_{hkl}$	*K*	*T*hermal gradient along the dendrite growth direction
$\overline{G}_n$	*K*	Total thermal gradient direction
T_0	*°C*	Ambient temperature
K	$WK^{-1}m^{-1}$	Thermal conductivity
x, y, z	*mm*	Coordinate axes
α	m^2/s	Thermal diffusivity
LET	*keV/µm*	Linear energy transfer
2D		Two-dimensional data
$3D$		Three-dimensional data
A		Crack sensitivity
ASME		American Society of Mechanical Engineers
ASTM		American Society for Testing and Materials
BM		Base Material
CEN		European Committee for Standardization
CMOS		Complementary metal-oxide-semiconductor
CNR		Contrast–to–Noise Ratio
$CNR_N^{specific}$		*Specific normalised* contrast–to–noise ratio
CsI		Cesium Iodide scintillator
CT		Computed Tomography
DDA		Digital Detector Array
FZ		Fusion zone
GTA		Gas Tungsten Arc
GV		Grey Value
HAZ		Heat Affected Zone
IQI		Image quality indicator
HV	*kV*	X-ray tube high voltage
M		Magnification

Θ	Laminographic angle
PT	Perception threshold
RDG	Rappaz-Drezet-Gremaud diagram
SEM	Scanning Electron Microscope
$\boldsymbol{SNR}$	Signal –to – Noise Ratio
SR-CL	Synchrotron Radiation - Computed Laminography
SR-CT	Synchrotron Radiation - Computed Tomography
WM	Weld Material
$\boldsymbol{Z_{eff}}$	Effective atomic number

Zusammenfassung

Heißrisse sind ein bekanntes Phänomen während des Schweißens, das auf den sicheren Einsatz von Aluminium-Legierungen einen großen Einfluss hat. Die Neigung zur Heißrissbildung beeinflusst wesemtlich die Auswahl einer Legierung und ihre Schweißbarkeit. Heißrissbildung tritt vor allem in der „Mushy Zone“ auf, die den Übergang wischen dem festen und dem flüssigen Teil des Schweißbades darstellt. Hier erfährt die metallische Legierung thermische Ausdehnungen und Kontraktionen [1]. Im Laufe der Jahre wurden viele Theorien vorgeschlagen, um die Erstarrungsdynamik des Schweißbades zu erklären. Jedoch sind diese Untersuchungen qualitativer Natur. Inzwischen sind viele der Vorhersagemodelle nicht ausreichend genug aufgrund des Fehlens von quantitativen Informationen. Aus diesem Grunde ist es unerlässlich für eine zuverlässige und robuste quantitative Voraussage wichtige Fragen der Heißrissbildung zu beantworten, wie z.B. die Korrelation zwischen Schweißparametern und Rißbildung oder Rißwachstum und Rißlänge.

Das Ziel dieser Forschung war es, eine neuen experimentellen in-situ Ansatz bei der Untersuchung von Heißrißildung und -wachstum während des Schweißens einzuführen. Das wurde mit einem robusten Durchstrahlungsaufbau mit 40 ms Belichtungsdauer bei einer Bildrate von 10 Bildern pro Sekunde während des Schweißen erreicht. Mit einer konventionellen Minifokus-Röntgenquelle (YXLON Röntgenröhre Y.TU 225-D04) und einen digitalen Matrixdetektor mit 75 µm Pixelgröße (Dexela 1512) wurden sequentiell 2D-Projektionen erfasst, die während eines Wolfram-Inertgas-Schweißvorganges aufgenommen wureden. Fünf verschiedene Aluminiumlegierungen wurden untersucht.

In dieser Arbeit wurde eine koplanare laminographische Bildaufnahme verwendet, die eine lineare Translation von Schweißnaht und Detektor gemeinsam und parallel zur festen Röntgenquelle realisiert. Diese synchronisierte Bewegung von Schweißnaht und Detektor ermöglicht das geschweißte Material aus unterschiedlichen Winkeln relativ zur Schweißrichtung zu durchstrahlen. Schließlich wird die 3D-Information der untersuchten Schweißnaht mit einem koplanaren laminographischen 3D-Rekonstrutionsalgorithmus rekonstruiert.

Der laminographische 3D-Rekonstrutionsalgorithmus wurde realisiert durch eine Hochpass–Filtertechnik, die einen gefilterten Rückprojektionsalgorithmus mit Verschiebungsmittelung verwendet, um laminographische 3D-Rekonstruktionsdaten der Schweißnaht-Region zu erzeugen.

Eine Analyse der Rissverteilung wurde durchgeführt, indem die aufgenommenen 2D-Röntgenaufnahmen aller untersuchten Legierungen miteinander verglichen wurden. Weiterhin wurde untersucht, ob sich eine Beziehung zwischen Rissentstehung und Rissausbreitung

während des Schweißens ermitteln lässt. Temperaturverteilungsmessungen wurden mit Thermoelementen und einer Infrarotkamera aufgenommen. Das wurde verwendet, um die Temperaturverteilungen und Abkühlgeschwindigkeiten in der „Mushy Zone“ des Schweibades zu bestimmen. Risslängen und Schweißnaht-Unregelmäßigkeiten wie Porositäten und Einschlüsse wurden mittles 3D-Laminographie und Computertomographie gemessen. Das Ziel dieser Forschungsarbeit war, ein gründliches Verständnis der Erstarrungsrissbildung in Aluminium-Legierungen zu entwickeln.

Dieser In-situ-Ansatz eröffnet auch neue Möglichkeiten auf dem Gebiet der Heißriss-Forschung durch die Kombination von Informationen sowohl der Rissinitialisierung und ihrer Korrelation mit den Schweißparametern.

Abstract

Hot cracking is a known phenomenon during welding, which has a severe influence on the durability of aluminium alloys. The susceptibility of hot cracking plays a pivotal role in defining alloys weldability. Hot cracking mainly occurs at the mushy zone, this is the position between the solidus and liquation interface of the weld pool. The mushy zone is the region where the metallic alloy experiences thermal expansion and contraction [1]. Over the years, many theories have been proposed to demonstrate and explain the solidification dynamics of the weld pool. However, these investigations are qualitative in nature. Meanwhile, many of the prediction models are not adequate due to the lack of quantitative information. For this reason, it is imperative for a reliable and robust quantitative forecast to evaluate and characterize some of the prevailing questions of hot cracking. Notably, how hot cracking correlates to welding parameters for its crack growth and cracks length.

This research aims to introduce an in-situ observatory approach in the detection of hot crack formation and propagation during welding. The primary objective of this study was to develop a robust X-ray set-up with 40ms frame exposure at a frame rate of 10 frames/s during welding. This was achieved by using a conventional mini focus X-ray source (YXLON X-ray tube Y.TU 225-D04) and a 75 µm pixel size digital detector array (Dexela 1512). Sequential 2D radiographic projections were acquired for hot crack observation during single-pass gas tungsten arc welding. Five different aluminium alloys were investigated.

In this study, a coplanar laminographic imaging system was used, which realizes a linear translation of weld material and detector together and parallel to the fixed X-ray source. This synchronized motion of the weld material and the detector allows penetrating the weld material with different exposure angles relative to the welding direction. Finally, the 3D information of the investigated weld material can be reconstructed by a coplanar laminographic reconstruction algorithm.

The laminographic reconstruction algorithm was realized as a high-pass filter technique using a filtered back-projection algorithm with shift averaging of the related projections to generate a 3D laminographic reconstruction data of the weld region.

A study of crack distribution was conducted by comparison of the acquired 2D radiographs of all the alloys used in the research. Furthermore, a crack distribution analysis was carried out to determine the relationship between crack initiation and crack propagation during welding. Temperature distribution measurements were taken from thermocouple elements and an infra-red camera. These were used to determine the temperature distributions and cooling rates at the mushy zone of the weld pool. Crack lengths and weld imperfections such as porosity and inclusions were measured by 3D-laminography and computed tomography reconstructions.

The purpose of this research work was to develop an in-depth knowledge of the solidification cracking of aluminium alloys.

This in-situ approach was also aimed to open new possibilities into the field of hot crack research by combining information on both the crack initiation and its correlation to the welding parameters.

Table of Contents

1 Introduction

1.1 Background

The weldability of aluminium alloys is defined by their susceptibility to solidification cracking [1]. Depending upon the alloy chemical composition and welding conditions, cracks may form in the weld metal during solidification. Some alloys possess such a high cracking tendency that welding without cracking is not possible such as aluminium alloys with Magnesium (Mg) and Silicon (Si) base. The alloy composition is critical for the formation of solidification cracks caused by the grain structure of the aluminium alloy impinge on each other after welding. Solidification shrinkage and thermal contractions of the solidifying material may generate a rupture of the liquid film at the grain boundaries [2]. One other reason that can be attributed to this rupture is the critical strain rate within the Brittle Temperature Range (BTR) [3]. That forms part of the solidification range where hot cracks occur because of lack of ductility within the mushy zone, where liquid fraction gets into a Brittle Temperature Range (BTR). The BTR is the temperature range whereby a coherent dendrite network is established during welding which influences the formation of solidification cracks [3, 4].

Hot cracking is defined as solidification cracks formed within the solidus-liquation interface of the weld metal at high temperatures. This is the region where the welded metal has coherence, becomes very brittle, and causes a decrease in the aluminium alloy ductility. The decrease of cohesion between the alloy grain boundaries initiates hot cracks, which are caused as a result of thermal contractions [5]. At this point, the aluminium alloy experiences critical strains that are responsible for crack initiation and subsequent crack growth. The notable theory by Rappaz Drezet-Gremaud (RDG) describes the pressure drop and strain rate at the liquid phase of the mushy zone as a result of insufficient liquid feeding that leads to solidification cracking [4]. Moreover, other factors to solidification cracking are temperature distribution and chemical composition of the aluminium alloy in the liquid phase [5]. These factors influence the solidification cracking behaviour of the aluminium alloy.

These aforementioned characteristics and influencing factors of solidification cracking in the aluminium alloy by hot cracking remain a major problem in welding technology. However, none of these existing criteria can provide the answers on whether the hot crack will occur or not and the extent of cracking in terms of position, length and shape of the crack.

The purpose of this study is to outline the requirements for hot cracking manifestation with an existing test such as Houldcroft and bead-on-plate tests [6, 7]. This will include the

mechanisms of nucleation, propagation of hot cracking and in-situ observation of solidification cracks during welding.

In-situ observations of the heat-affected zone of the weld pool were carried out with a conventional X-ray source and the adoption of the coplanar laminographic reconstruction method. The conventional X-ray source is easily accessible, robust and has large scanning angles coupled with high photon flux [8, 9]. Whereas, the laminographic method has the advantage of in-situ observation without cross-sectioning of the welded materials.

The in-situ observations of solidification crack formation have the advantage to relate the occurring events to post-mortem observations of crack surface features. To study these effects in real-time, a system is required for the observation of crack growth formation.

The motivation of this thesis is to develop a robust system for real-time observation of hot crack formation and propagation. This is to enable the visualization of crack formation (i.e. crack depth and crack morphology) and provide an understanding of crack propagation on both the surface and within the welded material during welding. Furthermore, the results of computed tomography imaging and laminographic 3D-reconstructions will be compared to ascertain the differences in crack lengths and weld inclusions such as porosity.
The purpose of the in-situ approach is to look into new possibilities in the field of hot crack research by having direct information on both the crack initiation and its correlation to the welding parameters and temperature distribution.

1.2 Thesis Outline

This work is structured into eight chapters as follows: Chapter 2 introduces the scientific background of radiology and its interaction with aluminium alloys. The interaction of X-rays and matter by absorption and scattering are discussed resulting in the radiographic image.

Chapter 3 focuses on the fundamental concepts of welding, the characteristics of aluminium alloys on the resulting seam during welding. The influencing factors such as welding parameters and alloy composition are also discussed, which had an integral impact on solidification cracking and flaw evolution during welding. The subject of crack susceptibility is addressed also, with a focus on the phenomenon of hot cracking.

A general overview of existing studies are discussed, for example, research works carried on the observation of crack initiation and propagation with the application of other radiography sources, i.e. neutron and synchrotron are also discussed in chapter 4. The use of digital radiography, acquisition schemes and compensation principles are also looked at in this chapter.

Chapter 5 introduces the concept of laminographic principles by looking at the types of laminographic scanning geometries and their respective advantages to this research. An in-depth description of the adopted laminographic geometry and the mathematical formulation that governs it are explained. The projection technique and its reconstruction algorithm are also addressed in this section.

An introduction to the “shift and-add” filtered back-projection reconstruction method is highlighted in this chapter. This mathematical process generates 3D volumes from the X-ray projection data acquired at different angles during scanning.

The adoption of solidification crack tests such as the Houldcroft test (HCT) and the bead–on-plate test for enabling crack formation during welding is introduced in chapter 6. The translation manipulator to achieve co-planar laminographic scans are also discussed. The correlation of welding speed and the determination of image quality with interest in movement unsharpness are all presented in this chapter.

Chapter 7 summarizes the results obtained from the Houldcroft test (HCT, [40]) and bead-on-plate (BOP, [34]) tests. Further studies are performed to show the influence of strain rates on the Houldcroft test (HCT). The 2D radiographic data obtained during welding are analysed with ImageJ crack tracking tool for crack propagation.

The analysis of the co-planar laminographic reconstructions are presented here and its relation to computed tomography data are discussed. Further studies into weld imperfections such as porosity from the laminographic and computed tomographic data are also carried out in this chapter. The real-time weld 2D and post-weld 3D models are adopted to describe the different damage evolution of the aluminium alloy with the application of BAM TomoPlan software (a programme used for the laminographic reconstruction).

Chapter 8 addresses the general conclusions for all the experimental data acquired and an out-look at possible future work.

2 Scientific Background on Industrial Radiography

Industrial radiographic inspections have been utilized for many years for quality control and assurance of various products. However, the use of digital radiography has recently been implemented in sectors such as medicine, aerospace, automotive and petrochemical industries etc. Digital radiography for non-destructive tests has a lot of benefits such as its excellent image quality, cost reduction due to the elimination of chemical processors and maintenance for radiographic films developments.

The application of radiographic inspection techniques plays a major role in the quantitative determination of internal flaws in an inspected material.

2.1 Historical milestones and developments of industrial radiography

There has been numerous innovative applications and techniques being introduced after the discovery of X-rays by Dr Wilhelm Conrad Roentgen [8]. He discovered that, if an object of variable density is positioned between an X-ray source with a detector and irradiated with X-rays, a contrast image called a radiograph is produced [9]. The earliest radiograph of Bertha Roentgen's hand clearly showed the contrast between bones. This discovery laid the foundation for NDT imaging applications till today [10].

The X-ray tube is composed of a vacuum tube that consists of anode and cathode that generates X-ray radiation [9, 10]. The X-rays are generated when a fast-accelerated electron beam emitted from the cathode filament collides with the outer electrons of the anode. When the emitted electron reaches the anode, it transfers most of its energy to the atoms of the anode target material by ionization and excitation [11, 12]. The de-acceleration of electrons inside the anode generates X-rays also known as "Bremsstrahlung" as illustrated in Fig. 1.

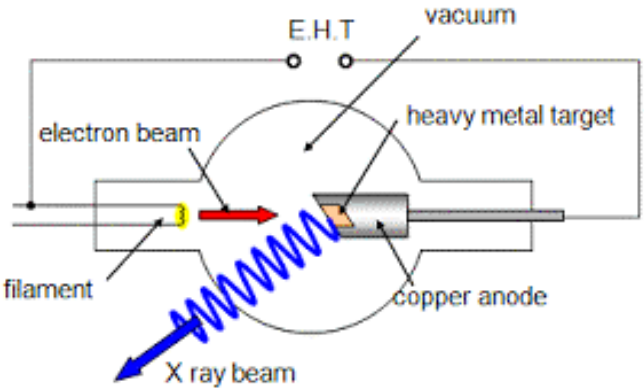

Figure 1: Schematic of an X-ray tube [11]

X-ray radiation has higher frequencies and shorter wavelengths than light and radio waves [10, 12]. The X-ray radiation is emitted as photons and each quantum of the photon emitted has a well-defined energy E, expressed by Max Planck's equation as.

$$\mathrm{E} = \mathrm{hv} \tag{2.1}$$

As h is Planck's constant and v is the frequency of radiation.

The X-ray radiation is a continuous spectrum, with the maximum photon energy depending on the electrons striking the anode and the high voltage generator [8, 11]. The shape of the spectrum also depends on the inherent filtration material of the X-ray tube window. The shortest wavelength of the spectrum is expressed as:

$$\lambda[nm] = \frac{1.234}{\mathrm{E[keV]}} \tag{2.2}$$

The X-ray quantum energy is dependent on the wavelengths λ, which classifies the type of X-ray emitted. For instance, an X-ray with a shorter wavelength of less than 0.1 nm (or E > 10 keV) is classified as hard X-rays while longer wavelengths are known as soft X-rays. These photons are electromagnetic radiation with zero mass, zero charges and velocity to the speed of light [9, 12]. Due to the electrical neutral nature, photons do not steadily lose their energy through coulombic interactions with the atomic electrons. Rather the photons travel a considerable distance before undergoing an interaction, which leads to either partial or total transfer of photon energy to the material. These photon energy transfer or energy loss

mechanisms are categorized as the Photoelectric effect, Compton effect and Pair production [21].

2.2 Photoelectric effect

The Photoelectric effect is the absorption of photons by an atom. This occurs when photons interact with a bound electron. The photon is completely absorbed and ejects an electron with kinetic energy, E_{e^-}. This corresponds to the photon energy hv and the electrons binding energy E_b [21, 22]. As expressed in Eqn.2.3.

$$\mathrm{E_{e^-}} = hv - \mathrm{E_b} \tag{2.3}$$

With Planck constant h and frequency of the absorbed photon v.

The electron-hole created in the inner atomic shell is filled by an electron of the outer shell, which produces fluorescence radiation or the electron escapes from the shell directly. This is known as the Auger electron [22, 23]. The energy range for the occurrence of the photoelectric effect is about 200keV to 10MeV.

2.3 Compton effect

Compton effect is the collision between a photon and a loosely bound outer-shell orbital electron of an atom. In the Compton effect, because the incident photon energy greatly exceeds the binding energy of the electron to the atom, this occurs as a result of a collision between the photon and a “free” electron. However, when part of the photon energy is absorbed in a collision and the photon travels further with reduced energy [22, 23]. The emitted photon leaves in a direction different from that of the original photon, which is also commonly referred to as Compton scattering. The energy difference between the incident and the scattered photon [19, 21, 23] is expressed as

$$E_{e^-} = hv - hv^- \tag{2.4}$$

The frequency of the incident and scattered photon is v and v^- respectively. The quasi-free photon will also be deflected from the angle of incidence and eject from the collision at lower

energies is known as backscattering radiation. The energy range of the quasi-free scattered photon is between 100 KeV and 10 MeV [19, 21]. This is the energy range where the quasi-free photon experiences an incoherent scattering, where the atomic electron binding energy is neglected except for the photoelectric effect [9].

2.4 Pair production

Pair production will occur when X-ray photons with an energy higher than 1.022 MeV interact with atomic nuclei. A schematic diagram about the process of pair production is shown in Fig. 2. The photon of energy *hv* loses its entire energy when it collides with the nucleus of the atom.

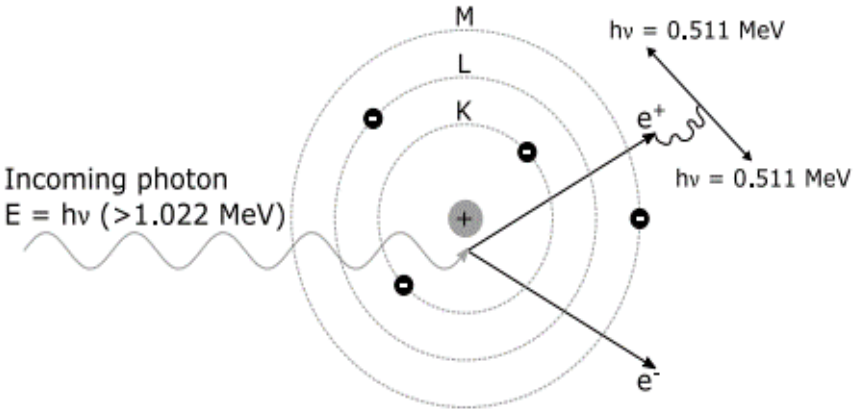

Figure 2. Pair Production Process [8]

The law of conservation of total energy, momentum and electric charge controls these interactions. After the interactions, a pair of electrons and positron occurs. The positron, **+e**, as a particle has the same properties as an electron except for its opposite charge signs. The two particles, electron and positron have opposite charges and their magnetic momentum signs are opposite. An opposite charge sign means that the summation of the net charges of pairs will be zero. This is equal to the initial photon before the collision [6], where, the conservation of electric charge is maintained. When a photon, passes near the nucleus of an atom, it is subjected to strong-field effects from the nucleus and may disappear as a photon and reappear as a positive and negative electron pair. The two electrons produced **e-** and **e+**, are not scattered orbital electrons but are created in the energy and mass conversion of the disappearing photon. The kinetic energy of the electrons produced will be the difference

between the energy of the incoming photon and the energy equivalent of two-electron masses (2 x 0.511 or 1.022 MeV) [11, 12].

$$E_{e+} + E_{e-} = hv - 1.022(Mev) \quad (2.5)$$

The momentum in this process can be neglected because the atomic nucleus is thousands of times massive than a pair of electrons and positrons, where the photon momentum is absorbed.

2.5 Mass attenuation coefficient

X-ray photons are quanta of electromagnetic radiation with zero mass, zero charges and travel at a velocity of the speed of light. X-ray photons are electrically neutral and lose energy through columbic interaction with atomic electrons [11]. During the interaction of an X-ray photon with a material, the X-ray photon deposits its energy in the material by ionisation [12]. The probability of an interaction per unit distance travelled by an X-ray photon in a material is referred to as linear attenuation coefficient (μ).

The linear attenuation coefficient is an important parameter for characterizing the penetration and diffusion of X-rays in a material. The scattering and absorption of X-ray radiation are related to the density and effective atomic number of material. However, the linear (μ) or mass attenuation (μ/ρ) coefficient, which is defined as the probability of all possible interactions between X-rays and atomic nuclei of the material [22, 23]. These attenuation coefficients depend on the incident photon energy and the absorbing materials parameters such as material type, thickness and densities. The accurate values of mass attenuation coefficients (μ/ρ) of X-rays in a material is of great importance for industrial, biological, agricultural and medical studies. Several related parameters can be derived from the mass attenuation coefficient, such as mass energy-absorption coefficient, total interactions, cross-section, the effective atomic number and the electron density.

The theoretical relationship for the determination of linear mass attenuation coefficients can be deduced from the Beer-Lambert law [19, 21] as

$$I = I_0 e^{-\mu x} \tag{2.6}$$

Where I_0 is the incident photon number, x is the penetrated thickness of the material (mm), μ is the linear attenuation coefficient and I is the transmitted intensity through the material [23]. The mass attenuation coefficient ($\frac{\mu}{\rho}$) of the material is also given as

$$\frac{\mu}{\rho} = \frac{1}{\rho x} \ln\left(\frac{I_O}{I}\right) \tag{2.7}$$

Where ρ is the material density (g/cm^3). The mass attenuation coefficient ($\frac{\mu}{\rho}$) (cm^2/g) is relevant in the determination of the chemical compound or the mixture of elements. This is expressed as

$$\frac{\mu}{\rho} = \sum_i w_i \frac{\mu}{\rho_i} \tag{2.8}$$

Where w_i and $\frac{\mu}{\rho_i}$ are the weight fraction and mass attenuation coefficient of the ith constituent elements respectively. The mass attenuation does not depend on phase transformation of the material (such as gas, liquid or solid). This makes it useful to define the mass attenuation coefficients for the chemical composition by the weight fraction as $\boldsymbol{w_i}$.

The calculation of the total mass attenuation coefficient as the sum of the $\tau_{photoelecctric}$, the atomic photo effect cross-section, $\sigma_{Compton}$ as the Compton scatter cross-section and k_{pair} the pair production cross-section for electron-positron production in the field of the nucleus is as expressed in Eqn.2.9.

$$\mu_\rho = \frac{\mu}{\rho} = \frac{1}{\rho} \left(\tau_{photoelectric} + \sigma_{Compton} + k_{pair}\right) \tag{2.9}$$

The total mass attenuation coefficient depends on the effective atomic number and electron density of the material, which are the basic quantities required in determining the penetration

of X-ray in the material. The total mass attenuation coefficient is also a measure of the probability of the interaction that occurs between incident photons and the material at a unit mass per unit area. The knowledge of the mass attenuation coefficients of X-rays in aluminium alloys and other materials is of significant interest for industrial applications. Additionally, the total mass attenuation coefficient provides a wide variety of information about the fundamental properties of the material at the atomic and molecular levels. The total mass attenuation coefficient for aluminium alloy is 0.0241 $cm^2 g^{-1}$ at 8 MeV [22]. The mass attenuation coefficient of pure aluminium alloy is shown in Fig. 3.

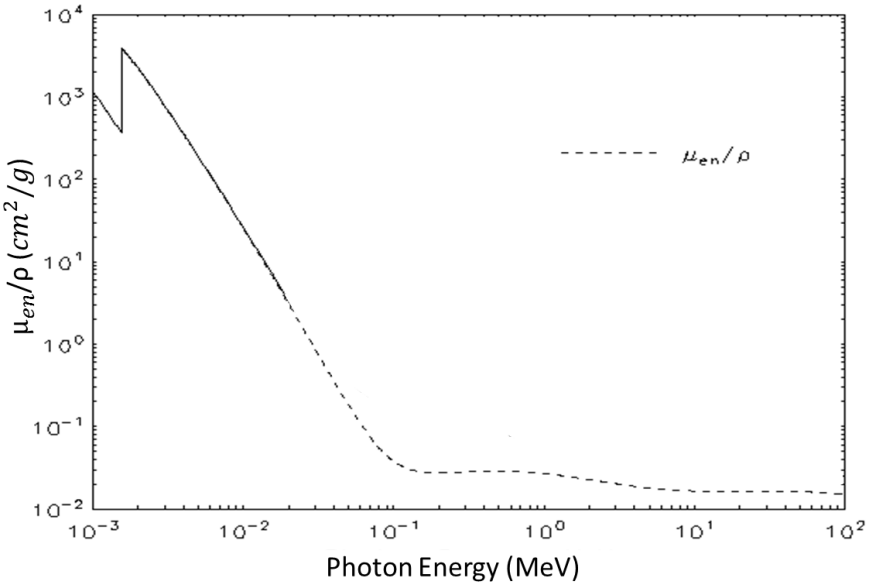

Figure 3. Graph of the mass attenuation coefficient of pure aluminium alloy (μ_{en}= energy integrating detector used) [22]

3 Welding and Weld Imperfections

3.1 Introduction

Welding processes are essential for the manufacture of a wide variety of products, such as metallic frames, pressure vessels, automotive components and any product, which is produced by welding. However, welding operations are generally expensive; it requires a considerable investment of time and has to be established under the appropriate welding conditions. The major challenge in welding, especially in aluminium alloys is the appropriate performance of welded components devoid of welding imperfections such as inclusion, porosity and solidification cracks etc. There are many welding processes, which are employed as a function of the material used, as well as the geometric characteristics of the material used.

This chapter describes the background information of aluminium alloys productions, properties and the impact of aluminium chemical composition on solidification cracking (hot cracking) during welding.

3.1.1 Aluminium

Aluminium is an ancient metal, which has been produced and used industrially since the last centuries [44, 48]. The aluminium alloy has become one of the most important and widely used construction materials in engineering works until today. During the industrial revolution in the 18th century, with the high dependency on machines, aluminium alloy usage has increased in different industrial fields, such as automobile construction, housing, ship and aircraft structures [46, 47]. Aluminium has been investigated for material behaviour for different aluminium alloys and the corresponding fracture behaviour of its components [44, 45].

3.1.2 Aluminium production

The versatility of aluminium makes it the most widely used metal after steel and the most abundant metal in the world, which comprises about 8% of the earth crust [48]. Aluminium has a very stable chemical compound known as alumino-silicates and the extraction of metallic aluminium is a very complex series of industrial processes [49]. The worldwide demand for aluminium is approximately 29 million tons per year. About 22 million tons are new aluminium

and 7 million tons are from recycled aluminium scraps [44, 47]. It takes about 14,000 kWh to produce 1 ton of new aluminium. This explains the high cost of aluminium productions.
The ore most commonly used for the extraction process is bauxite together with silica and titanium dioxide [43, 48, 50]. Bauxite contains an appreciable amount of iron compounds that gives its red colour characteristic.
Bauxite is mined in the form of granules and does not need crushing before being treated [46]. The bauxite granules are digested at high temperature and pressure with caustic soda to dissolve the aluminium, leaving iron, silicon and titanium compounds undissolved [49, 50]. These undissolved residues are washed to leave a liquor that contains only aluminium in the caustic solution [47]. The aluminium is precipitated out as a hydrate with an energy of about 14,000 kWh, washed and calcined to produce the aluminium metal [46, 48].

3.1.3 Aluminium properties and applications

The properties of an aluminium alloy differ by grade, which depends on the alloys chemical composition. This gives each alloy a certain grade and characteristics.
These grades and chemical compositions give each aluminium alloy its properties and characteristics such as strength, lightness, corrosion resistance, recyclability and formability [28, 44, 46].
Some of the common properties of aluminium alloy are:

- Aluminium and most of its alloys range are resistant to various forms of corrosion, due to their chemical affinity with oxygen. The surface of the metal is permanently covered with a layer of aluminium oxide, for corrosion prevention [49, 50].
- It is a good thermal and electrical conductor
- Aluminium is widely used as a raw material for food packaging because of its non-toxic and low permeability properties [41, 46].
- Aluminium has high diffuse reflectivity and low secondary heat emission factor. These properties make it useful for protective shields and ventilators in offices and industrial buildings [48].

The chemical composition of an aluminium alloy is described by the addition of other elements to pure aluminium to enhance its properties and primarily to increase its strength. Most of these

elements are iron, silicon, copper, magnesium, manganese and zinc at levels that make up about 15 percent of the alloy weight.

The properties for the three classes of aluminium alloy used in this research are outlined as follows according to EN 573 [45]:

1xxx Series

The 1xxx series alloys comprise of aluminium 99 percent or higher purity aluminium. This series has excellent corrosion resistance, excellent workability, as well as high thermal and electrical conductivity. The 1xxx series is commonly used for electric transmission or power grids. A common alloy designation in this series is 1050, for electrical applications [26, 28, 38].

5xxx Series

For this alloy, magnesium is the primary alloying agent series, is one of the most effective and widely used alloying elements for aluminium. Magnesium offers a range of positive effects. The magnesium element increases the strength and the alloys strain hardening ability while also increasing weldability. Alloys in this series possess high strength characteristics, as well as good weldability and resistance to corrosion. The aluminium-magnesium alloys are widely used in building and construction, storage tanks, pressure vessels and marine applications. Examples of these alloys series applications are 5059 in electronics, 5083 in marine applications and military fighting vehicles [46, 65].

6xxx Series

The 6xxx series are versatile, heat treatable, highly formable and weldable. The 6xxx series are moderately high strength coupled with excellent corrosion resistance. Alloys in this series contain silicon and magnesium element. The combination of silicon and magnesium elements strengthens the alloy by precipitation hardening heat treatment. They have improved weldability due to increased fluidity and lower shrinkage. Most of the extrusion products from the 6xxx series are the preferred choice for architectural and structural applications. Alloy 6082 is the most widely used alloy in this series and is often used in truck and marine frames [48, 52].

Apart from the numerous advantages and increasing applications of aluminium alloys in all sectors of industrial applications, the aluminium alloy is highly susceptible to weld defects during and after welding. These challenges faced during the weldability of aluminium has become the driving force for the investigation and development of viable and efficient ways for

joining an aluminium alloy. Thereby, having an in-depth understanding of the causes of weld defects without adverse effects on the alloys mechanical, chemical and metallurgical performances [47, 50].

3.2 Aluminium alloy weldability challenges

One of the most severe challenges in aluminium welding is the occurrence of cracks during solidification [47]. The susceptibility to solidification cracking defines the weldability of an aluminium alloy [26, 28]. This depends on the alloys chemical composition, welding conditions and weld geometry. Some aluminium alloys have such a high cracking tendency that welding without cracking is not possible, notably are aluminium alloy series (2xxx and 7xxx alloys). These aluminium alloys are highly susceptible to solidification cracking commonly referred to as hot cracking [27, 32, 51]. This is a major defect occurring above the solidus temperature, either upon solidification cracking or upon liquation cracking [28, 30, 33].

Hot cracking criteria are based on the influence of grain morphology and thermal fields induced by welding. These mechanisms are not easily predictable due to the complex influential factors that play a major role in aluminium alloy weldability to produce a defect-free weld [56, 57].

3.2.1 Hot cracking phenomenon

The mitigation of the occurrence of hot cracking in aluminium alloy weldability is difficult for one to achieve. This is a result of the welding process, metallurgy and mechanical influences during welding. Several tests have been proposed and developed to characterize the aluminium alloy propensity to hot cracking [6, 30, 62]. During welding, the aluminium alloy is subjected to high thermal gradients around the melting zone due to localized heat input. The melting zone undergoes cooling of the molten weld pool while welding is in progress. The melting zone is bordered by two isothermal surfaces, they correspond to liquidus and solidus temperatures in between the mushy zone [29, 35, 36]. The mushy zone corresponds to the coexistence of liquid and solid phases [5, 28, 70]. Upon solidification, the solidifying weld metal shrinks due to solidification shrinkage and thermal contraction [33, 73]. When solidification progresses, the mushy zone begins to form a rigid continuous network that is being induced by the surrounding material. A separation of the microstructure at the grain boundaries occurs when the deformation exceeds a certain threshold [39]. Additionally, at the terminal stage of

solidification, an opening cannot be compensated by the remaining liquid due to low permeability and high solid fractions [37, 38]. Furthermore, solidification temperature range, segregation of impurity elements, the morphology of solidifying grains, liquid feeding and grains coherency are some of the important metallurgical factors affecting solidification cracking [34]. At the coherency temperature, the solidification in the mushy region begins to form a rigid continuous network. Hot cracking occurs when the coherency in the mushy region and the coherency temperature drops [43, 45]. This notion has been extended to weld solidification cracking and it states that hot cracking occurs due to the rupture of liquid films that persist until the last stage of solidification. In reference to the works of Prokhorov, that considers the mushy zone as a single entity and defines the ductility of a material by its solidification rates [43, 58, 63, 73]. The Prokhorov model is influenced by the critical strain rate criterion that leads to hot cracking. The Prokhorov model of hot cracking occurrence is extensively discussed in Subchapter 3.2.3.1.

3.2.2 Hot cracking models

The concept of hot cracking has numerous fundamental theories as well as characteristics that cause the initialisation of hot crack formation [31, 34].

The three primary factors that influence the susceptibility of an aluminium alloy to cracks are categorized as welding process, Metallurgy and Design as seen in Fig. 4. These factors define the occurrence of hot cracking during welding.

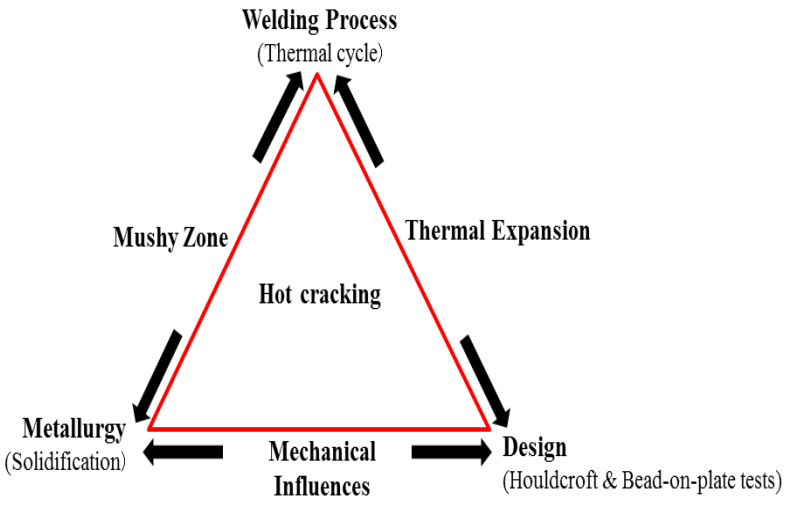

Figure 4: Influential factors for hot cracking [1]

From the chart above, the welding process is mainly characterized by the thermal cycle generated from the welding parameters such as welding speed, current and voltage that constitute the heat input of the weld [35, 36]. The heat input influences the susceptibility of an aluminium alloy to hot cracking by generating a brittle temperature range (BTR) during welding [27, 28]. This BTR corresponds to the interval between the coherency temperature (where the liquid does not easily circulate because of the low permeability of the solid structure) and the coalescence temperature (where the solid opposes mechanical resistance) in the mushy zone [4, 73, 77]. During welding processes, the thermal loading is primarily produced by thermal contraction due to temperature evolution around and within the mushy zone. The cooling rate after welding affects the solidification shrinkage (due to phase change) as well as the thermal contraction of the weld by the expansion coefficient of the solidified weld [39]. This leads to the formation of hot cracks within the mushy zone because of the solidification rate [45, 51, 56].
The welded design, on the other hand, is the mechanical impact caused by the geometry and stiffness of the weld surroundings. However, the kind of weld design technique used will have an impacting role in facilitating cracking susceptibility. Typical examples of welding designs used for the investigation of hot cracking formation are the Houldcroft test (HCT) and bead-on-plate (BOP) test [41, 43, 58]. In the Houldcroft technique, the material stiffness is varied by the length of the saw cut slots to the base material, as shown in Fig. 5. However, the bead-on-plate (BOP) test has no saw cut slots at its edges, this is shown in Fig. 17. The bead-on-plate (BOP) test is commonly used to investigate constant arc welds during welding [33, 57].

3.2.3 Hot cracking influencing factors

During solidification of the weld pool, hot cracking occurs when the grains structures impinge on each other [41]. The strains rate causing solidification shrinkage and thermal contraction of the solidifying material leads to a rupture of the liquid film at the grain boundaries. One explanation for this rupture is the excess of a critical strain limit within the *Brittle Temperature Range* (BTR) [45, 69]. For many alloys, it is known that the solidification range corresponds to the alloys susceptibility to solidification cracking [51]. This is well explained by the *Rappaz-Drezet-Gremaud criterion* (RDG), as the pressure drop of the liquid phase between the roots of two neighbouring grains suffering insufficient liquid feeding [4, 55, 57]. Additionally, the chemical composition of the interdendritic liquid phase also influences the solidification cracking behaviour of the aluminium weld [46, 47]. The strength of the weld is influenced by the alloy chemical composition and temperature distribution and has an adverse influence on the hot crack initialisation [65, 76, 79].

3.2.3.1 Critical strain

The critical strain of an aluminium alloy occurs at the semi-solid region of the weld seam (i.e. mushy zone). This is the region where the aluminium alloy exceeds its strain limits and causes a rupture in the alloy [42]. The strain is caused as a result of solidification shrinkage and thermal contraction that exert a force within the alloys grains structure and leads to segregation of the grain boundaries. This is known as the brittle temperature range (BTR), in which the susceptibility to hot cracking is likely to occur [34, 43]. As predicted by the Rappaz Drezet and Gremaud model (RDG), the hot cracking of an aluminium alloy is influenced by the critical strains along the alloys solidification path during welding (refer Subchapter 3.3.4) [44, 73].

3.2.3.2 Brittle temperature range (BTR)

The brittle temperature range (BTR) of the weld relates to the temperature range over which solidification cracking occurs. As the initial amount of liquid present in the interstices phase of the solid network is reduced to a thin continuous liquid film, it is finally isolated into liquid pockets [70]. The initiation of a solidification crack appears because of the high permeability of the mushy zone (i.e. high liquid feeding), and at the inter grain solid bridging [27, 41]. Solidification cracking is likely to initiate, where the alloy possesses both low permeability, low strength and low ductility within the BTR [56, 70].

The assertion of hot cracking susceptibility with regard to high-temperature brittleness is well formulated by Prokhorov, where the formation of hot cracks depends on three factors [33, 51], i.e. size of the temperature brittleness range, plastic strain capacity, as well as the rate at which the strain increases. As shown in Fig. 5, the brittle temperature range reflects the changes in metal plasticity as a function of the high-temperature brittleness. At the liquidus temperature, the mixture of liquid and solid crystals in the microstructure yields high formability [25, 26, 30]. As the crystallization temperature decreases, the plasticity also rapidly decreases to reach a critical value of plasticity. When the straight lines “at the mushy zone”, which represents the amount of strain, crosses the brittle temperature range it will cause cracks to be formed [37, 50].

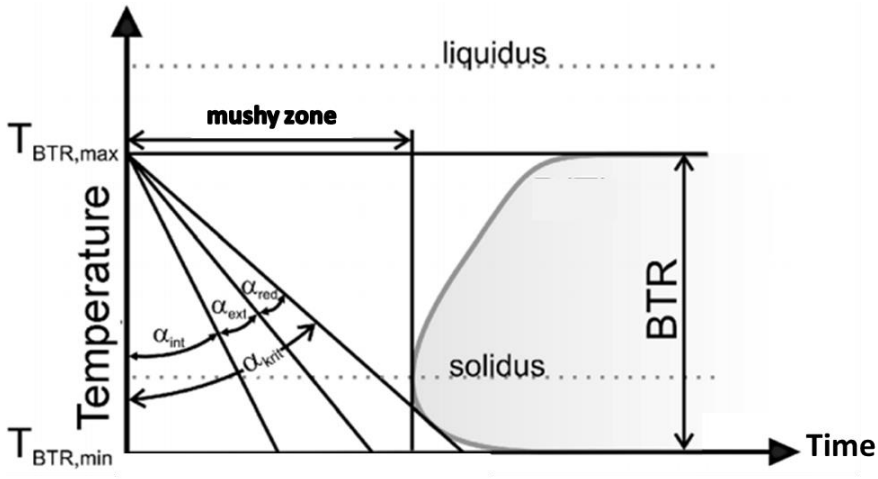

Figure 5: Scheme of the dependence between alloy plasticity within the mushy zone and the intensity of increasing strain, critical temperature intensity of strain determined from the tangent of the slope angle of a straight line [45].

Hot cracks appearing in the brittle temperature range are defined as the temperature interval where the microstructure is in a critical configuration [16, 26].

The resistance to hot cracking is also characterized by the plasticity margin ratio of the weld pool [33]. This is a quantity associated with the critical temperature intensity of strain (*CST)* and the high-temperature brittleness range. This depends mainly on metallurgical factors and the thermal conditions during welding [34, 38]. This temperature brittleness range ($T_{BTR,max} - T_{BTR}, min$) can be calculated as shown in Fig. 5 above [45].

The essential variables of the heat input are heat transfer coefficient, density, heat capacity, thermal conductivity coefficient, welding speed, welding torch power and base material thickness [54, 56, 57].

The temperature fields and the microstructural state fields also depend on the welding volumetric strains and welding deformations rates. The volumetric strain occurs as a result of thermal expansion, chemical composition and microstructural transformation [45]. This region of distortional strain happens as a result of time-independent plasticity and time-dependent viscoplastic deformation [39]. At this point, the strains owing to solidification shrinkage and thermal contraction can be carried by the solidifying material. This leads to a rupture of the remaining liquid film at the grain boundaries [47, 80, 81].

3.3 Welding Tests

3.3.1 Hot cracking tests

Most of the hot cracking susceptibility is usually determined by the external load exerted on the base material or by the kind of welding design technique used [41]. The purpose of an external load for the hot cracking test is to investigate an aluminium alloys susceptibility to cracking in relation to the applied mechanical loading [27]. The input variables such as external loading and welding parameters can be assigned to measurable output data, such as crack length and position of cracks. This makes the results interpretable and comparable to other welding techniques i.e. self-restraint hot cracking tests (Houldcroft test (HCT)) [39, 42]. The most used external load fabrication for hot crack tests are the Modified Varestraint Transvarestraint (MVT) and Transvarestraint tests [43]. The Modified Varestraint test and Transvarestraint test differs only by the bending direction of the welded material [35, 45].

3.3.2 Self-restraint test (Houldcroft test)

In the self-restraint test, solidification cracks are generated as a result of the material design, mechanical and chemical properties of the aluminium alloy [26]. The self-restraint cracking tests are employed to reproduce the actual welding conditions as closely as possible [51, 52]. The configuration of the base material and the related fixtures are designed to induce different restraints [53, 54] as shown in Fig. 6. In the application of the Houldcroft crack susceptibility test, the base material is machined with several saw cut slots of various lengths that are perpendicular to the weld seam. These saw cut slots reduce the stiffness of the base material [40, 41]. The shortest slots length has maximum stiffness and hot cracking is highly susceptible. As the length of the slot increases, the stiffness of the material decreases and the crack created at the beginning will curtail as the welding proceeds. The generated crack length is measured and compared to the solidification crack susceptibility of other welded alloys [39].

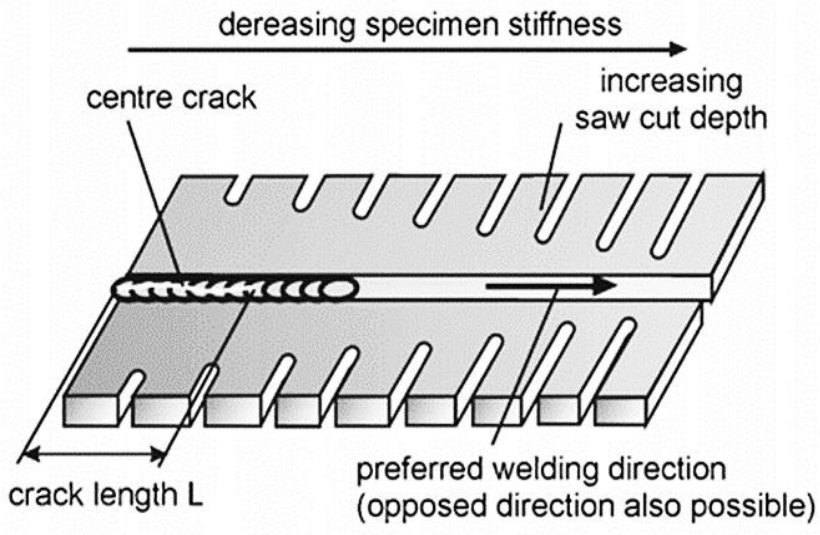

Figure 6: Houldcroft cracking test with saw cut slots [41]

The base material dimensions and the distance between the width and depth of the slot depending on the material thickness [7, 56]. The Houldcroft base material dimensions used in this work are illustrated in Fig. 19.

3.3.3 Solidification behaviour of welded alloys

The solidification behaviour of the weld pool depends on the three main parameters that influence the solidification cracking of the weld pool, which are the welding speed (s), arc current (I) and the arc voltage (U), which are commonly summarised as the heat input per unit length(HI) [kJ/mm]. These form the fundamental solidification mechanics of the weld pool in the metallic alloy [49] and is defined as

$$Heat\ Input(HI) = \frac{Voltage * Amperage\ [W]}{Welding\ Speed\ [\frac{m}{s}]}\ \text{[kJ/mm]} \tag{3.1}$$

This is an essential parameter for comparing different welding procedures for a given welding process. The other parameters that have an adverse influence on weld solidification cracks are the heat transfer efficiency [52, 53], cooling rate, thermal gradient and cracks growth rate [49, 51].

The heat input controls the temperature in the welding pool:

$$Thermal\ gradient\ (G) * Solidification\ growth\ rate\ (R) = \frac{dT}{dt} \quad (3.2)$$

Where $\frac{dT}{dt}$ is the temperature distribution in the mushy zone to time. The base metal crystals transform from liquid to solid in this region. The base metal grains at the fusion region acts as the substrate for nucleation and the substrate grain at the liquified zone is where complete crystallization of base metal initiates [45].

3.3.4 Weld pool mechanics

The weld pool mechanics of the weld is commonly referred to as the fluid dynamic portion of the weld, where the base metal has reached its melting point during welding [37]. The weld pool is dependent on the thermal conditions and the characteristics of the fluid flow [82, 83]. The weld pool solidification is the dynamics of weld pool development to its welding speed. Furthermore, the thermal interaction of the weld pool plays a major role in the fluid flow, which relates to the weld pool size and shape [74, 75]. The two main types of weld pool shapes are the tear drop and an elliptical shape. The elliptical pool shape is usually associated with high heat input and low travel speeds and the tear drop shape is also associated with lower heat input at a fast travelling speed of the welding torch [56].

As shown in Fig. 7, the weld pool is categorized into two parts, which are the liquid circulation region and the mushy zone. For this region, the brittle temperature range (BTR) is determined by the Rappaz Drezet Gremaud criterion (RDG) [68, 69, 70].

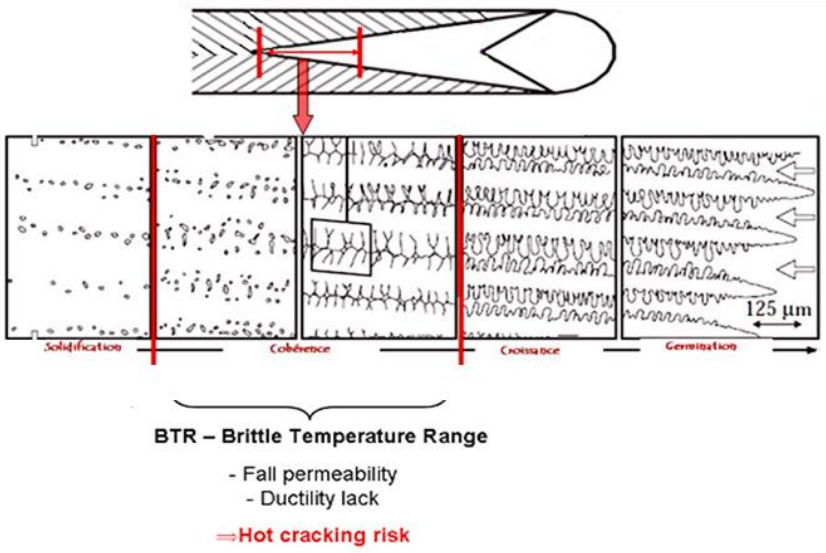

Figure 7: Schematic of hot crack formation by RDG approach [63]

The Rappaz Drezet Gremaud (RDG) criterion for hot cracking is based on the mass balance performance at the liquidus and solidus interface [70, 75]. This accounts for the deformation of the solid microstructure that is directly perpendicular to the dendrites due to the interdendritic liquid flow induction [76]. Hot crack susceptibility of the aluminium alloy is primarily influenced by the micro-porosity, which is also associated with the solidification rate and shrinkage of the grains. The solidification rate and grain shrinkage are caused by stress and pressure in the brittle temperature range [79]. The RDG is mathematically expressed from Darcy´s equation to explain the liquid flow in the mushy zone, see Eqn. 3.3 [65, 70]. The brittle temperature range is used to evaluate the solidification cracking susceptibility of the welded alloy by determining the strain rate, temperature distribution and crack length as shown in Fig. 7 [63, 77].

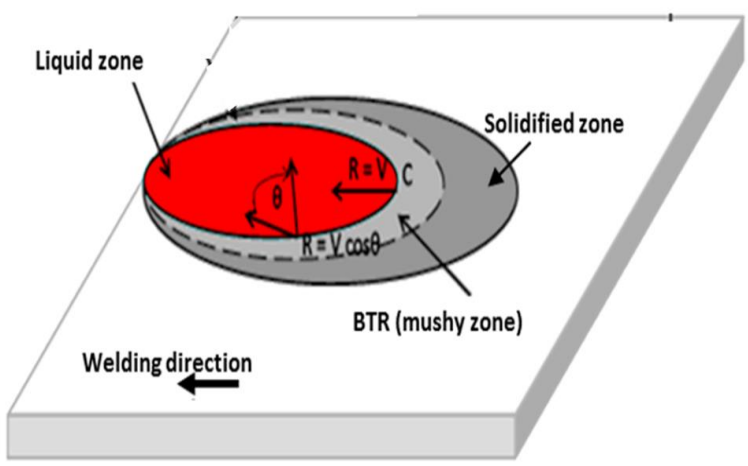

Figure 8: Influence of the welding speed V on the crystallization rate R at selected points of the weld pool isotherms [55]

One other major influence on the weld pool is the fluid dynamics or molten conditions in the weld pool that depends on the welding speed.

The mathematical representation of the weld pool isotherms, where the crystallization rate R is deduced from Fig. 8 [75, 77, 79] as:

$$R = V cos\Theta \tag{3.3}$$

Where Θ is the angle between the welding speed (V) and the crystallisation direction.

The proportionality between the crystallization rate of the molten metal in the weld pool **R** and the cooling rate (W) is expressed in Eqn.3.4.

$$R = kW \tag{3.4}$$

Where k is the proportionality factor for defining the cooling rate W at any point of the phase interface in the weld pool. The crystallization rate **R** of the molten metal is determined by the liquid permeability and lack of ductility in the mushy zone during the solidification of the weld seam.

This causes a change in the viscosity of the aluminium alloy during the liquid-to-solid transition [63]. This transition is due to the deformation of the dendritic network, which strongly depends on the coherency state and the flow of liquid of the alloy undergoing a porous solid phase. The formation of hot cracks are also associated with a lack of feeding in the mushy zone, but only for a specific region of the dendritic network, which is subjected to strains [45]. The porosity in

welds is associated with the hydrostatic depression in the mushy zone combined with the segregation of gaseous solute elements [41, 44]. This depression is also associated with the section of the liquid in the porous dendritic region due to shrinkage [82, 83]. Examples of notable welding defects are shown in Fig. 9, which are commonly encountered during the welding of aluminium alloys.

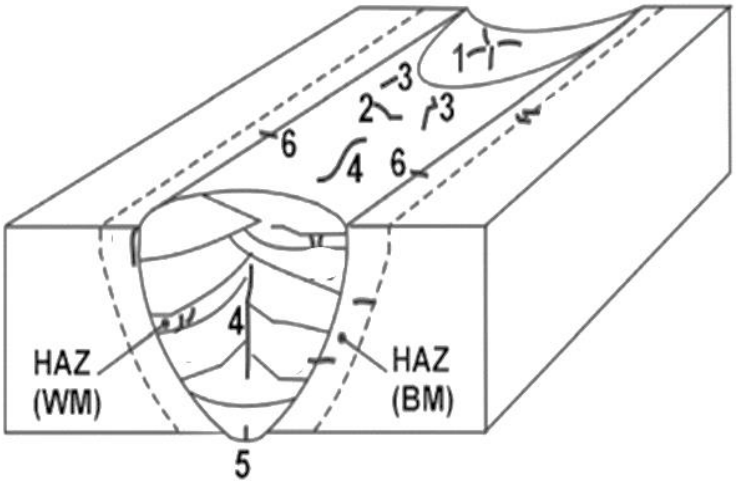

1 - Crater crack	4 - Centreline crack in longitudinal section and transverse section
2 - Transverse crack	5 - Root crack
3 - Longitudinal crack	6 - Edge crack
HAZ – Heat Affected Zone	BM / WM - Base Material / Weld Material

Figure 9: Types of weld cracks [34]

Other physical defects that occur in welds are undercut, insufficient fusion, excessive deformation and porosity, which also affect weld quality and its durability.

All modern welding standards show zero tolerance for cracks whereas the other defects are tolerated within certain limits [59]. The most common defect encountered in any of the aluminium alloy series is crater cracks. These small cracks appear at the end of the weld seam where the arc has been broken. They are also called shallow hot cracks. Although small, these

cracks also propagate into the weld bead [60]. The major reason for these defects is an incorrect technique for ending the weld.

Aluminium cools so fast; it does not provide adequate time for the weld bead to flatten or the crater to fill. To properly end a weld, the crater should be filled. This is done by reversing the arc travel direction before breaking the arc [61]. In addition, if the welding control is designed to supply gas for a short time after the arc is broken, the crater should be shielded until it is completely solidified.

The transverse cracks are perpendicular to the weld direction. This occurs because of high shrinkage stress acting on the welded material of low ductility especially on the final pass or by the hot cracking mechanism. This type of crack can also be an extension of a crack that is initiated at the end of a weld [82, 83]. Centreline cracks and root cracks, on the other hand, are cracks caused by undue stresses on the centre of the weld. The root or edge cracks are cracks formed by short beads at the root of the weld. The reason for the generation of root or edge cracks is the alloys hydrogen brittleness [76].

All these cracks are unacceptable discontinuities and are considered detrimental to the performance of the weld.

3.4 Summary

The above summarized the factors of hot cracking initialisation during aluminium fusion welding. The notable influencing factors for solidification cracking are the chemical composition, weld design and the welding parameters such as welding speed, current and voltage. These factors have direct and indirect influences on solidification cracking during welding. Most of these challenges are known and extensive work [32, 78] has been carried out to quantitatively understand some of the problems such as:

- Solidification crack initialisation and growth in the mushy zone
- Crack length, crack positioning and the rate of growth in relation to the welding parameters
- In-situ observation of crack initialisation and propagation during welding
- Determination of crack depth in the volume

The experimental investigations in chapter 6 were performed on aluminium alloy series 1xxx, 5xxx and 6xxx. These alloy series are known for their excellent mechanical properties but are highly susceptible to cracks.
The welding parameters were chosen to ensure the complete melting (i.e. heat input) of the welded alloy to facilitate the initialisation of hot cracks during welding.
Welding designs of both Houldcroft and bead-on-plate (BOP) tests were also used to test for strains. In the application of the Houldcroft crack susceptibility test, the base material is machined with several saw cut slots of various lengths that are perpendicular to the weld seam as shown in Fig. 5. These saw cut slots reduce the stiffness of the base material. At the shortest slots length, the stiffness is maximum and hot cracking is highly susceptible. The length of the slot increases the stiffness of the material and decreases the crack growth rate. This is different to the bead-on-plate (BOP) test without saw cut slots at its edges.
The damage models (e.g. Rappaz Drezet Gremaud (RDG) criterion) describe the evolution of crack initialization; growth and coalescence were adopted to investigate the crack propagation.

4 Real-Time In-situ Radiography

4.1 Radiographic sources (X-rays, Synchrotron, Neutron)

X-rays are a form of electromagnetic radiation as light. X-ray distinguishing feature is its extremely short wavelength of about 1/10,000 to that of light [11]. This characteristic is responsible for the ability of X-rays to penetrate materials. The total amount of radiation emitted by an X-ray tube depends on tube current, voltage and exposure time [8, 9]. When other operating conditions are held constant, a change in tube current causes a proportional change in the intensity of the radiation emitted [21, 23]. Conventional X-rays are mostly used for NDT inspections; however, some of the other radiation sources that can be used for NDT inspections are synchrotron radiation and neutrons. The synchrotron radiation is used to study the corrosion and hydriding mechanism in metallic alloys [84, 85]. Synchrotron radiation diffraction and fluorescence are usually applied to study oxide layer structures [86].

Moreover, synchrotron radiation imaging is also known for its high spatial resolution and its sensitivity to determine low background crystal structures. The observation of fatigue crack propagation behaviour under torsional loading using microcomputer tomographic imaging of synchrotron radiation was carried out by Shiozawa et.al [90]. Shiozawa´s detection of torsion fatigue crack propagation behaviour was observed using synchrotron imaging for continuous monitoring of the shape of the crack inside the material. Kromm et.al [31] studied the use of synchrotron radiation for in-situ phase analysis for low transformation temperatures in welding material. This is the compressive residual stresses within a welded material and its adjacent areas are obtained by measuring the kinetic transformation of crystalline phases during welding [41, 42].

Helfen et. al [86] introduced the use of both synchrotron radiation and computer tomography for 3D inspections of cracks in composite polymers and alloys.

The other radiation that is also been used in material characterization is neutron radiation (thermal neutrons). This is known for its penetrating features and its zero-charge particles, which do not interact with electrons present in a material [81, 83]. Neutrons interact primarily with the nuclei of an atom within a material. Both scattering and absorption processes occur by removing neutrons from the beam directed to an object. The detection of moisture-initiated corrosions in products is the major industrial application for neutrons. Some research work was carried out with neutrons by Mayer et.al [87, 88]. Neutron irradiation of dilute aluminium alloys was investigated to look into the distribution of aluminium alloy atoms and to determine the interstitial dislocation loops nucleate that grows and interacts to form a dislocation network

[109]. This is termed to be an alternative for microstructure variation determination of alloys by nuclear transmutation reactions, that enable clustering of vacancies into voids in alloys [79. 83].

All these different radiation sources have various advantages in the study of material structure characterization and defect determination. However, the disadvantage of using synchrotron radiation is that it requires a highly protective shielding of dangerous radiation from the accelerator and this requires a huge space to set up for a remote-controlled experimental laboratory. This makes it costly to operate the synchrotron and limits the rate of experiments that can be conducted.

Neutron radiation devices, on the other hand, are usually used as supplementary to X-ray radiography. In comparison, neutron radiation is also expensive to generate and maintain [91, 92]. It also possesses low beam intensity relative to X-ray and therefore cannot be used in investigations of time-dependent processes.

Conventional X-ray radiation possesses several advantages over the other radiation sources i.e. synchrotron and neutrons. It is extensively applied in many fields, i.e. in medicine, aeronautics and petrochemical industries etc. and can be obtained in different energies and focal spot sizes [85, 86].

4.2 Digital radiography

Digital radiography is one of the most used non-destructive testing (NDT) techniques in several industrial applications. Digital Detector Arrays (DDA) or Flat Panel Detectors (FPD) offer straight digitization of the radiographic image. This technology presents high-quality images with many possibilities of post-processing [13, 17]. DDA may operate directly or indirectly by converting incident radiation into an electrical charge that can be read out. Direct detectors convert the absorbed X-rays into charges directly in a photoconductor. Indirect detectors first convert X-rays to visible light in a scintillator and detect the visible light in a photosensor array. Each method has advantages and disadvantages, as well as special limits of use in imaging systems. Indirect detectors use a photosensor built into each pixel and the entire array is covered by a scintillating layer, where X-ray interacts and produces visible light. These light photons are detected by a matrix of photodiodes on a CMOS substrate and the electric charges generated within every photodiode are read by a matrix of transistor switches [94, 95].

The development of a digital detector array has revolutionized radiological applications in several fields of imaging inspections. This has surpassed other imaging detectors such as

radiographic films in various radiological applications [15, 17, 96]. The advantages of the digital detector array are the easy implementation and instant real-time generation of radiographic data. The generated radiographic image can be stored and distributed electronically without the risk of radiographic data loss [93, 100].

The digital detector transforms absorbed X-ray photons into electrical charges per pixel, which are then digitized and quantified into a greyscale value. This represents the number of X-ray photons deposited on the pixel in the digital detector array [91, 92].

4.2.1 CMOS digital detector array

There are several types of digital detector arrays in existence, but for this research, the concentration will be on Complementary Metal- Oxide Semiconductor (CMOS) detectors such as Dexela 1512 using indirect X-ray detection by a scintillator and photodiode [94, 95]. As shown in Fig. 10 and Table 1, are the detector dimensions and features used in this research. Additionally, the digital detector array is protected against the heat from the welding torch to prevent the DDA from damage and overheating during welding. The protection of the digital detector array was done by covering the sensitive area of the DDA with 2 cm thick homogenous fibreglass material in a robust protective case as can be seen in Fig. 15.

Figure 10: Dexela 1512 digital detector array [132]

Table 1: Dexela 1512 Detector parameters

Pixel Size (µm)	74.8
Sensitive Area (mm^2)	145.4 × 114.9
Pixel Matrix (px)	1944 × 1536

This digital detector uses the same technology of integrated circuits used in microprocessors, microcontrollers, RAM and digital logic circuits. The CMOS technology is used in ultra-large-scale integrated circuit chips, which are mostly associated with chips containing millions of complementary metal-oxide-semiconductor field-effect transistors [91, 92, 96]. This is often referred to as Active Pixel Sensing [72, 89]. CMOS light detectors are excellent for its lower power requirements and the fast readout accessibility as well as low noise with peripheral circuitry [93, 95]. CMOS photodiode is usually coupled by fibre optic faceplates on a CsI scintillating screen. The Dexela 1512 detector allows a read-out speed of 8 frames/s and the measured Basic Spatial Resolution SR_b of the detector was 0.08 mm (duplex wire D11 not resolved when placed directly on the detector) which corresponds to image testing class A according ISO 17636-2 above 1.5 mm wall thickness. The measurement of the image quality class of the radiograph are carried out by placing both, a duplex and single wire IQI on the inspected material as shown in Fig. 10. The number of duplex wire pairs visible and single wires are used to determine the image quality numbers of the acquired radiograph.

4.2.2 DDA adjustment and bad pixel correction principles

Digital detector array adjustment and bad pixel correction are common practices in industrial radiology to achieve the highest flaw sensitivity for internal wall thickness changes [99, 101]. The radiographic images quality depends on the basic spatial resolution (i.e. effective pixel size) or geometrical unsharpness, contrast sensitivity, material thickness, image lag, signal-to-noise ratio, bad pixel distribution, dynamic range and internal scatter radiation (see ASTM E2597). These image properties determine the quantitative characteristics of the digital detector array, which are significant to the image quality [96, 98].

The purpose of detector adjustment is as follows

(i) compensating for the differences among the individual pixels that relate to the sensitivity and dark signal response for the generation of a homogenous pixel response.

(ii) compensating for the differences in gain and offset response among individual signal channels of the amplification and digitization electronics of the detector (ADC channels)

(iii) compensating for non-uniformity of the X-ray field

(iv) establishing a known arithmetic relationship (for example, linear or logarithmic) between detector response (grey value) and incident radiation dosage at the detector surface (mGy).

(v) additional processing, for example, identifying and interpolating defective pixels, is also part of the detector adjustment task.

The procedure to determine defective pixels in a radiographic image is by calibrating the DDA with an offset image and gain images to generate calibrated images as described in ASTM E2597 [93, 96].

The standard adjustment practice is to use an offset and a gain image. The offset image is an image with about 30 seconds of integration time captured without radiation. The gain image is acquired when the DDA is been exposed at a constant dose rate at selected energy of about 80% of saturation grey value (GV) of the detector for about 30 s. This is used to equalize the pixel response of the detector pixels [91]. This pixel correction is determined by subtracting the offset image and by scaling the gain image pixel by pixel [14, 113]. The bad pixels, which are the dead pixels or over responding pixel of the detector, needs to be interpolated by neighbouring good pixels.

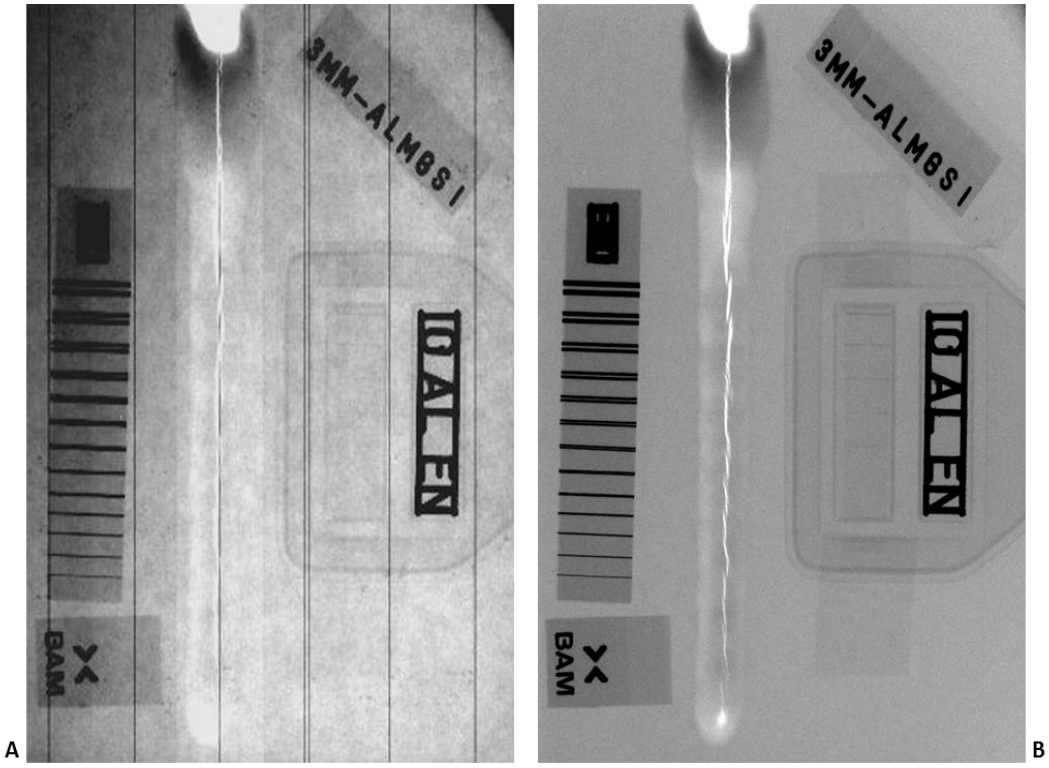

Figure 11: (A) Raw radiographic image and (B) Gain-adjusted radiographic image of AlMgSi alloy, 3 mm wall thickness, 84 kV

As shown in Fig. 11 above, are the images of both raw and gain-adjusted radiographs of AlMgSi alloy with image quality indicators of both single and duplex wire IQI´s. These image quality indicators (IQI`s) are standardised devices consisting of a series of elements of graded dimensions, which enables a measure of the image quality to be obtained. These IQI´s are usually included in every radiograph to assist in determining the contrast sensitivity and spatial resolution of the radiographic image and to provide a reference point for consistency in flaw detection. The single wire IQI is used to determine the contrast sensitivity of the image, whereas the duplex wire IQI, on the other hand, is used to measure the basic spatial resolution of the radiographic image. The duplex wire IQI is made up of 13 wires pairs of platinum with various diameters and distances embedded in a rigid plastic block. The number of wires pairs that are resolvable indicates the unsharpness. The resolved wire pairs are determined by the profile function for the determination of the basic spatial resolution. However, the singled wire IQI consists of a series of straight wires of the same material with different diameters. Before adjustment, the raw image as seen in Fig. 11 (A) has vertical lines, which are caused by manufacturing deviations in photodiode sensitivity. The pixel corrections of the detector software as seen in Fig. 11 (B) correct for such differences. The adjusted radiographic image

can then be used to measure the image sharpness, image contrast and image noise usually referred to as the image quality determination [92, 98]. The resolved wire pairs are determined by the profile function for the determination of the basic spatial resolution according to the ISO 19232-5, see Fig. 12. Tables 2 and 3 below shows the diameters and the corresponding resolution for both single wire and duplex wire indicators, whereas Table 4 indicates the image quality classes.

The achieved image quality class for this research was class A and not class B because to obtain class B, a duplex wire D13 needs to be achieved for the wall thickness above 1.5 mm.

Table 2: Single wire IQI Diameter and numbers according to ISO 19232-1

Element number W = wire	W1	W2	W3	W4	W5	W6	W7	W8	W9	W10	W11	W12	W13	W14	W15	W16
Diameter (mm)	3.2	2.5	2	1.6	1.25	1	0.8	0.63	0.5	0.4	0.32	0.25	0.2	0.16	0.125	0.1

Table 3: Duplex wire IQI diameter and numbers according to ISO 19232-5

Element number D = duplex	D1	D2	D3	D4	D5	D6	D7	D8	D9	D10	D11	D12	D13
$SR_b = \frac{u}{2}$ Diameter (mm)	0.8	0.63	0.50	0.4	0.32	0.25	0.20	0.16	0.13	0.10	0.08	0.063	0.05

Table 4: Maximum image unsharpness for Class A and Class B from Single wire and Duplex wire IQIs (from ISO 17636-2)

Wall thickness	Wire IQI		Duplex IQI	
	A	B	A	B
3 mm	W16	W17	D10	D13

One of the most important aspects of radiographic image quality is X-ray quantum noise. This is a fundamental noise source, which is determined by the radiation dose that is delivered to the detector as well as the X-ray beam energy and absorption properties of the material. In a correctly designed imaging task, the only noise source is the quantum noise of the X-ray source. The noise properties of X-ray imaging systems show also limitations by the noise

introduced by the gain images during detector adjustment as seen in Fig. 12. The Poisson noise of the X-ray radiation is proportional to the square root of the radiation dose. For higher exposure times, the SNR saturation increases, this is caused by the noise injection during detector adjustment using a gain image of 32 frames at 88 ms.

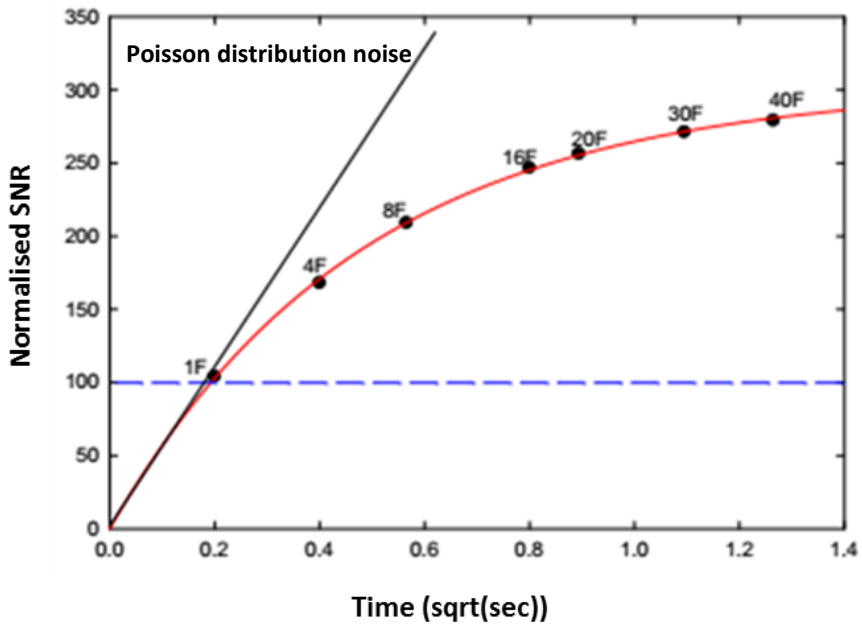

Figure 12: Radiographic image quality analysis of the weld

As seen in Fig. 12, the major parameter of image quality is the normalized SNR (see ISO 17636-2); this requires the measured SNR to be corrected by the basic spatial resolution as expressed in Eqn 4.1 as

$$SNR_N = SNR_{measured} \cdot \frac{88.6\mu m}{SR_b} \tag{4.1}$$

Where SR_b is the basic spatial resolution (in μm) of the detector, which corresponds to its effective pixel size.

4.3 Summary

The image quality of a radiographic image is determined by the degree of detail its shows. The image quality of a radiograph is influenced by a large variety of factors:

- the radiation source (radiation energy and focal spot size),
- the inspected object (especially object material and thickness),
- the imaging set-up and inspection geometry (source to object distance, object to detector distance),
- the detector (basic spatial resolution, Sensitivity and SNR).

Image quality is measured using Image Quality Indicators (IQI´s) as shown in Fig. 11. IQI´s are standardised devices (see ISO 19232) consisting of a series of elements of graded dimensions, which enables the measurement of different image quality numbers. These IQIs are usually included in every radiograph to check the minimum image quality of the radiographic technique.

The determined basic spatial resolution of the detector for a single frame at an exposure time of 40 milliseconds is 100 μm (duplex wire D10 not resolved). The measured SNR in a single frame for all radiographs is 120; this corresponds to a normalised SNR_N of 100. The SNR of an image is usually calculated as the ratio of the mean pixel value to the standard deviation of the pixel values over a given neighbourhood. The measured SNR is determined from a region of interest of 20 x 55 pixels as the ratio of the mean grey value divided by the standard deviation inside this window. The SNR measures how much signal has been corrupted by noise and helps in describing the quality of an image. The measured SNR refers to the relative magnitude of the signal compared to the uncertainty in that signal on a per-pixel basis. High SNR is particularly important in applications requiring precise image quality measurements. The detected photons in the CMOS detector Dexela 1512 follows a Poisson distribution, which is responsible for the photon noise and determines the SNR of the acquired image.

5 Laminographic Principles

The application of laminographic techniques was first used in medical diagnostics applications [102, 104]. Laminography is a method used to obtain depth information on objects when computed tomography is not possible. For instance, the measurement of large planar objects such as the wings of an aeroplane [105, 131]. Apart from the high photon flux, and high spatial resolution of CT, images are usually achieved for equivalent exposure times by employing X-ray magnification techniques [95, 124]. However, consequently, the effective field of view of the detector system at the object position becomes reduced simultaneously. The resolution of the CT scan is limited by the requirement that the tomographic field-of-view has to cover the full object in the lateral direction to avoid truncation artefacts. To achieve CT non-truncated projections, the entire illuminated object volume should stay within the detector's field of view during a full tomographic rotation. In that effect, the tomography can be relaxed to a certain extent depending on the size of the object, but for laterally extended objects, this requirement often implies that the regions of interest (ROI) must be extracted. This is usually done by cutting or machining a small object out from the tested object. This object extraction, however, is a drawback for non-destructive inspection. Even if object extraction succeeds without deterioration of significant parts of the object volume, some objects may not provide sufficient mechanical stability for performing the CT scan [105, 122, 126]. In these cases, computed laminography provides a viable alternative to CT. There are several kinds of laminographic scanning geometries namely co-planar laminography, swing laminography and rotational laminography [102, 103].

The swing laminography is a limited angle tomography and has a scanning geometry where the object is not swung to full 360 degrees, but rather to a smaller angular range e.g. +/- 30 degrees. In swing laminography, the scanning geometry is very similar to that of rotational laminography [84].

Rotational laminography is realized by the rotation of the planar object around an axis perpendicular to its surface. The X-ray source and detector remain fixed in position during scanning [84, 86]. While in translational coplanar laminography, both object and detector are moved in parallel to the X-ray source [94]. In opposite, a linear motion of the X-ray source relative to the fixed object and detector can be used too. The axis of source motion is parallel to the detector and the object plane. The object scanned is penetrated at different angles during the scanning process [96, 100].

5.1 Coplanar translational laminographic geometry

Coplanar laminography is a method used to obtain defect information of objects. In coplanar translational laminography, the radiation source is moved relative to the object and the detector in a plane parallel to the X-ray source. The observation of the object from different positions provides different projection angles. The X-ray source is moved on linear axes as shown in Fig. 13 [96, 131]. The object and detector are positioned in a parallel plane to the scanning axis of the X-ray source, the X-ray source shifts at different angles **ϴ** between -40° to +40° to the detector along the axes **–y** and +**y** in equidistant steps Δ**S**. multiple projections S1, S2 are acquired equidistantly by positioning increments of the X-ray source Δ**S** [131]. The advantage of coplanar translational laminographic geometry is its simple implementation by moving the X-ray source on a single axis.

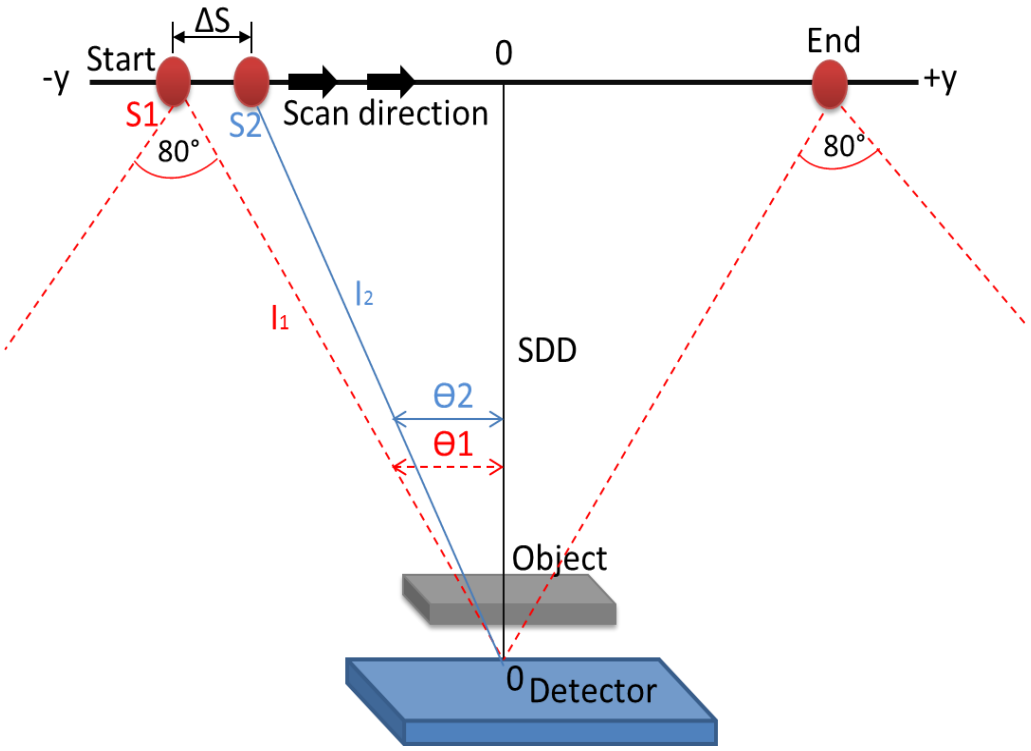

Figure 13: Schematic of coplanar translational laminography geometry [131]

As the radiation source moves from **–y** to **+y** along the y-axis, the detector is in a plane parallel to the y-axis at a perpendicular source-detector distance (SDD). The X-ray source moves in equidistant steps **ΔS** from the **–y** to the **+y**-axis position. The incidence angle **ϴ1** on the

detector for the projection with distance $\boldsymbol{I_1}$ is given by the position **S1** of the X-ray source is expressed as

$$\Theta 1 = \arctan \frac{S1}{SDD} \quad (5.1)\ [131]$$

The distance I_1 between the X-ray source and detector is also expressed as

$$I_1 = \frac{SDD}{cos\,\Theta 1} \quad (5.2)$$

During scanning the X-ray source, the object is penetrated at different angles $\boldsymbol{\theta_i}$ along the scan direction from **–y** to **+y**. The detector pixels receive information of the projected object volume under sequentially changing angles. These projections contain the projected internal structural information of the inspected object [96, 102,104].

5.2 Laminography reconstruction technique

The laminographic reconstruction technique used in this work is the “shift and - add” filtered back projection. This is a mathematical process used to reconstruct 3D volumes from X-ray sequential projections acquired at different scanning positions of the inspected object [104, 105]. The advantage of this reconstruction method is to be able to reconstruct images with the lowest possible noise without affecting image accuracy and spatial resolution [98, 99].

The “shift and-add” filtered back-projection reconstruction uses coordinated motion between the X-ray source and the detector [125, 126]. The co-planar laminography geometry has a fixed object and detector; while the X-ray source is moved at equidistant steps (see Fig. 13 above). The motion constraint has a varied magnification for each point within the object during scanning. The relative motion of a feature projection on the detector is a function of the depth of the features within the object. The object planes that are parallel to the detector can be reconstructed by simply shifting and adding the input images together [96, 112, 115]. As featured in the same plane will lie in the same location on the detector, reinforcing its appearance. Out-of-plane features, however, will appear blurred due to projections varying

locations on the detector. The plane of focus is selected by applying an offset shift to each input projection image before summation [97, 117, 125].

The reconstruction algorithm (TomoPlan) used here works in three steps:

1. First, the projection data is scaled as if it were measured at the plane containing the isocenter.

2. Secondly, the row of each projection is individually filtered. Typically, a ramp filter (in the frequency domain after FFT) is used to remove the radial blurring that occurs during the back-projection process [96, 98]. The filtering is usually done by the multiplication of a function rather than the computational complex convolution process that would be required in the Cartesian domain. For this work, a Hamming window was used to filter the images.

3. Finally, the filtered and weighted data are back-projected over a grid to reconstruct the volume.

The coplanar arrangement of the detector plane and the translational direction of the source allows the application of an efficient shift-averaging algorithm. In this case, translation and summation are the two main parameters required for reconstruction. In the filtered back-projection, the rays of different projections intersect at the original place in space. A position in the object is mapped to different detector positions depending on the position of the X-ray source and mapped to the original position in the space during the back projection. As the distance between the X-ray source and the detector is constant throughout scanning.

In any tomographic reconstruction, the data of measured projections from the detector plane are transformed into the reconstruction space. A numerical shift algorithm with an average over the projections (shift average) enables the calculation of one layer of the laminographic reconstruction volume. This algorithm is applicable with the coplanar arrangement of the detector plane and the translation direction of the radiation source. The acquired projections are added according to the non-linear angle of incidence change, which is parallel to the X-ray source.
The computing time is approximately proportional to the product of the number of projections, number of detector pixels and the number of calculated reconstruction layers. The reconstruction of 200 layers from a data set with 800 projections to 1026 x 252 pixels requires about 85 seconds of computer GPU.

5.3 Summary

The “Shift-and-add” reconstruction uses coordinated motion between the X-ray source, detector and the welded material to acquire the projection images needed for the reconstruction. The relative motion of a feature projection on the detector is a function of the features depth location within the material. Material planes parallel to the detector can be reconstructed by shifting and adding the input projection images together. Features at a plane with constant shift have the same location on the detector, reinforcing its appearance. While the out-of-plane features, however, will appear blurred due to varying shifts in the projections on the detector.

The 3D reconstruction of weld defects of a 3 mm thick aluminium alloy loaded with both Houldcroft and bead-on-plate (BOP) test of base material were successfully obtained with coplanar laminographic technique, see chapter 7.4.

6 Material and Methods

6.1 Setup for real-time in-situ observation

The experimental setup for this research comprises an X-ray source, digital detector and the welded material to perform a real-time observation of crack growth during welding as shown in Fig. 14. This research aims to enable an in-depth understanding of the internal crack formation and propagation using X-rays. During welding of an aluminium alloy, a sequence of radiographs are acquired while irradiating the material at equidistant steps. The results from the acquired 2D radiography are further analysed and compared to post-weld translational laminography data for 3D volumetric studies of the different weld imperfections.

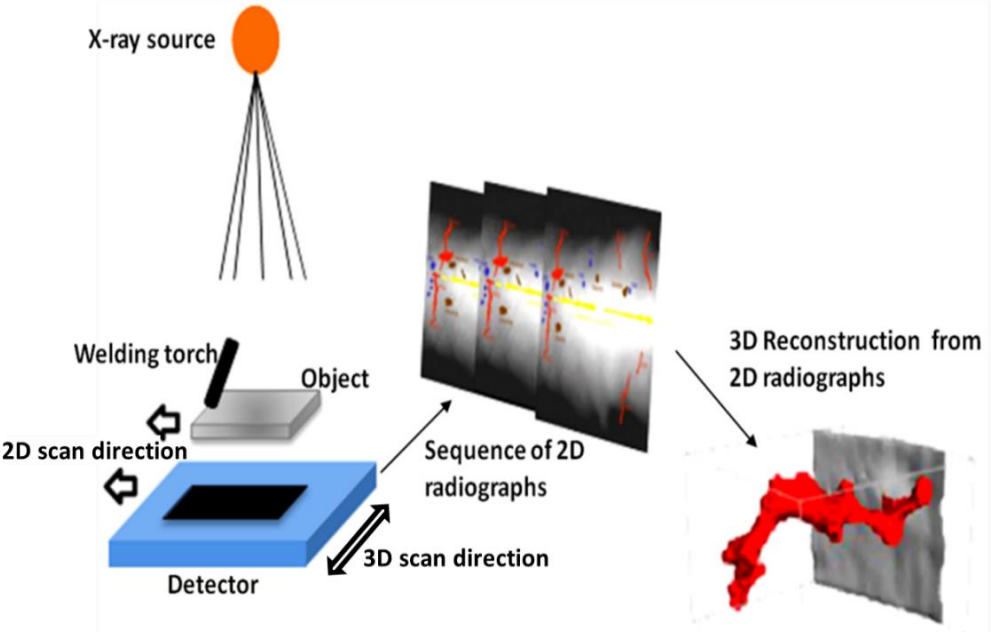

Figure 14: Sketch of the radiographic image acquisition with volume reconstruction

6.2 Shielding case and ceramic fibre insulator

To ensure the protection of the digital detector, a robust shielding case for the digital detector array was built to shield the detector from electromagnetic interference and heat generated by the welding device. The high heat generated by the welding device has to be shielded from the detector. A 5 mm thick aluminium alloy was used to build a protective case of dimensions

300 x 180 mm² as shown in Fig. 15 below. Also included are cooling fans to keep the detector at lower ambient temperature against the heat generated from the ignited welding torch.

A ceramic fibre plate of 20 mm thickness was used as an insulation material against high temperatures and also as a protective material in front of the sensitive area of the detector against metal sparks and weld droplets.

The ceramic fibre contains inorganic fibres of $Al_2O_3\ in\ SiO_2$ chemical compositions with a thermal resistance up to 1800 °C. It is lightweight, strong against thermal shocks and has homogeneous inner structures and low radiographic attenuation.

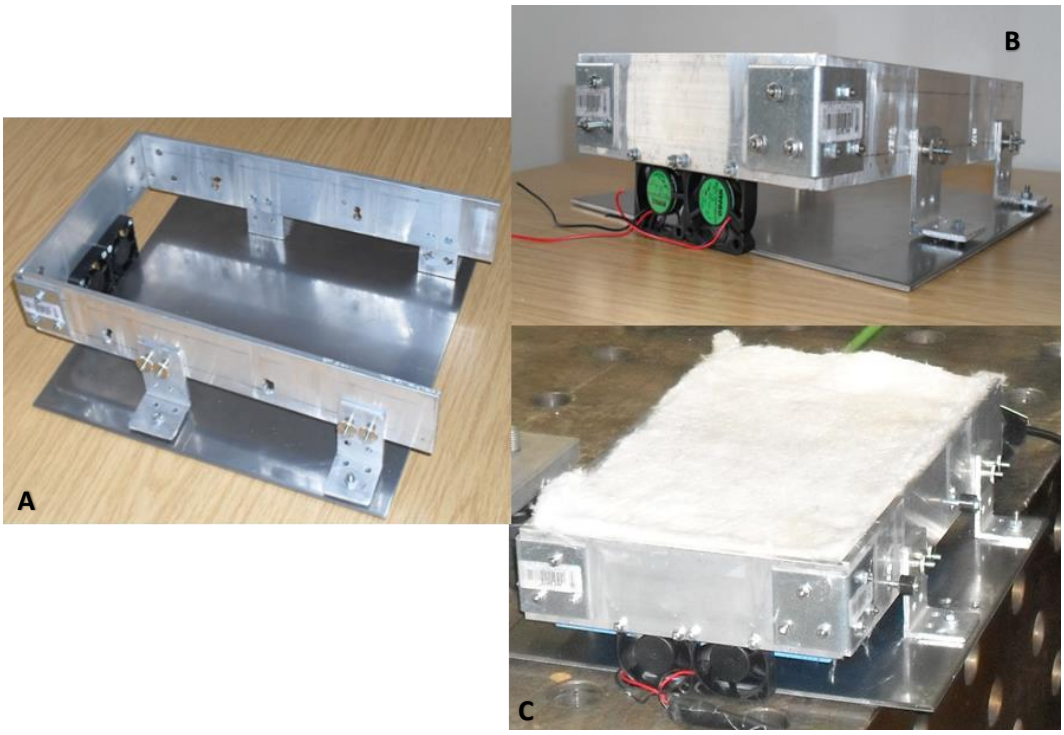

Figure 15: (**A**) Top view of the detector fixed frame, (**B**) End view of detector fixed frame with fans, (**C**) View with 20 mm ceramic fibre for shielding

6.3 Microstep controller and two axes manipulator

An Isel Microstep controller model C 142-4.1 was used as a controller unit for translational movements of the material and detector. It comprises of processor card (UI 5.C-I/O) for controlling two stepper motor axes, a serial RS 232 interface for connection to a computer. It has a positioning speed of 10,000 steps/sec maximum, an operating voltage of 30V and a phase current of 4 Amperes. The micro-step controller was connected to two translational

axes, which was mounted at 90° to the X- and Y- axes. The X-axis was used for the real-time scanning of welding material and detector during welding. The Y-axis was also used for post-weld 3D inspection, see (**e**) in Fig. 16.

6.4 Hot crack observation setup

The in-situ observation of hot crack formations was done with a YXLON X-ray tube Y.TU 225-D04 with a focal spot size of 0.4 mm according to EN12543. A Dexela 1512 digital detector array was also used for the acquisition of the radiographic image sequence during welding. The detector had a 75 µm pixel size and a CsI scintillator above the CMOS detector substrate. These resulted in a basic spatial resolution (SR_b) of 80 µm without binning. The detector has an ADC resolution of 14bits per pixel and readout mode of 10 frames per second at a resolution of 1536 x 1944 pixels. The operating temperature range is between -10 °C and +40 °C with a sensitive area of 145.4 x 114.9 mm^2.

A VarioCam 700 infrared camera was used for temperature distribution measurements of the base material during welding. This is a high definition thermal camera with a resolution of 1280 × 800 pixels with optomechanical Microscan features. It possesses recording and storage of IR frames of up to 240Hz at an accuracy of +/- 1%.

In this research, also a Photron FastCam high-speed optical camera was used for the surface observation of the weld pool region to understand the dynamics of the weld pool. This system provides 1920 x 1440-pixel resolution at a frame rate of 1500 fps with a recording rate up to 75000 fps at a reduced resolution. It utilizes a high-performance CMOS image sensor with a 12-bit range to provide light sensitivity that allows for high-speed recordings. The Photron Fastcam is controlled by a remote LCD keypad over a Gigabit Ethernet network.

The experiment for the observation of hot cracking was carried out by placing the base material (**g**) on a linear motion manipulator (**e**) between the X-ray source (**a**) and the detector (**f**). A series of sequential 2D radiographs are then acquired whilst welding as shown in Fig. 16.

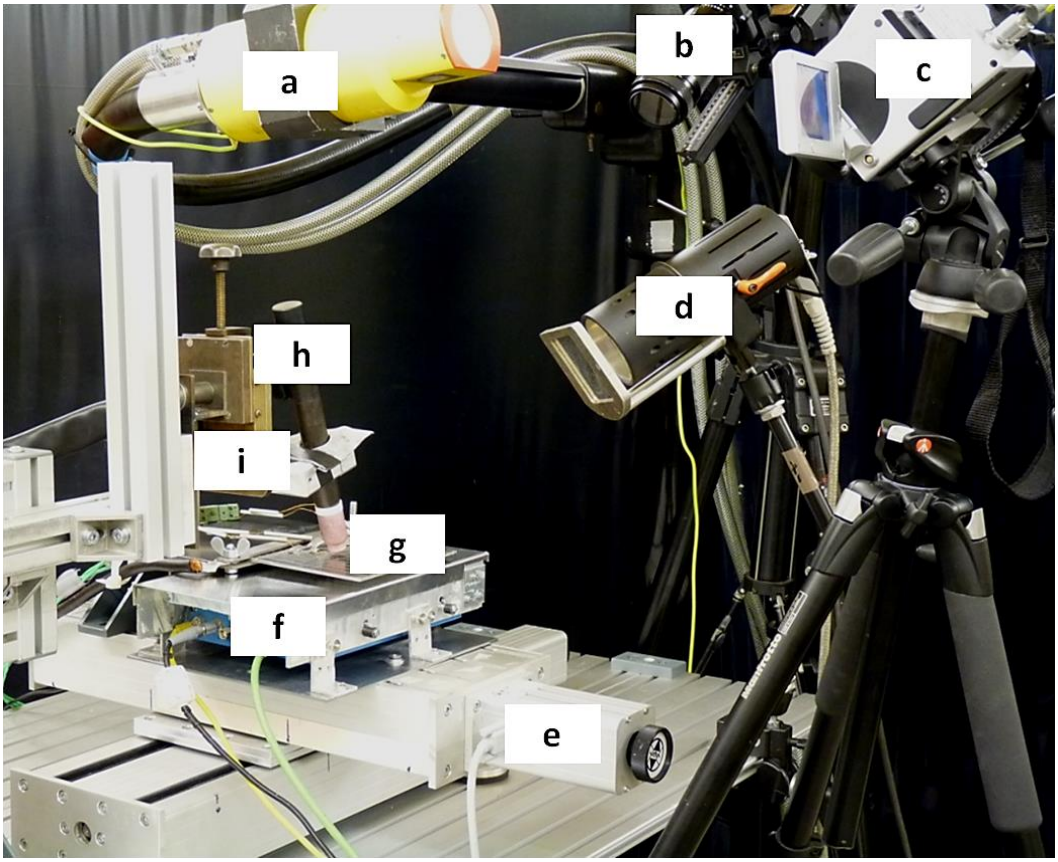

Figure 16: Experimental setup with (**a**) Yxlon X-ray tube, (**b**) Photron Fastcam high-speed optical camera, (**c**) VarioCam 700 infra-red camera, (**d**) Light source for illumination, (**e**) Manipulator, (**f**) DDA in the thermal shielding case, (**g**) Base material holder with a base material, (**h**) Welding torch and (**i**) Welding torch holder

The IR thermography system (**c**) was also used in the experiments, which was a VarioCam 700 infrared camera [132] and the IRBIS 3 software for image acquisition and processing. The VarioCam 700 camera is an upper-class thermal camera for research with a 1280 × 800 pixels resolution that provides razor-sharp infrared recordings. The IR camera uses an internal bandpass filter that allows the detection of the emitted energy in the wavelength range of 5 - 10 μm. This minimizes the interference from arc light and hot tungsten electrodes on the image quality.

The X-ray exposure parameters and radiographic acquisition time used for all aluminium plates are presented in Table 5.

Table 5: X-ray exposure parameters of the 2D image sequences for all aluminium plates

X-ray Voltage	X-ray current	Focal spot d	SDD	ODD	Frame number	Frame time
84 kV	4.1 mA	0.4 mm	426 mm	46 mm	1	0.04 s

An "ISee! Professional" software from Vision–in-X was used for the 2D radiographic image acquisition and DDA adjustment. Image evaluations were done with both "Isee! Professional" and "ImageJ" software [134, 135]. Approximately 1600 sequential projections were acquired at an equidistant movement during welding for different welding speeds of 2.3, 2.8, 3.6, 5.3 and 8 mm/s, respectively. These different welding speeds were selected for heat input that depends on the welding voltage and welding currents, see Table.8. The calculated movement unsharpness of the selected welding speeds was below the detector pixel size of 80 µm as shown in Table 5. An 84 kV X-ray voltage and a source to detector distance of 426 mm were used to avoid image saturation in the base material and to keep the magnification factor below 1.2 (considered as no magnification (M=1) in ISO 17636-2). During welding, series of radiographs were acquired and also the acquisition of post-weld radiographs along the axes **–y** and **+y** in equidistant steps were used for reconstruction purposes by applying a shift average method realized in the BAM software TomoPlan. The cross-sectional visualization analysis was done with VG-Studio MAX software.

The signal-to-noise ratio (SNR) from the acquired 2D radiographic images were measured on a selected region of interest (ROIs) with a size of 20 x 55 pixels. This selected region of interest (ROI) determined the signal intensity and the image background noise. The grey values of the acquired 2D radiographs were also analysed. The grey value response is directly proportional to the radiation dose, which is necessary for the correct determination of $\boldsymbol{SNR}$, $\boldsymbol{SR_b}$ and $\boldsymbol{SNR_N}$. The basic spatial resolution $\boldsymbol{SR_b}$ of the image is the half value of the total image unsharpness $\boldsymbol{u_T}$ measured with a duplex wire IQI at the object according to ISO 19232-5. This is expressed as

$$SR_b^{image} = \frac{u_T}{2M} \tag{6.1}$$

Where $\boldsymbol{u_T}$ is the total image unsharpness and $\boldsymbol{M}$ is the magnification. The total image unsharpness ($\boldsymbol{u_T}$) depends on both inherent unsharpness ($\boldsymbol{u_i}$) of the detector and the geometric unsharpness ($\boldsymbol{u_G}$) of the experimental setup by a convolution as expressed in ISO 17636 as

$$u_T = \sqrt{u_i^2 + u_G^2} \tag{6.2}$$

$$\text{For } u_i = 2SR_b^{detector} \text{ and } u_G = (M - 1)d \tag{6.3}$$

The $\boldsymbol{SOD}$ is the source to object distance, $\boldsymbol{d}$ is the focal spot size of the source and $\boldsymbol{SDD}$ is the source to detector distance. The minimum required source to object distance ($\boldsymbol{f}$) depends on the focal spot size $\boldsymbol{d}$ of the X-ray source, magnification $\boldsymbol{M}$ and the material thickness (l). As the image unsharpness u_g is limited by ISO 17636-2 according to

$$u_g = \frac{1}{7.5}\sqrt[3]{l} \text{ , complying with testing class A of the ISO 17636-2.} \tag{6.4}$$

With reference to the exposure parameters from Table 5, the calculated $\boldsymbol{f}$ according to ISO 17636 is

$\boldsymbol{f}$ = 95.7 mm < SOD = 380 mm at Table 5, at a measured $\boldsymbol{SR_b^{image}}$ **=** 80 µm.

The magnification ($\boldsymbol{M}$) of the setup is obtained from the distances:

$$M = \frac{SDD}{SOD} = \frac{426\ mm}{380\ mm} = 1.12 \tag{6.5}$$

The minimum detectable crack width by X-ray radiography depends on the total unsharpness of the X-ray set-up. The main parameters for detailed visibility in radiography are the contrast-to-noise ratio (CNR) and the Basic Spatial Resolution (SR_b) of the image. The CNR of a small

wall thickness change Δl can be determined from the SNR, which is a function of the effective attenuation coefficient μ_{eff}.

$$CNR = SNR * \mu_{eff} * \Delta l \tag{6.6}$$

$$SNR_N = \frac{SNR * 88.6\ \mu m}{SR_b} \tag{6.7}$$

The SNR_N depends on the exposure conditions and the Basic Spatial Resolution (SR_b) of the image.

For the testing of welded alloys, a testing class A was achieved and not testing class B. This is, as a result, the short frame exposure time of 40 ms for real-time data acquisition to guarantee a minimum normalized SNR of 100.

6.4.1 Movement unsharpness and resolution

In addition to the geometrical unsharpness consideration discussed in chapter 6.4, there is another unsharpness caused by the movement of the object and detector. The quality of a radiographic image is influenced by image resolution and unsharpness because of the shift in the position of the object.

The movement of the object and detector causes the movement unsharpness. The movement of the focal spot, as illustrated in Fig. 17 causes the penumbra of a feature in the image.

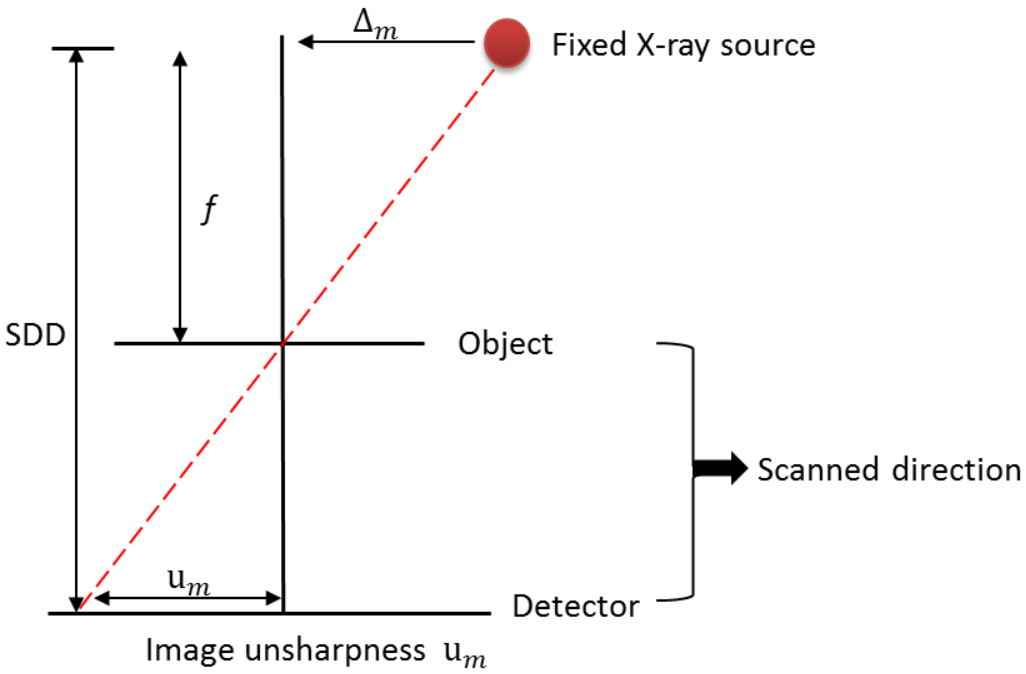

Figure 17: Movement unsharpness u_m schematics for a moving source

The movement unsharpness is generally dependent on the geometrical magnification as expressed in Eqn. 6.8.

The geometric unsharpness in the image is determined as

$$u_G = (M - 1)\, d \tag{6.8}$$

In addition, the movement unsharpness is deduced as

$$u_m = \Delta t\, (M - 1)\, v \tag{6.9}$$

Where M is the magnification, v is the velocity of the base material in mm/s and Δt is the 40 ms frame exposure time.

The movement unsharpness was calculated from Table 5, with a magnification of 1.12. The values for the movement unsharpness for the respective welding speeds are listed in Table 6 for each welding speed.

Table 6: Movement unsharpness of different welding speeds

Welding speeds (mm/s)	*Movement Unsharpness U_m (mm)*
2.3	0.010
2.8	0.013
3.6	0.016
5.3	0.024
8	0.036

The determined movement unsharpness as seen in Table 6. is considerably smaller than the detector basic spatial resolution of 0.08 mm and this can be neglected.

6.4.2 Base materials and welding process

The aim of welding is to generate a good welding quality free of defects. However, defects in welds are inevitable. This makes it necessary to study and understand the process of welding and the influence of the base materials chemical composition on the causes of weld defects.
An automatic Gas Tungsten Arc Welding (GTAW) process was chosen in this work. In the GTAW process, an electrical arc is created between a tungsten electrode and the base material. An inert gas of argon was used to protect the metal against oxidation. Before welding, the base material was clamped on both edges. A fusion line was made with GTAW on the aluminium base material along a longitudinal direction. However, the arc weld torch was placed at a fixed position while the base material was translated along a longitudinal direction at varying speeds.
The five Aluminium alloys used for this research are known for their applications in automobile industries, aircraft, shipbuilding and plant constructions as listed in Table 9.
The selected aluminium alloys are Al99.5 (EN AW 1050A), AlMg4.5Mn0.7 (EN AW 5083), AlMg (EN AW 5059), AlMgSi0.5 (EN AW 6060) and AlSi1MgMn (EN AW 6082). The base material thickness was 3 mm for each alloy with a dimension of 150 x 150 mm². The chemical compositions of these five alloys were measured with an ARL iSpark Series optical emission spectrometer; the results are presented in Table 7:

Table 7: Chemical composition of investigated Al alloys in w %

Alloys	Chemical composition in wt.-%									
	Si	**Fe**	**Mn**	**Mg**	**Zn**	**Ni**	**Ti**	**Cr**	**Cu**	**Al**
Al 99.5 (EN AW 1050)	0.25	0.40	0.05	0.05	0.07	-	0.05	-	0.05	99
AlMg (EN AW 5059)	0.19	0.16	0.28	1.39	-	-	-	-	0.09	98
AlMgSi0.5 (EN AW 6060)	0.42	0.23	0.05	0.49	0.009	0.002	0.017	-	-	99
AlSi1MgMn (EN AW 6082)	0.70	0.50	0.40	0.60	0.20	-	0.10	0.25	0.10	97
AlMg4.5Mn0.7 (EN AW 5083)	0.40	0.68	0.40	4.46	0.25	-	0.15	0.05	0.10	94

To study crack initialisation during welding different geometrical designs were used. A bead-on-plate (BOP) technique as shown in Fig. 19 and Houldcroft (also known as Fishbone technique) shown in Fig. 21 were adopted. These welding techniques were used to study the crack susceptibility of the alloy. The adopted operating conditions were to ensure complete melting of the base material as given in Table 8. The welding current was also increased to compensate for the increasing welding speeds. This was to ensure the maximum heat input needed for the complete melting of the base material, thereby initiating hot cracks.

The alloys were welded with argon gas as the shielding gas at a gas flow rate of 16 l/min. A 2.4 mm diameter tungsten electrode was used. The electrode was positioned at an angle of 30° to the base material and powered with an AC polarity (of 80% negative, 20% positive) with a frequency of 50Hz. The welding parameters used are presented in Table 8.

Table 8: Welding parameters used

Weld Parameters	**Exp1**	**Exp2**	**Exp3**	**Exp4**	**Exp5**
Voltage ($\boldsymbol{U}$) in V	16	16	16	16	16
Current ($\boldsymbol{I}$) in A	120	130	140	165	180
Speed ($\boldsymbol{v}$) in mms^{-1}	2.3	2.8	3.6	5.3	8.0
Heat input (kJ/mm)	835	743	622	498.11	360

Table 9: Applications and properties of selected aluminium alloys

Alloy	Applications	Properties
Al-99.5% [EN AW 1050]	Tanks, boilers, rivets condenser blades & nuclear applications	Low mechanical strength, high ductility, high electric & thermal conductivity
AlMg [EN AW 5059]	Automotive parts, marine application	High formability, high strength
AlMgSi0.5 [EN AW 6060]	Architectural sections, lightings, furniture	Medium strength, complex sections, anodizing quality
AlSi1MgMn [EN AW 6082]	Machining, forgings, tools	Heat treatable alloys (soft temper), atmospheric corrosion resistance
AlMg4.5Mn0.7 [EN AW 5083]	Heavy-duty structures, hydraulics systems, marine & offshore	Good machinability, high corrosion resistance

Four thermocouple elements were spot-welded onto the base material to determine the temperature distribution of the weld pool, see Fig. 18.

The thermocouple elements were placed at 40 mm distance between each other along the longitudinal direction of the weld seam at 10 mm distance from the edge of the base material as shown in Fig. 18. A NI 9213, 16 channel, 24-bit thermocouple data acquisition system was used for temperature distribution recordings.

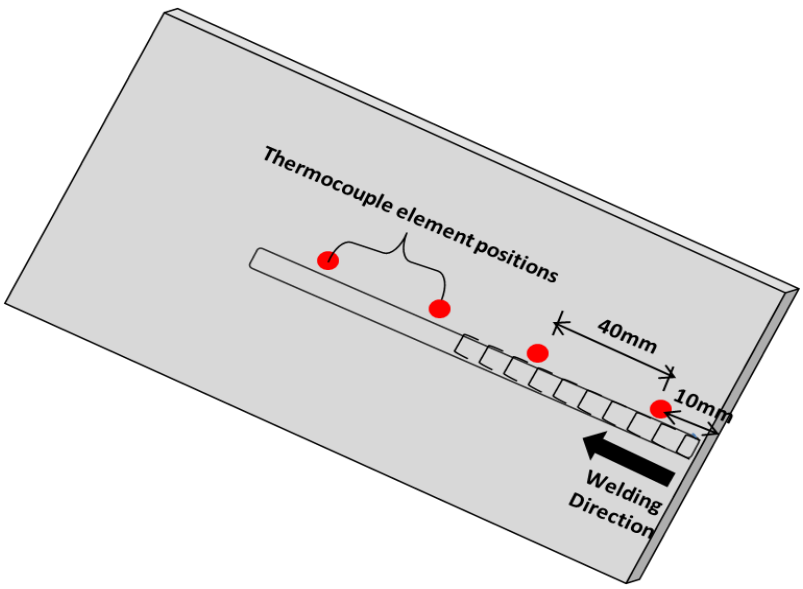

Figure 18: Sketch of bead-on-plate (BOP) test layout with thermo-couple elements positions

In addition, the thermophysical properties of the alloy in Table 10 were used to determine the cooling rate and solidification rate of the alloys.

Table 10: Thermophysical properties of Al alloys at 32°C

Material	Thermal Conductivity (W/mK)	Density (ρ) (g/cm^3)	Specific Latent Heat(J/kgK)	Thermal Diffusivity (m^2/s)
Al_99.5% [EN AW 1050]	205	2.707	896	$84\ x\ 10^{-6}$
AlMg [EN AW 5059]	177	2.770	875	$73\ x\ 10^{-6}$
AlMgSi0.5 [EN AW 6060]	117	2.707	892	$73\ x\ 10^{-6}$
AlSi1MgMn [EN AW 6082]	161	2.627	854	$71\ x\ 10^{-6}$
AlMg4.5Mn0.7 [EN AW 5083]	121	2.660	900	$49\ x\ 10^{-6}$

The Houldcroft test (HCT) is a commonly used test for understanding the phenomena of crack initialisation and growth during welding. Houldcroft test (HCT) is a well-known crack sensitivity test for understanding the impact of strain exerted through the different slot lengths in the base material [7, 42]. As shown in Fig. 19, the Houldcroft test (HCT) has several saw cut slots of different lengths on both sides of the alloy.

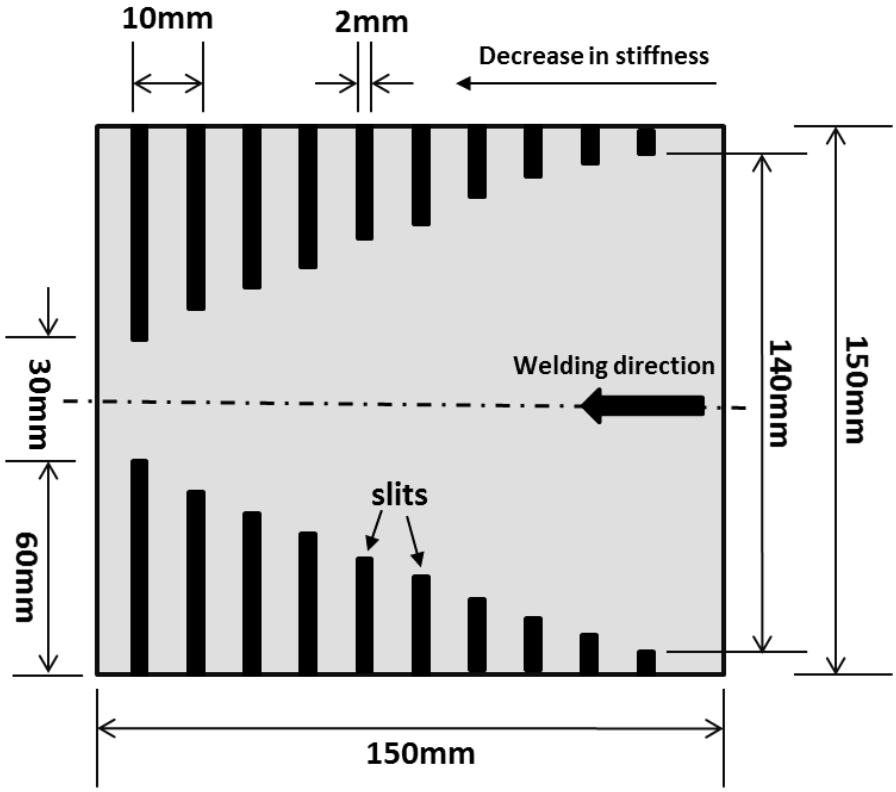

Figure 19: Sketch of Houldcroft test (HCT)

These saw cuts slots reduce the stiffness along the welding direction. This is used to determine the crack growth position to its welding conditions. During welding, the weld pool moves inwards along the centreline, where the cracks propagate due to thermal tensile stress.
Eqn 6.10 determines the crack sensitivity of the weld.

$$A = \left(\frac{l_t}{l_0}\right) * 100\% \tag{6.10}$$

A= crack sensitivity %, l_t = crack length (mm) and total weld length l_0 =100 mm

This is also necessary for the determination of the crack growth rate. The observed crack sensitivity range of all aluminium alloys was between 50% to 75% of the total crack length of 100 mm.

6.5 Summary

The in-situ observation of hot crack formations was done with a radiation source from YXLON (X-ray tube Y.TU 225-D04) with a focal spot size of 0.4 mm. A Dexela 1512 digital detector array was used for the acquisition of sequential radiographic images during welding. The detector had a 75 µm pixel size and a CsI scintillator on a faceplate above the CMOS detector substrate. This resulted in a basic spatial resolution (SR_b) of 80 µm for this detector.

The experiment of digital radiography for hot crack observation was done by placing the base material on a linear motion manipulator between the X-ray source and detector.

The five Aluminium alloys selected for this research are notably known for their applications in automobile industries, aircraft, shipbuilding and plant constructions. The selected alloys are Al99.5 (EN AW1050), AlMg4.5Mn0.7 (EN AW5083), AlMgSi0.5 (EN AW6060) and AlSi1MgMn (EN AW6082). A base material of 3 mm thickness was used for each alloy with dimensions of 150 x 150 mm^2. The geometrical design of test base materials was to enforce crack initialization during welding. In this investigation, a bead-on-plate (BOP) and Houldcroft test (HCT) was adapted. These welding tests are known from crack susceptibility investigations that depends on surface tension, temperature distribution and the dynamics of liquid rupture on crack susceptibility.

An additional factor for image unsharpness during welding is the unsharpness caused by the movement of the digital detector and welded material. The quality of a radiographic image is influenced by the total image resolution and unsharpness. This causes degeneration in image quality. The contribution of movement unsharpness for all the selected welding speeds, with the magnification of 1.12 for the welded material thickness as shown in Table 6 is negligible.

7 Results and Discussions

This chapter contains the experimental results and highlights the influence of welding parameters on the hot cracking susceptibility of aluminium alloys. In addition, the observation of the weld pool structure with X-ray, computed tomography and high-speed camera of all welds are also discussed. Furthermore, the difference in crack lengths and temperature distributions from both measurements using infra-red camera and thermocouple elements are also presented in this chapter.

7.1 Weld pool observation and crack growth for bead-on-plate and Houldcroft tests

The visualization and determination of the weld pool shape (i.e. mushy zone), crack initialization and propagation were observed during welding with both X-rays and an optical high-speed camera.

During a single pass welding, a highly concentrated heat source melted the base material. This caused a complete melting of the aluminium alloy at the heat-affected zone. The motion of liquid viscosity of the weld pool influenced the thermal phenomena during welding (refer to subchapter. 3.3.4). The buoyancy forces in the melted zone of the weld pool drove the liquid motion.

The real-time observation of the weld pool was carried out with both Photron high-speed camera for the surface investigation of the weld pool and the X-ray set-up for in-situ observation of the mushy zone as shown in Fig. 20. The weld pool region, as explained in chapter 3, consist of the three main fundamental features (i.e. liquid, mushy and solid zone).

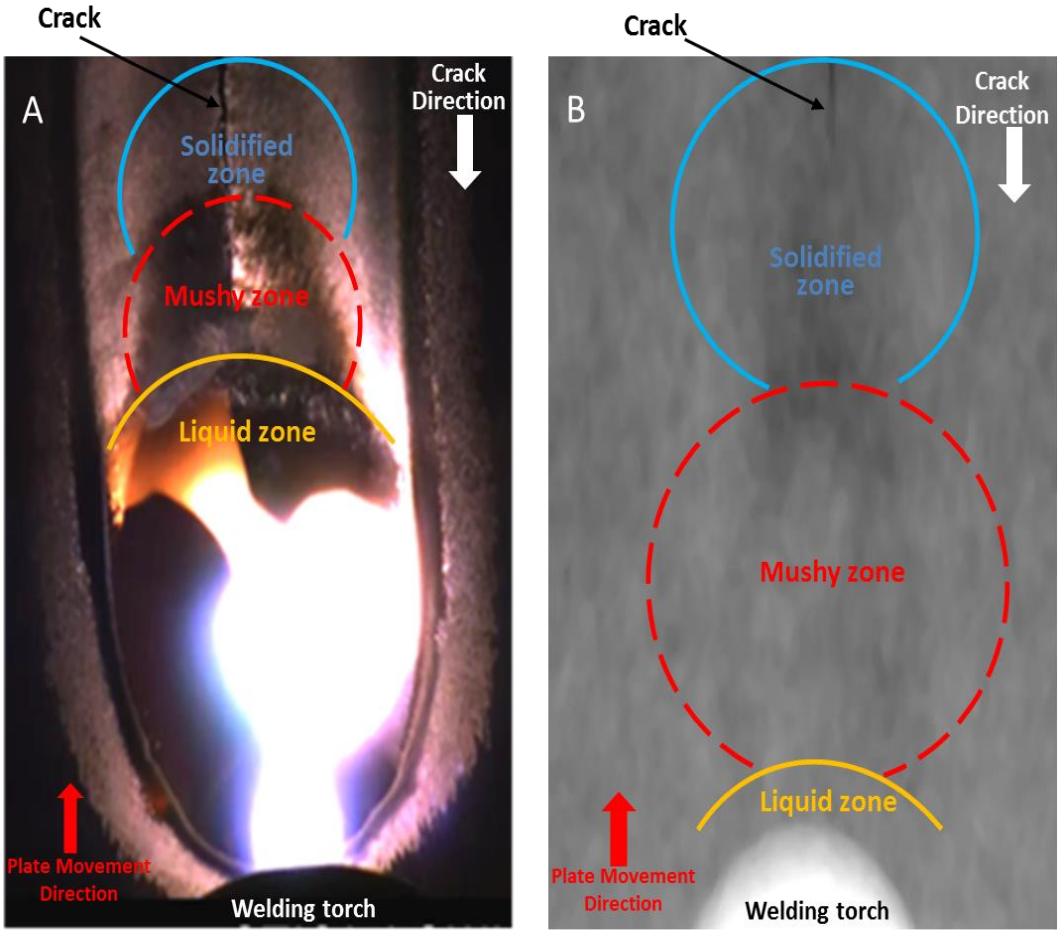

Figure 20: Real-time observation of the heat-affected zone (mushy zone) with Photron high-speed camera (A) and (B) X-ray in-situ observation raw data

The crack tip distance from the mushy zone and the difference in crack lengths from the two observatory methods are shown in Fig. 21 and Fig. 22 below respectively. The determination of other weld defects such as porosity was possible with X-ray observation.

The observation of crack formation was initialised after 20 seconds of welding without movement of both welded material and the detector (refer to Fig. 14). This was to ensure complete melting of the aluminium alloy to facilitate crack initialisation during solidification of the weld pool.

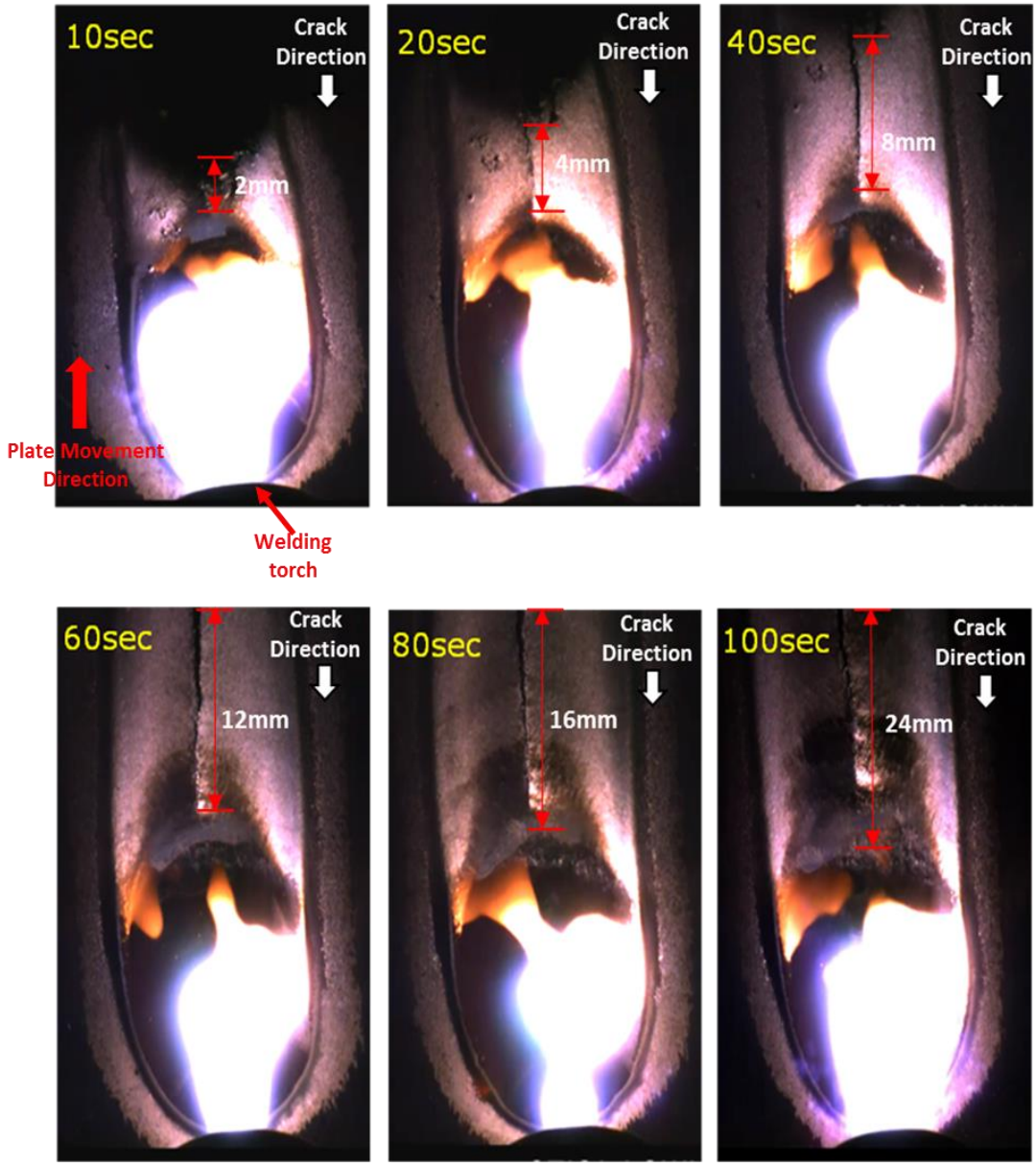

Figure 21: Crack growth during welding observed with Photron high-speed camera (field of views limited)

The initial crack tip manifested after the weld pool had undergone thermal expansion and contraction during the transformation of the solidus-liquidus interface.

In fusion welding, the interaction between the base material and the heat source led to the heat transfer and melting of the weld material. In the melting region, the circulation of molten was driven by the elasticity of the alloy because of surface tension gradient, liquid impingement, friction and electromagnetic forces of the weld. The resulting heat transfer, fluid flow and cooling rate of the weld pool influenced the temperature distribution in the weld material.

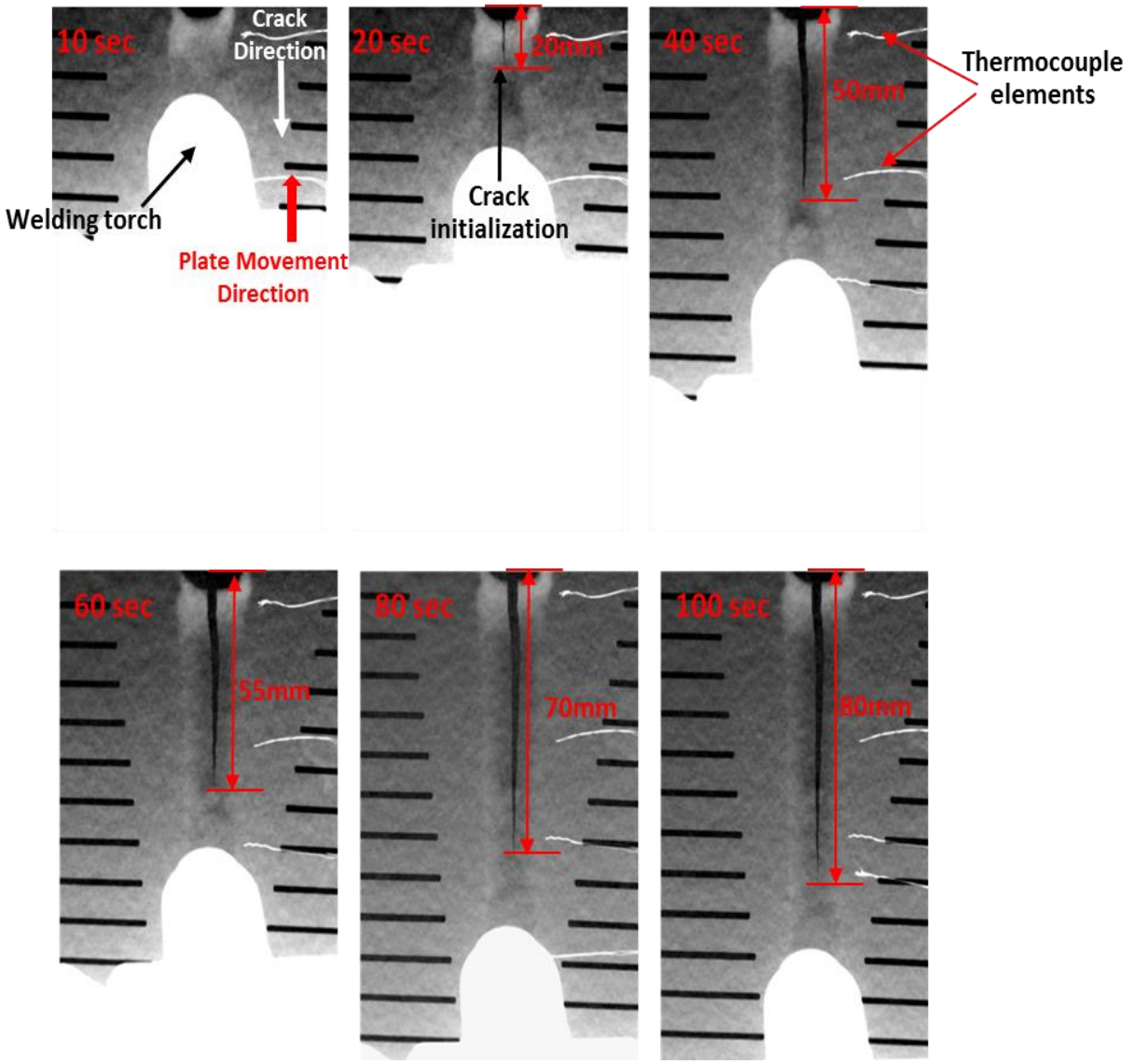

Figure 22: Real-time in-situ X-ray observation of crack growth following the welding torch (WD) during welding with respective timestamps

The difference in temperature with time, also regarded as the thermal cycle influenced the microstructures, residual stresses and weld distortions within the weld material. During welding, the weld pool, experienced loss of alloy elements by evaporation such as oxygen gas and this had an adverse influence on the thermal cycle of the weld.

The crack tip measurements from the mushy zone were done as illustrated in Fig. 23 and the results for all the welding speeds are listed in Table 11. This was to verify the crack growth rate and the solidification rate with the welding parameters (i.e. welding speed).

The advantages for the inspection of crack initialisation and propagation with X-rays over visual surface inspection by the Photron high-speed camera are

- Visualisation of the complete weld pool region is only possible by X-rays, see Fig. 22. The dynamic of the Photron high-speed camera avoids the inspection of the complete weld pool region, see Fig. 21. The detection of the crack tip in the images from the Photron high-speed camera cannot be performed due to the high image contrast.
- The rim of the mushy can be enhanced by high pass filtration on the 2D radiographs for clear visualisation, see Fig. 23. Therefore, only in the filtered 2D radiographs is possible to measure the crack tip distance reliably.

The average distances of the crack tips to the mushy zone of the weld pool for bead-on-plate and Houldcroft tests are listed with their respective welding speeds in Table 11.

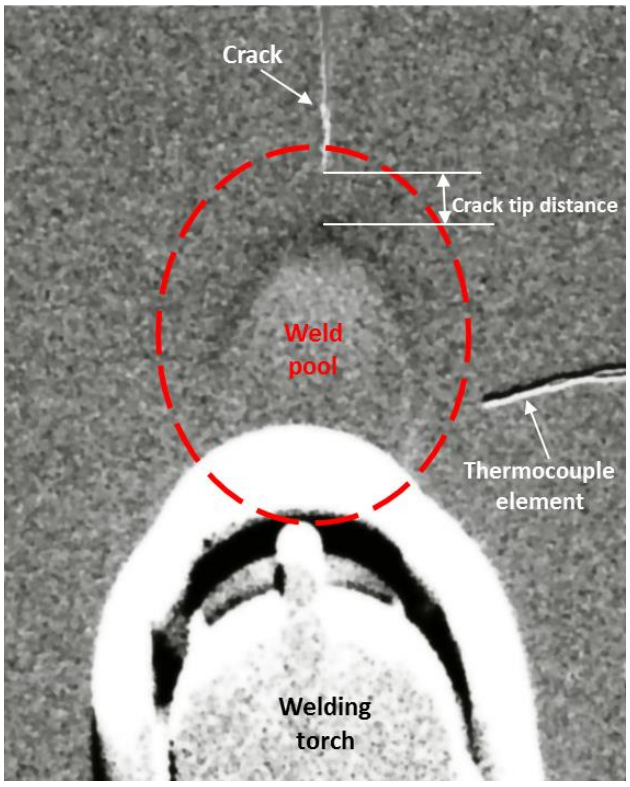

Figure 23: Determination of crack tip distance from the mushy zone (shown only after high pass filtering)

Table 11: Measured average (of all alloys) distances between the crack tip and the rim of the mushy zone

Welding speeds (mm/s)	Distances at bead-on-plate test (mm)	Distances at Houldcroft test (mm)
2.3	2	2.5
2.8	1.8	2.3
3.6	1.5	2
5.3	1.2	1.6
8	1	1.2

From Table 11, it can be seen that the distances between the crack tip and rim of the mushy zone are always at least 20% larger for the Houldcroft test compared to the bead-on-plate test. Due to the saw slots of the Houldcroft test the inner strain in the weld material is reduced compared to the bead-on-plate tests. Therefore, crack initialisation is started later resulting in a larger distance between the crack tip and rim of the mushy zone.

7.2 Thermal phenomena of the mushy zone

The temperature field on the weld material was measured to determine the different analytical models of the heat transfer. The analytical models relate to the moving heat source, which gives a two-dimensional temperature field for the weld material. The surface temperatures distributions recorded with infra-red thermography and thermocouple elements during welding were also compared. The infra-red camera was focused on the mushy zone of the weld pool, while the thermocouple elements were spot welded along the weld seam at 1 cm from the weld pool as shown in Fig. 18. These elements were used to measure the temperature distribution along the weld seam and to determine the cooling rate. This was also useful for the determination of the coherency temperature. (see subchapter 3.2.1).

In Fig. 24, are the thermographic images of the weld seam are shown with its respective welding time. Note: the welding torch warms up the detector heat insulation beneath the bead-on-plate piece partially.

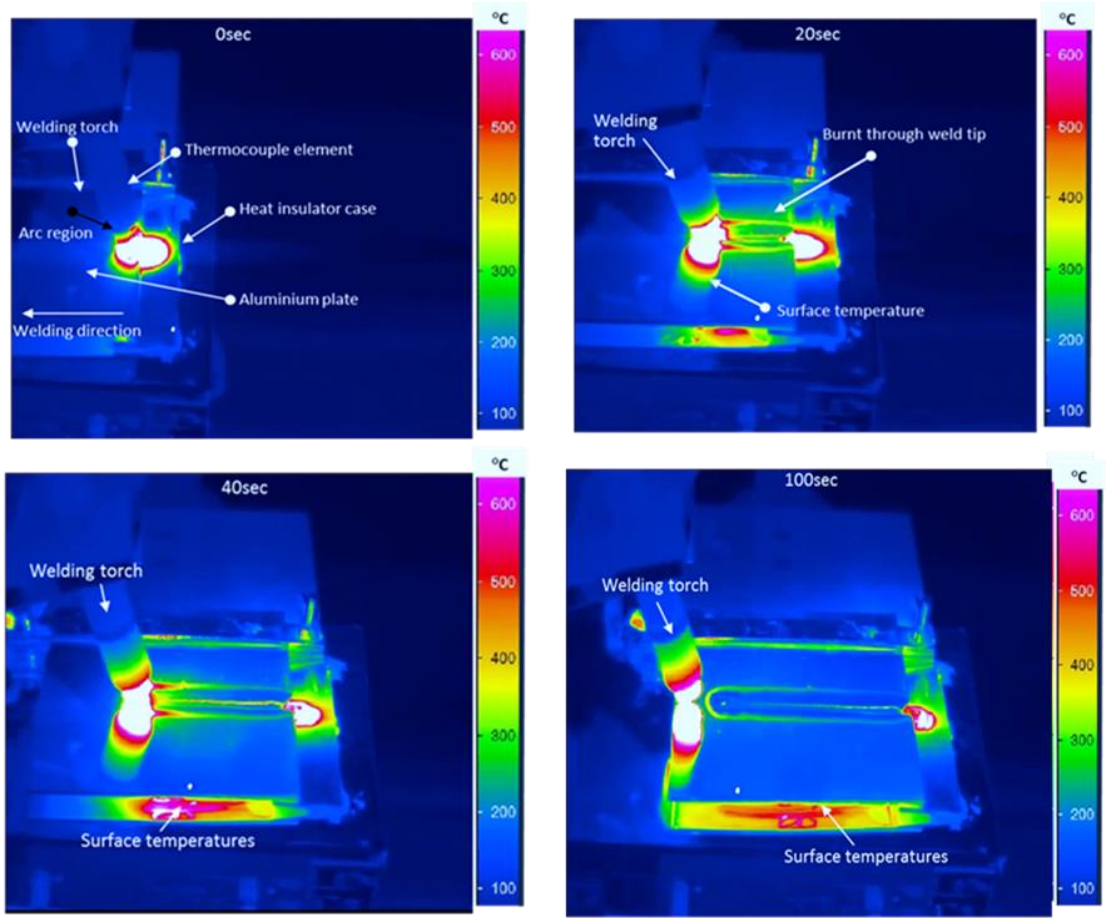

Figure 24: Thermograms showing the impinging process of weld pool dynamics and temperature distribution of bead–on–plate welding (no mushy zone visible)

The temperature distributions measured with the infra-red camera were compared to the data from the thermocouple elements to determine the temperature variations.

Prokhorov [45] explained the relationship between the heat input applied during welding and hot crack formation (refer to chapter 3).

In Fig. 25, the heat induction from the heat input is shown in relation to the welding speed.

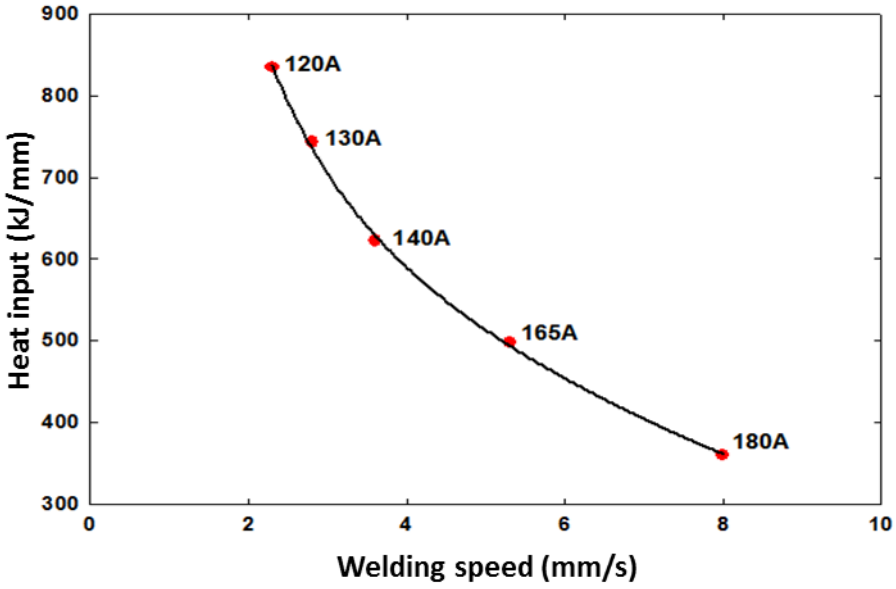

Figure 25: Heat input to weld alloy for different welding speeds and welding currents

The cooling rate of the weld is increased by increasing the welding speed, which results in a decrease in the heat input. This explains the high heat input for 120A welding current due to a slower welding speed.

In Fig. 26 below the temperature-time curves are shown for both thermocouple elements and the infra-red camera. The welding of the alloys started 30 s after temperature acquisition.

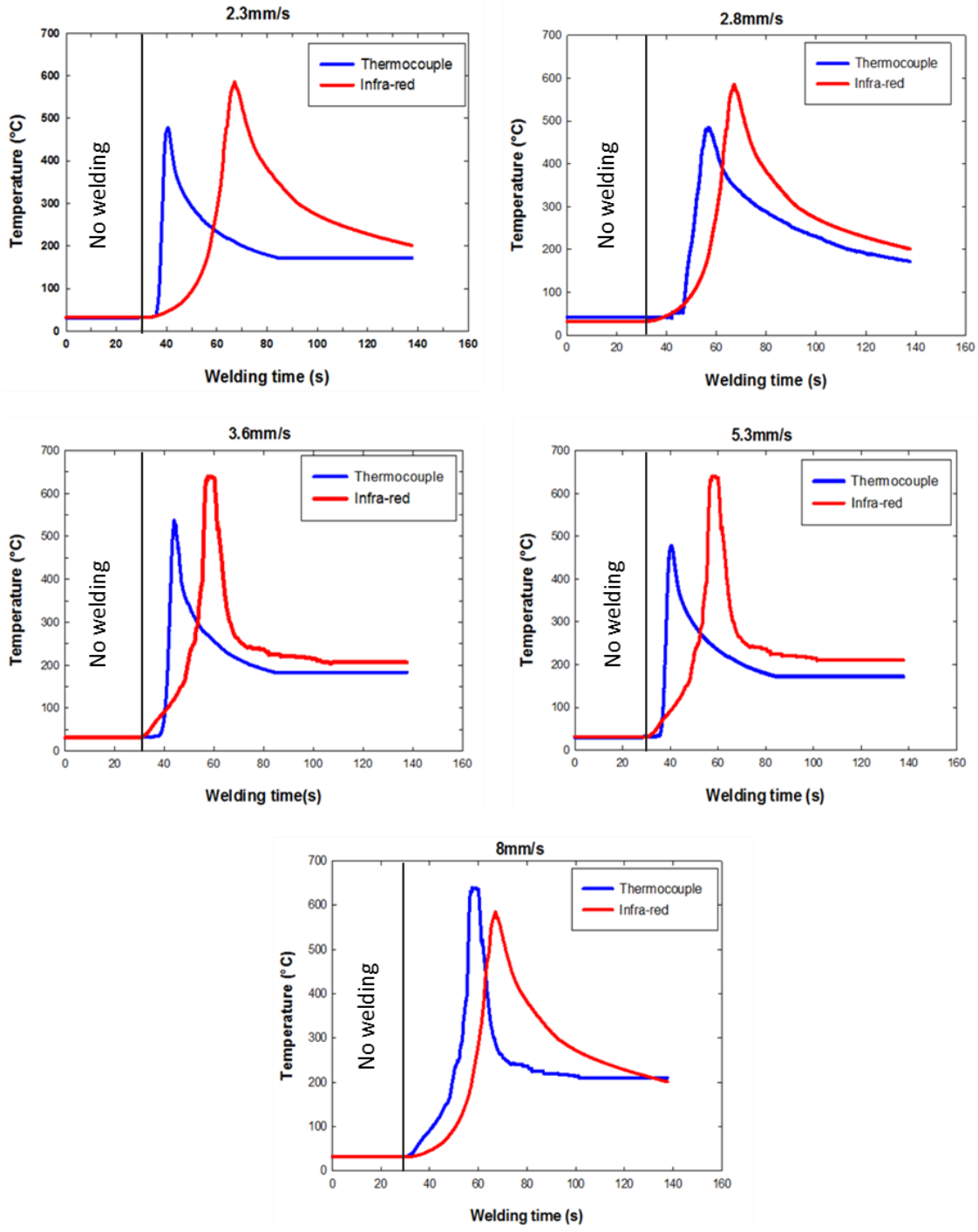

Figure 26: Temperature time dependencies of the measurements using thermocouple element (number 2) and the centre position of the infra-red camera (averaged over all alloys)

As the weld material was completely melted after 2 seconds of welding, the two temperature measuring devices registered a fast rise of the local temperature during welding.

However, it was noted that the peak temperature for all the different welding speeds had a delay between the thermocouple and infra-red recordings. This time delay between the peak temperatures curves was due to the different locations of measurements. The temperature distribution measurement with a thermocouple was taken at the edge of the weld seam. The measurement with an infra-red camera was taken from the middle of the weld seam. This shift in position is reflected by the time shift of the peak temperatures measured. The temperature curve for welding speed 2.3 mm/s recorded peak temperatures of 480 °C and 600 °C for thermocouple and infra-red camera respectively. The temperature recordings with Infra-red camera and the second thermocouple element for the welding speeds 2.8 mm/s are ($\mathrm{T}_{\mathrm{thermocouple}} = 500\,°C$ and $\mathrm{T}_{\mathrm{infra-red}} = 600\,°C$), for 3.6 mm/s ($\mathrm{T}_{\mathrm{thermocouple}} = 550\,°C$ and $\mathrm{T}_{\mathrm{infra-red}} = 650\,°C$), for 5.3 mm/s ($\mathrm{T}_{\mathrm{thermocouple}} = 500\,°C$ and $\mathrm{T}_{\mathrm{infra-red}} = 650\,°C$) as 8 mm/s measured ($\mathrm{T}_{\mathrm{thermocouple}} = 650\,°C$ and $\mathrm{T}_{\mathrm{infra-red}} = 600\,°C$) respectively. It was observed that the infra-red camera recorded lower peak temperatures than the thermocouple element for a welding speed of 8 mm/s. This was caused by adjustment problems in the experimental setup.

7.2.1 Cooling rate results

The cooling rate of a weld depends on the welding current, welding voltage and welding speed in the tungsten arc welding process. The heat input was selected to be inversely proportional to the welding speed see Fig. 25.

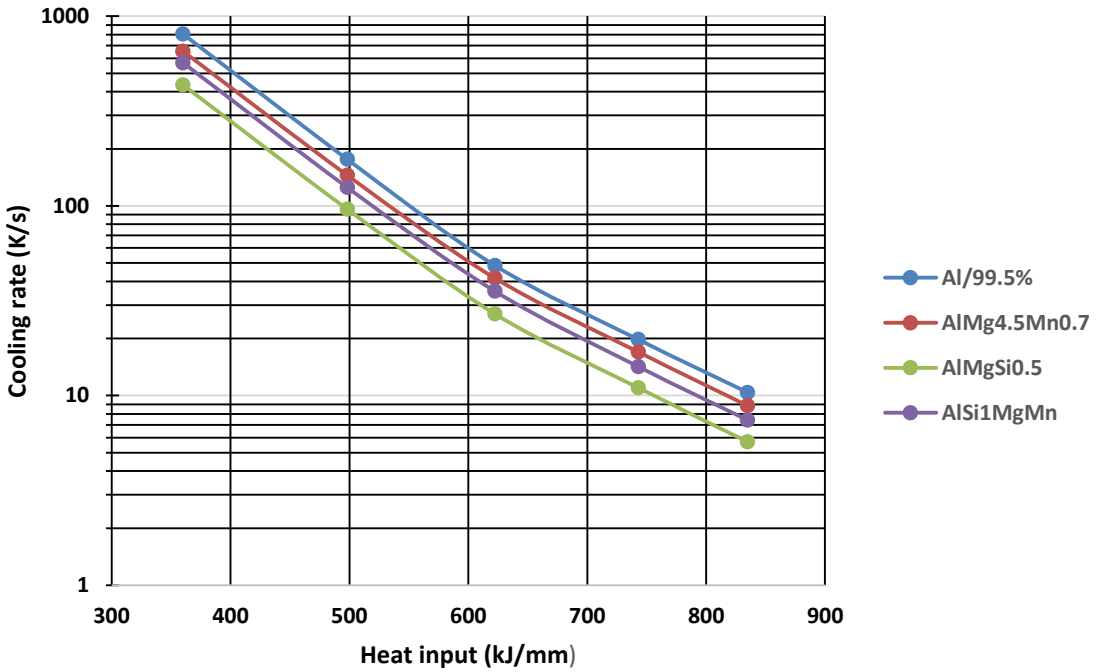

Figure 27: Cooling rate of the tested aluminium alloys (welding of AlMg alloy does not show cracks and it is not shown here)

The cooling rate was determined from Fig. 26 using an exponential fit from the peak temperature to the 1/e decayed temperature value and the period between both temperatures.

As seen in Fig. 27, the cooling rate with respect to the heat input shows the differences between the alloys. As the welding speed increases, the heat input decreases due to less arcing time in the region of the welded material. As the cooling rate depends on the thermal conductivity of the alloy.

7.2.2 Discussion

As a major outcome, it was discovered that for a correct measurement of the crack tip distance to the rim of the mushy only the high pass filtered X-ray projection has to be used.

The measured distance between the crack tip and the rim of the mushy zone for both the Houldcroft test and bead-on-plate are shown in Table 11. At 2.3 mm/s, the distance between the crack tip and the rim of the mushy measured 2 mm and 2.5 mm for bead-on-plate and Houldcroft rest respective. The distance between the crack tip and the rim of the mushy zone reduces with increasing welding speed. As the welding speed increases, the heat input decreases due to less arcing time in the region of the welded material resulting in an increasing solidification rate.

The measured distances between the crack tip and the rim of the mushy zone were at least 20% larger for the Houldcroft test than the bead-on-plate test. This is due to the inner strain caused by the saw slots of the Houldcroft test. The temperatures at welding speed 2.3 mm/s recorded peak temperatures of 480 °C and 600 °C for thermocouple and infra-red camera respectively. It was also observed that the infra-red camera recorded higher temperatures than the thermocouple elements for welding speeds 2.3 mm/, 2.8 mm/s, 3.8 mm/s and 5.3 mm/s except for welding speed 8 mm/s. The infra camera recording is at least 5% higher than the thermocouple element. This is because the temperature distribution recorded with the infra-red camera was taken from the mushy zone whilst the temperature measurements with thermocouple elements were taken at the weld boundary.

7.3 Crack growth measurements on Houldcroft samples

For crack initialisation, the weld material was heated for 2 s at the plate edge before the movement of the aluminium plate at a constant speed. During this 2 s heating of the aluminium plate, no crack was formed. The manifestation of crack occurred when the welding plate moved and the weld seam underwent solidification as seen in Fig. 21 and Fig. 22.

The time-dependent analysis of the crack growth shows crack initiation appearing after 20 seconds of welding of the base material. The initial crack tip manifested after the weld pool had undergone thermal expansion and contraction during the transformation of the solidus-liquidus interface. The rate of crack growth depends on the welding speed, which influenced the cooling rate of the welding process. The alloys Al-99.5%, AlMgSi0.5, AlMg4.5Mn0.7 and AlSi1MgMn exhibited crack initiation after 20 seconds of welding and the crack grew follows the welding torch. The AlMg alloy does not develop cracks.

7.3.1 Crack growth results

As seen in Fig. 28, for 120A welding current at 2.3 mm/s welding speed, the crack growth shows differences in crack length among all alloys with AlSi1MgMn (measuring the crack length of 8 cm), whilst alloys Al-99.5% and AlMgSi0.5 at measured crack lengths of 7.2 cm and 7.4 cm respectively.

Fig. 28, Fig. 29, Fig. 30 and Fig. 31, shows the comparison of crack lengths for all welded aluminium alloy with their respective welding speeds. These uncertainties and inconsistencies are common in the crack lengths determination of welds.

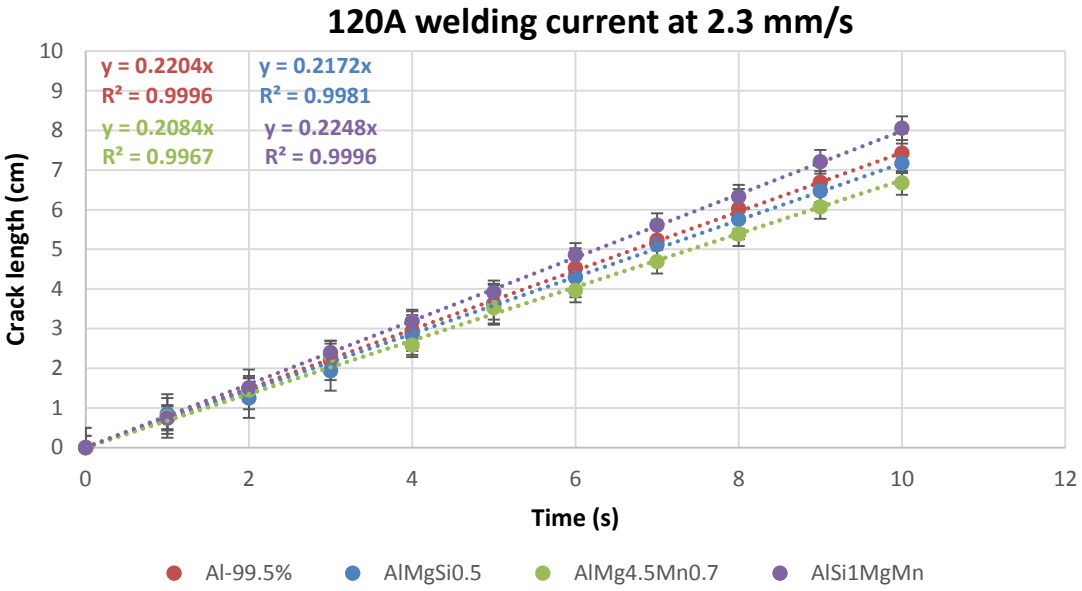

Figure 28: Crack length determination in relation to welding current 120A

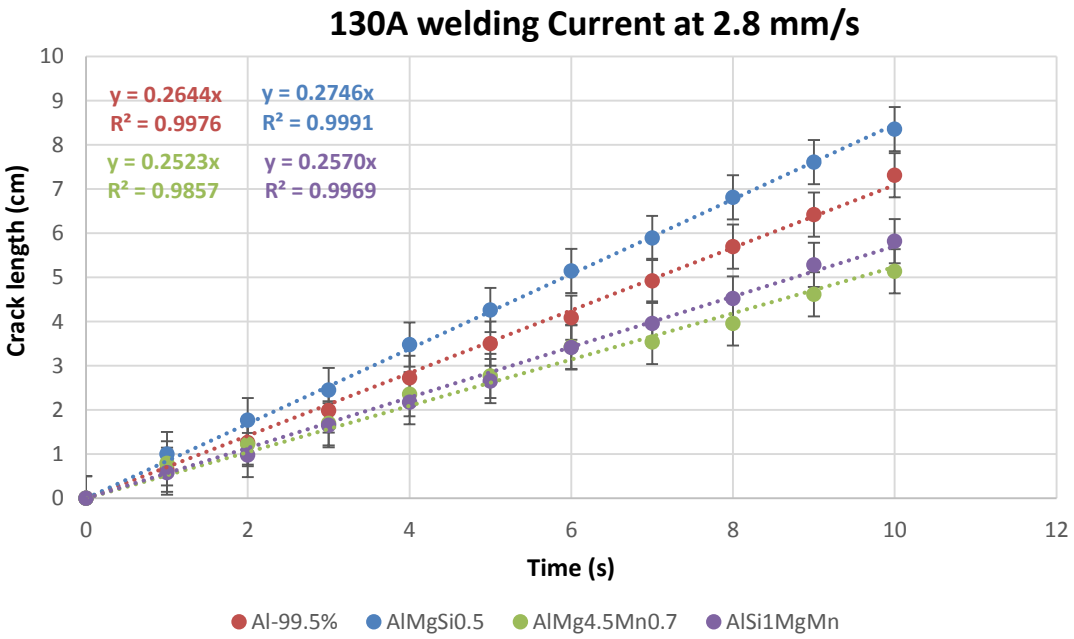

Figure 29: Crack length determination in relation to welding current 130A

The reason for the inconsistencies in crack lengths is attributed to misalignment of the weld base material under the welding torch, as well as the alloys chemical composition and the welding design (refer to Subchapter 3.2.2).

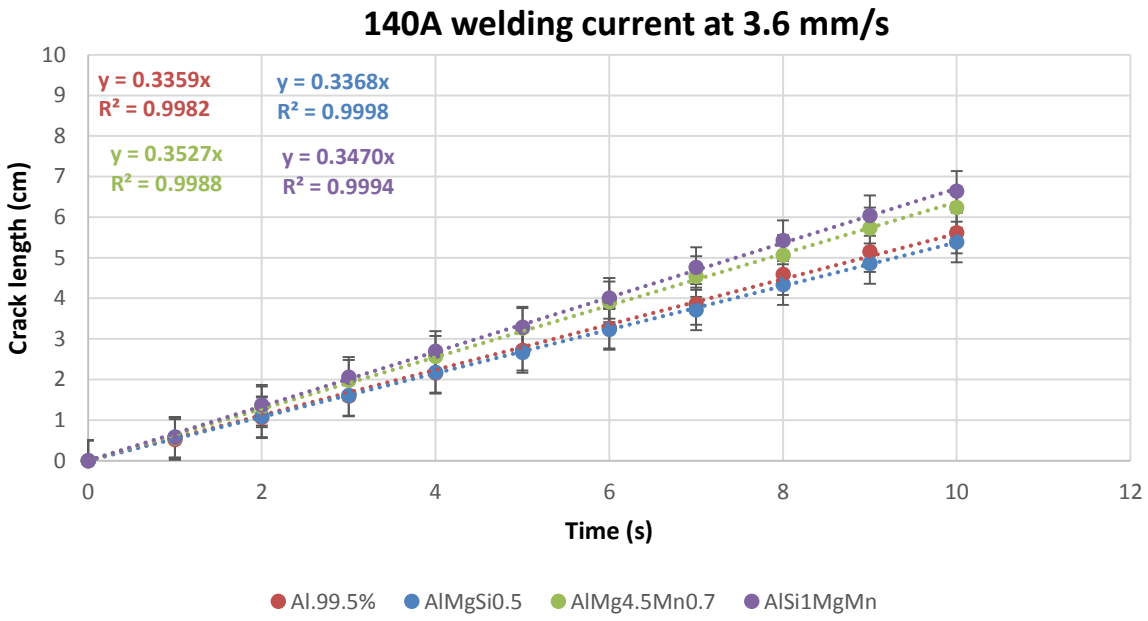

Figure 30: Crack length determination in relation to welding current 140A

Furthermore, the welding parameters influence on the heat input directly affects the solidification cracking susceptibility. The solidification rates of the weld correspond to the plasticity of the mushy zone. The strain intensity also influenced the thermal expansion and crack growth rate of the alloy creating an inconsistency in the crack lengths.

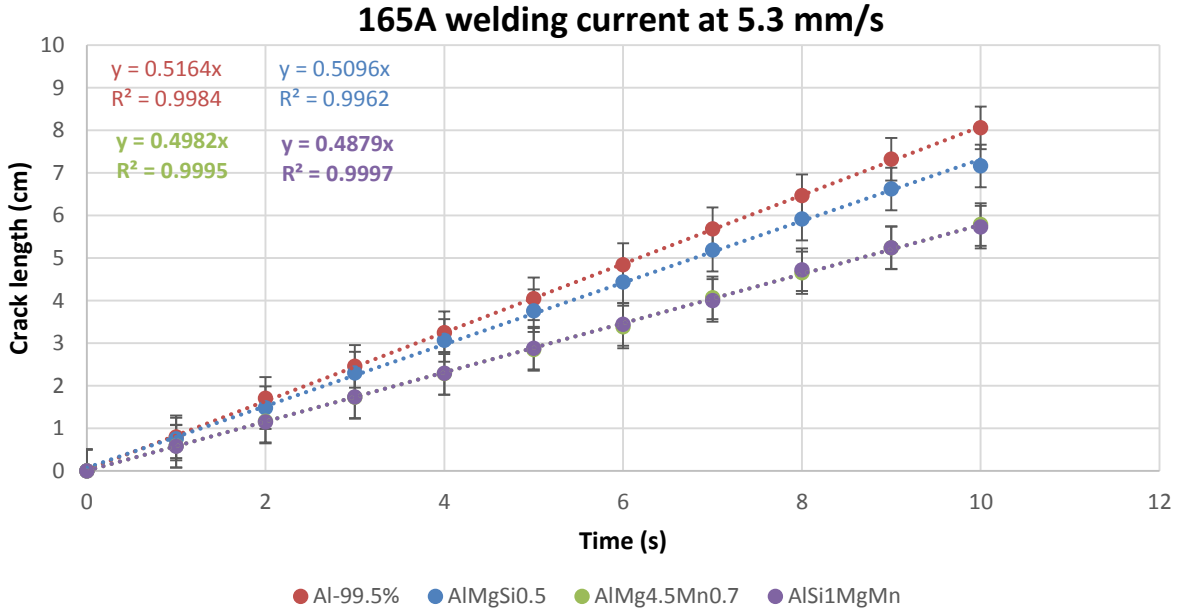

Figure 31: Crack length determination in relation to welding current 165A

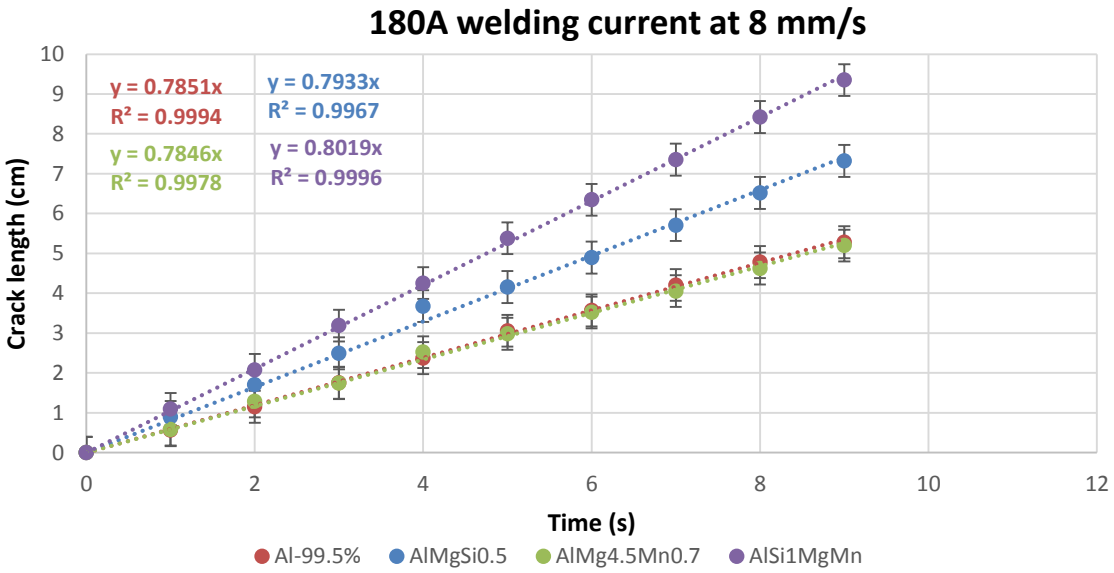

Figure 32: Crack length determination in relation to welding current 180A

7.3.2 Discussion

The measurements of weld crack lengths with the welding time were plotted (see Fig. 28, Fig. 29, Fig. 30, Fig. 31 and Fig. 32). All the experimental alloys exhibited crack initiation and crack propagation to the weld conditions. The result of two experimental data for currents 120A and 140A, the weld length and velocities for crack speed analysis was influenced by the welded design (i.e. bead-on-plate (BOP) and the Houldcroft test (HCT)). The bead-on-plate (BOP) recorded lower crack tip distances than the Houldcroft test (HCT) for all alloys in relation to the welding speeds (see Table 11).

Table 12: Measured crack growth rates extracted from slopes of Fig. 28 to Fig. 32 for Houldcroft tests

Welding speed (mm/s)	Crack growth rate for Al-99.5% (mm/s)	Crack growth rate for AlMgSi0.5 (mm/s)	Crack growth rate for AlMg4.5Mn0.7 (mm/s)	Crack growth rate for AlSi1MgMn (mm/s)
2.3	2.20	2.17	2.08	2.25
2.8	2.64	2.74	2.52	2.57
3.6	3.35	3.36	3.53	3.47
5.3	5.16	5.09	4.98	4.87
8	7.85	7.93	7.84	8.02

The summary of the measured crack growth rates for all welding speeds and material alloys is given in Table 12. The crack growths rate is maximal the welding speed, which is fulfilled in Table. 12. But depending on the alloy composition the shape of the mushy zone is changed, which results in a reduction of the crack growth rate of up to 10% from the welding speed depending on the alloy.

7.4 Co-planar laminography analysis

The laminographic reconstruction of the weld material was performed with the BAM reconstruction software “TomoPlan” (refer to Appendix C showing a parameter set used for reconstruction). The acquisition was realized by a co-planar translational motion. Sequences of radiographic images from different angles were combined in a reconstruction step to yield cross-sections of 3D data (see Fig. 13). After reconstruction, the reconstructed data were saved as ‘tiff’ stacks.

The crack lengths in the weld seam after welding from the translational laminographic projections are shown in Fig. 33. Some of the detailed characteristics from the laminographic projections such as edge cracks are marked in regions **A**, **B**, and **C,** as well as the measured crack lengths from the projected slices of a scanning angle range of ± 40°.

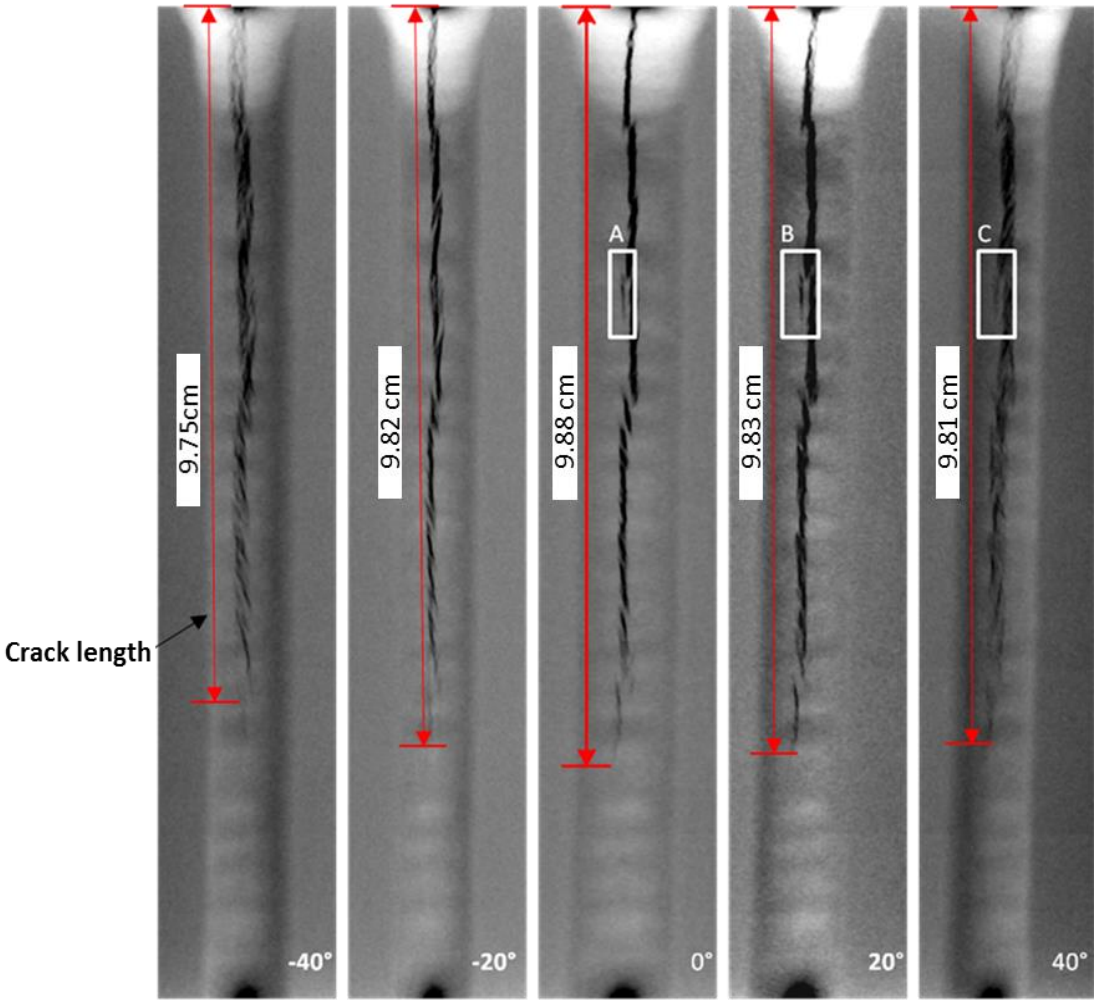

Figure 33: 2D Laminographic projections of AlMgSi0.5 alloy after bead-on-plate (BOP) welding of ± 40° scanning angle range at 8 mm/s welding speed

The measured edge crack lengths of the scanned weld were 1 cm, 1.2 cm and 1.05 cm for regions **A**, **B** and **C** respectively. This is the result of the different penetration angles when the beam direction differs from the crack direction in depth. The perpendicular penetration angle (0°) should give the maximum crack length because the solidification cracks are vertically in the welding seam see Fig. 43.

The crack lengths for both bead-on-plate (BOP) and the Houldcroft test (HCT) were compared to their welding speeds. The results showed the crack lengths at scan angle 0° measured the highest crack length in all welds (see Fig. 34 to Fig. 38). This confirms the above assumption. The bead-on-plate (BOP) test revealed higher crack lengths than the Houldcroft test. This is the result of the design of the base material; the bead-on-plate test has no saw cut slots at the edges (see subchapter 6.4.2).

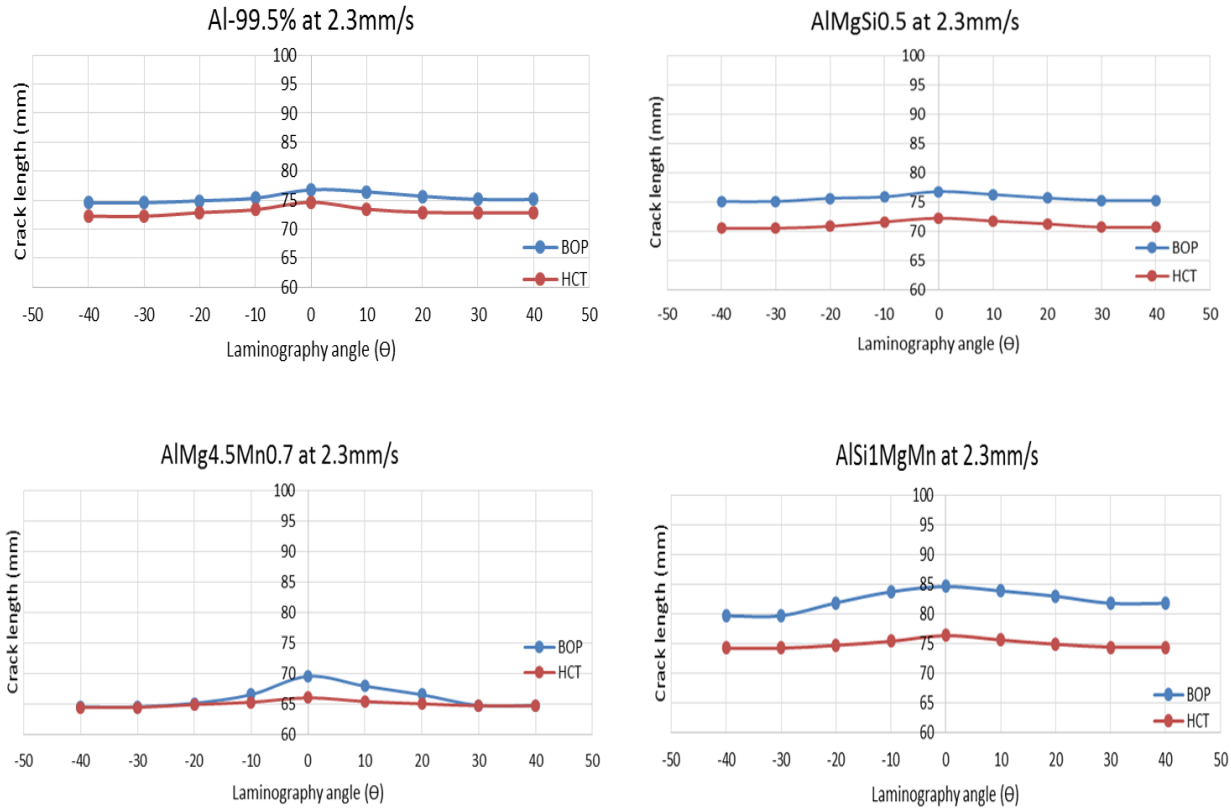

Figure 34: Crack length comparison in the projections for different alloys depending on the projection angle for 2.3 mm/s welding speed

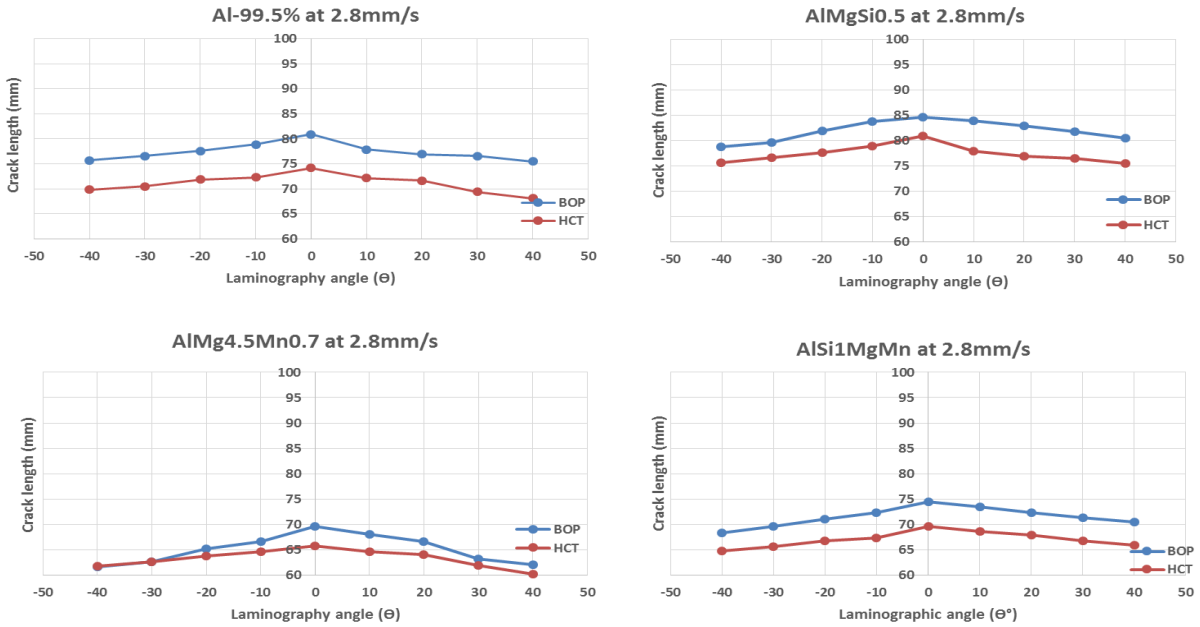

Figure 35: Crack length comparison in the projections for different alloys depending on the projection angle for 2.8 mm/s welding speed

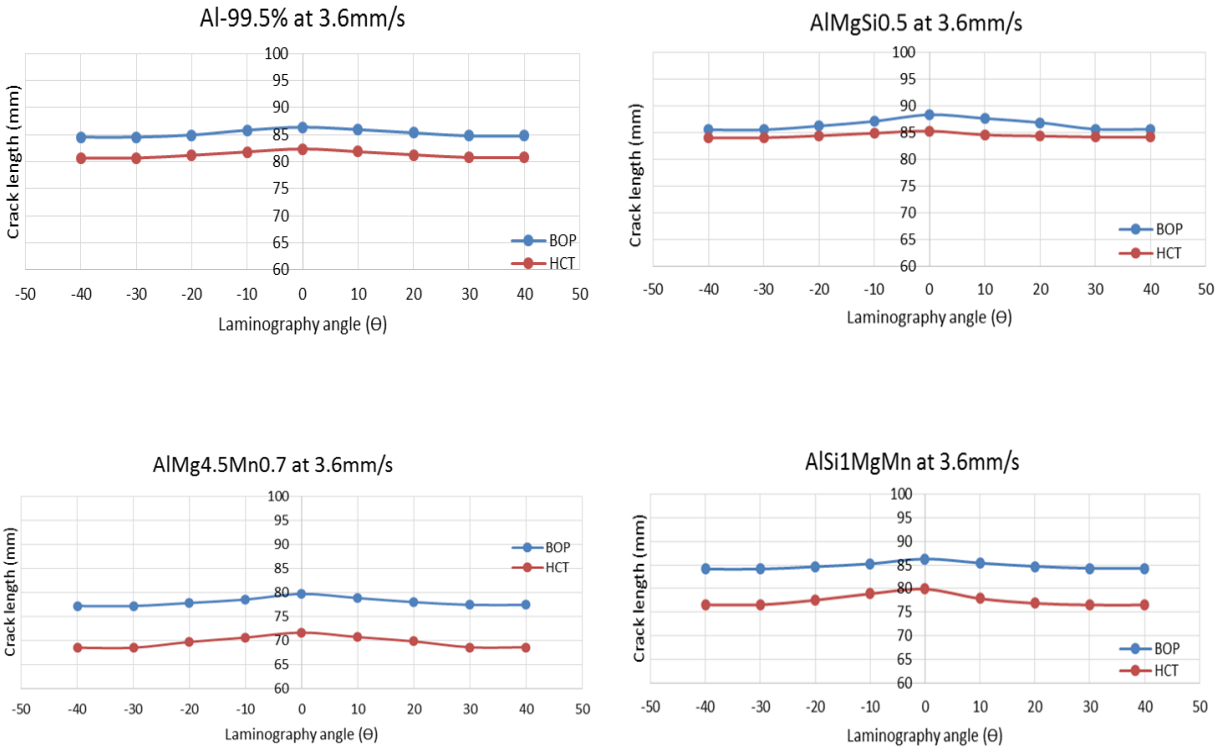

Figure 36: Crack length comparison in the projections for different alloys depending on the projection angle for 3.6 mm/s welding speed

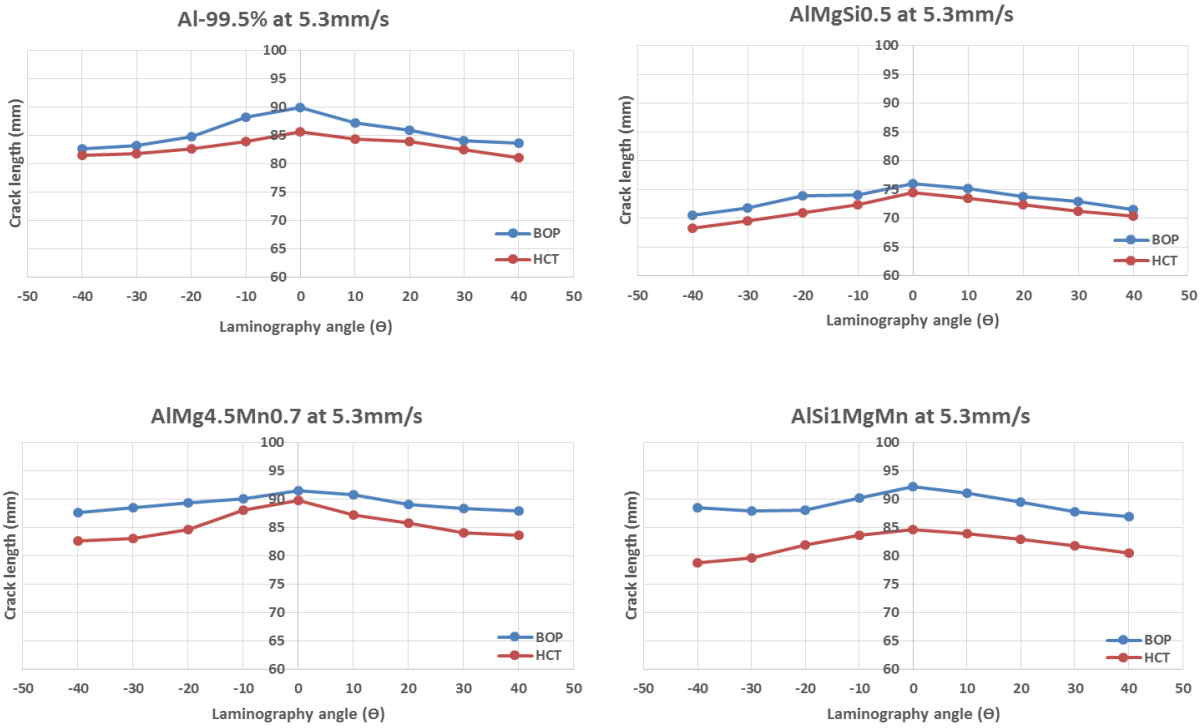

Figure 37: Crack length comparison in the projections for different alloys depending on the projection angle for 5.3 mm/s welding speed

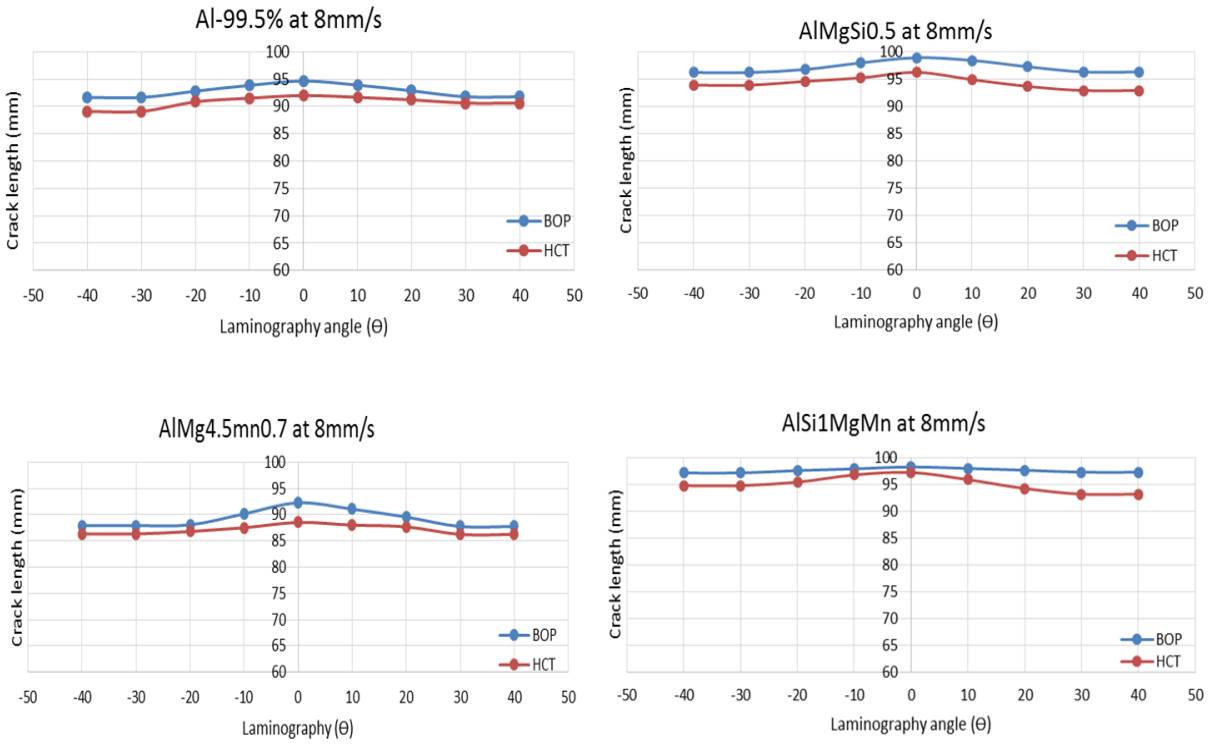

Figure 38: Crack length comparison in the projections for different alloys depending on the projection angle for 8 mm/s welding speed

Furthermore the comparison of the crack lengths between a single radiographic projection in Fig. 39 (**A**) and the translational laminographic reconstruction slice in the middle of the material Fig. 39 (**B**) were carried out. The measured crack lengths for both radiographic projection (**A**) and reconstructed translational laminographic slice (**B**) of a Houldcroft test (HCT) show the crack length of laminography reconstruction data appears to be longer than the measured crack length from the radiographic projection. This is a result of the laminographic reconstruction, where the crack information from the angle range of +/- 40° is accumulated. Therefore, the laminographic reconstruction shows the highest sensitivity for crack indications, which results in the longest crack length.

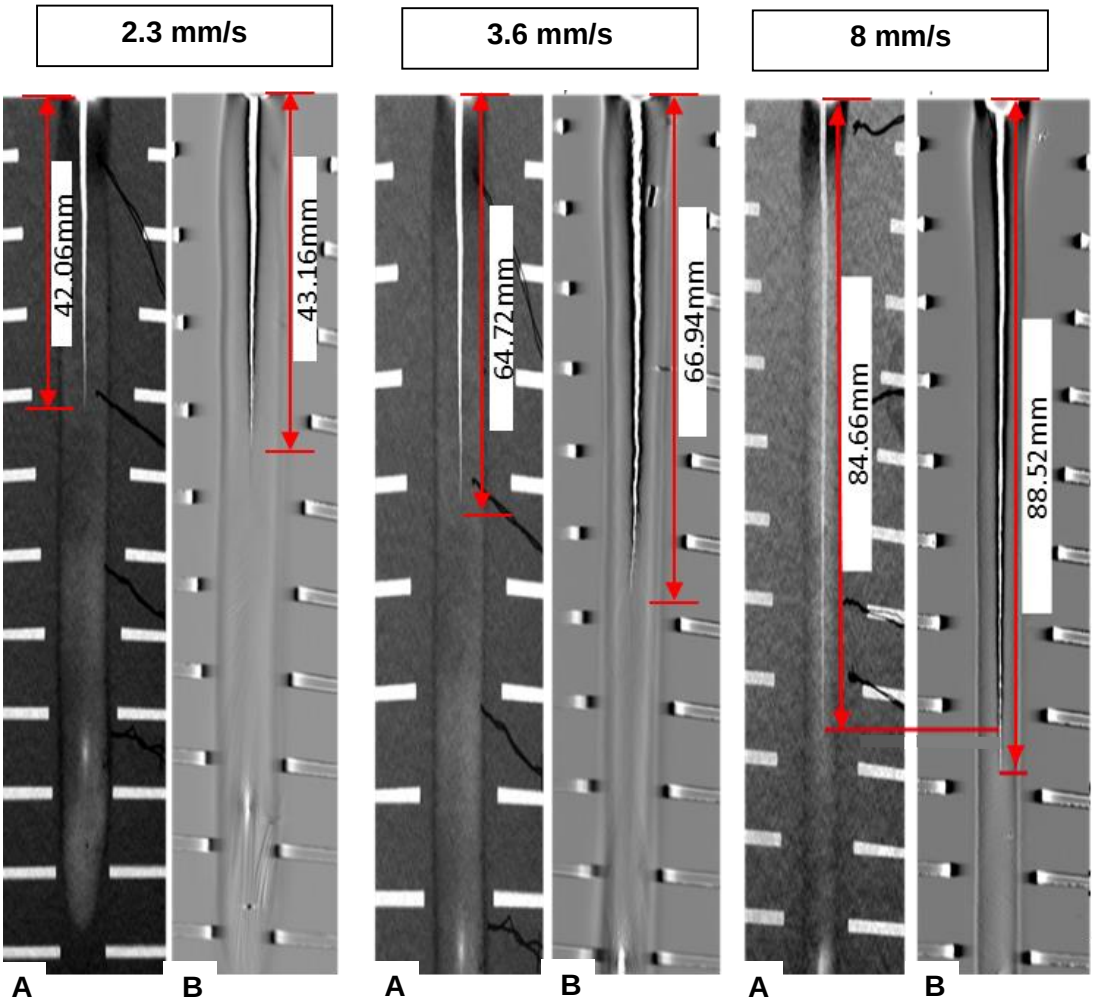

Figure 39: Comparison of raw 2D radiographic projections at 0° (A) and (B) reconstructed translational laminographic slices at the middle slice in 1.5 mm depth

The Houldcroft test (HCT) and bead-on-plate (BOP) welding techniques showed differences in the crack length of the welded material. The crack length for the bead-on-plate (BOP) test

was measured longer than the Houldcroft test (HCT) as shown in Fig. 34, Fig. 35, Fig. 36, Fig. 37 and Fig. 38 respectively. The crack length in the Houldcroft test (HCT) is shorter because the design of the saw cut slots in the base material reduces the weld material stiffness in the weld.

In Fig. 40, the crack length was compared from visual surface images, 2D projection radiographs at 0° and a laminographic reconstruction. The crack lengths from the laminographic reconstruction were measured the highest, the crack lengths of the 2D radiographs were shorter but still higher than the length at the surface. This confirms the earlier results from subchapters 7.1 and 7.4. of the crack length determinations.

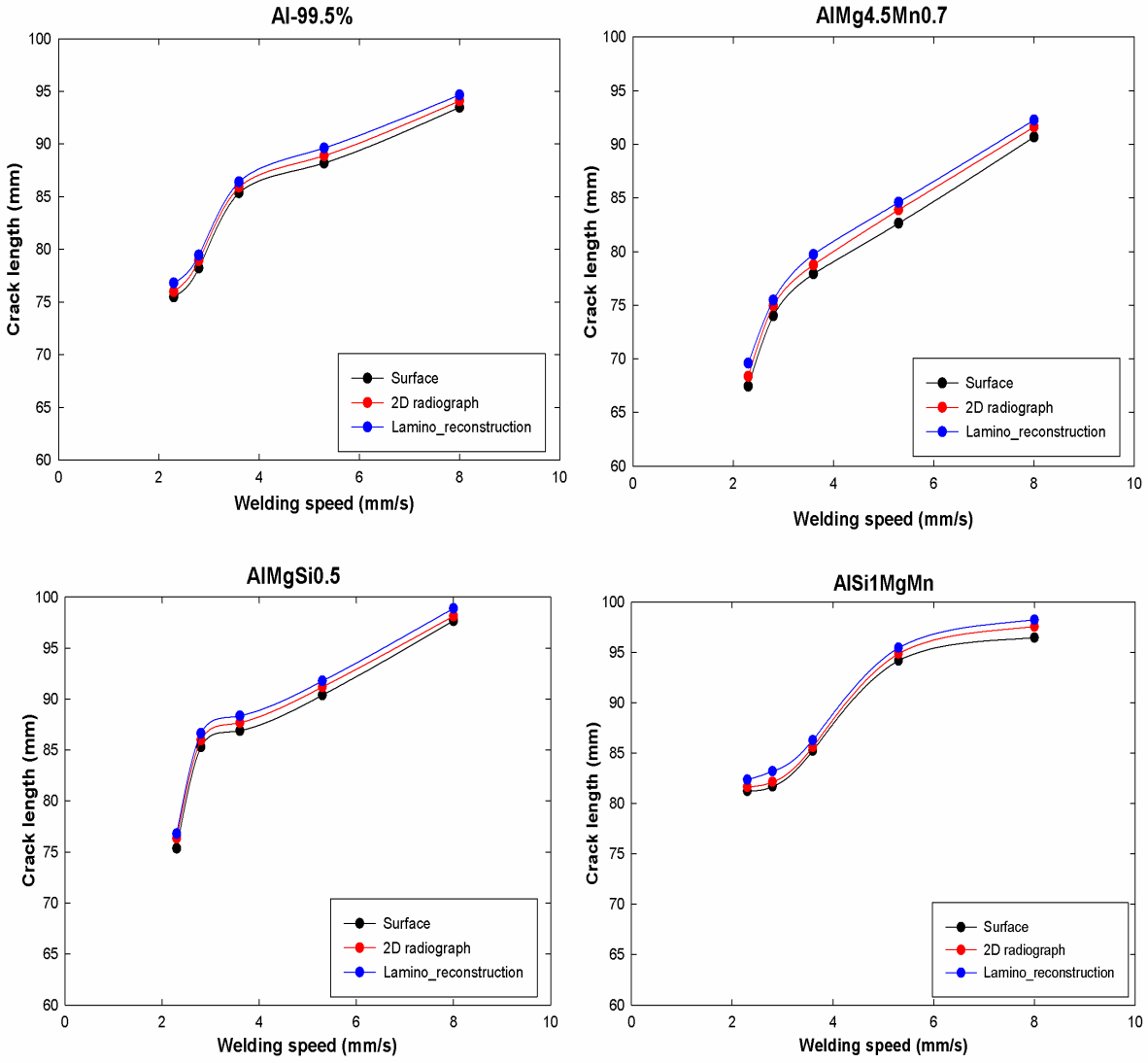

Figure 40: Crack length comparison with respect to welding speed for the three observatory methods

Further studies were also conducted for the determination of crack width as shown in Fig. 41 and Fig. 42. In Fig. 41, the measured crack width of 1 mm at position **A** had a crack depth of 1.8 mm. However, at position **B**, the measured crack width of 1.2 mm had a crack depth of 2.6 mm. These results were obtained using ImageJ image analysis of the reconstructed data. It cannot be shown in Fig. 41 and Fig. 42.

In Fig. 42, the measured crack width at positions **A** and **B** were 0.8 mm and 1.0 mm at crack depths of 2.3 mm and 2.8 mm respectively.

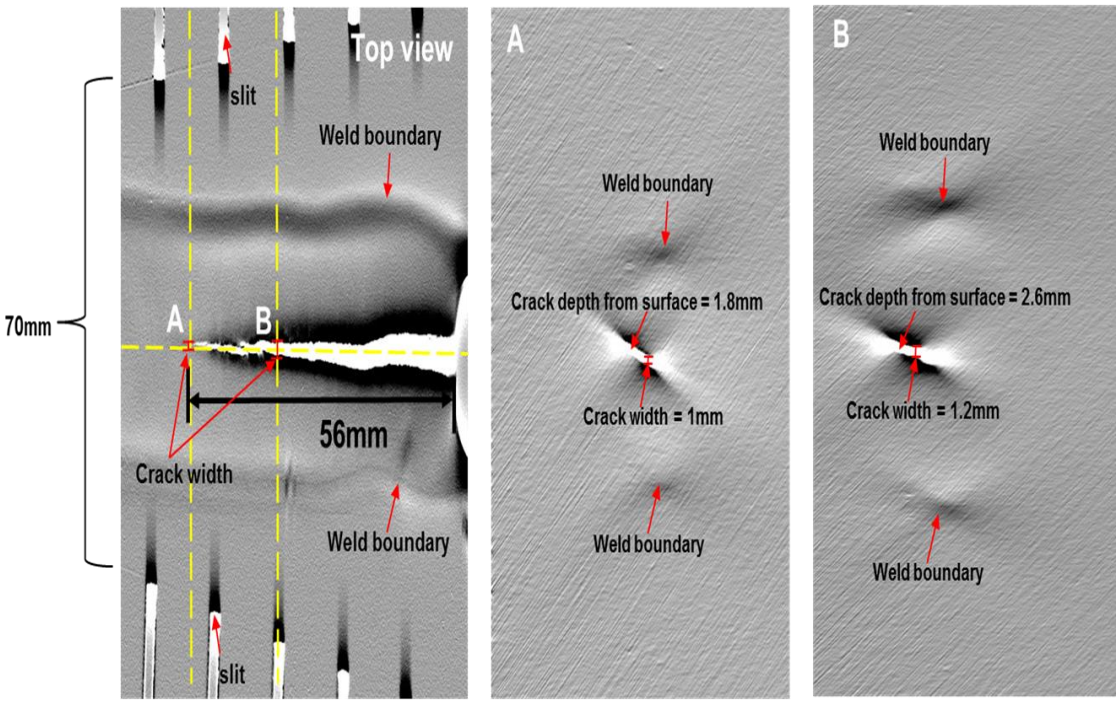

Figure 41: Laminograhic reconstruction of a Houldcroft test (HCT), Left: reconstructed centre slice and orthogonal cross-sections (A) and (B) Al-99.5% at 2.3 mm/s welding speed

These cross-sections of the laminographic reconstructions of the welding seam can be seen as an alternative to the destructive cross-sectioning by having a vertical slice of the reconstructed data. The advantage is to preserve the weld samples for further tests on the solidification cracking phenomenon.

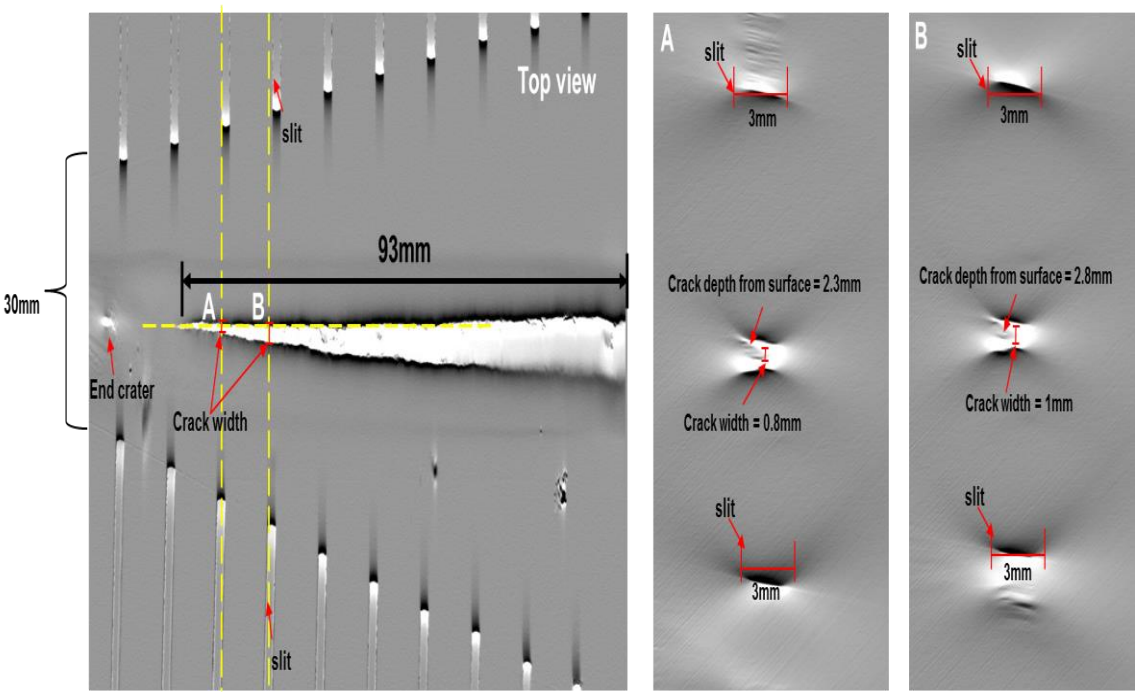

Figure 42: Laminograhic reconstruction of a Houldcroft test (HCT), Left: reconstructed centre slice and orthogonal cross-sections (A) and (B) AlMgSi0.5 at 8 mm/s welding speed

7.5 Comparison of reconstruction results of co-planar laminography and CT

The advantage of digital laminography is that the weld material can be reconstructed at different planes to determine the distribution of the crack lengths in depth. The weld defects derived from the laminographic reconstruction are comparable to computed tomography (CT) inspections. In computed tomography, the projected images of the material are acquired over an angular range of 360° on a rotating axis. In this chapter, the comparison of the image artefacts between laminography and computed tomography are discussed. In Fig. 43 (**A**) the front view of the rendered surface data set of the computed tomography reconstructed data of the weld seam is shown together with a cross-section derived from the reconstructed data at 2.5 mm depth (as seen in Fig. 43(**B**)).

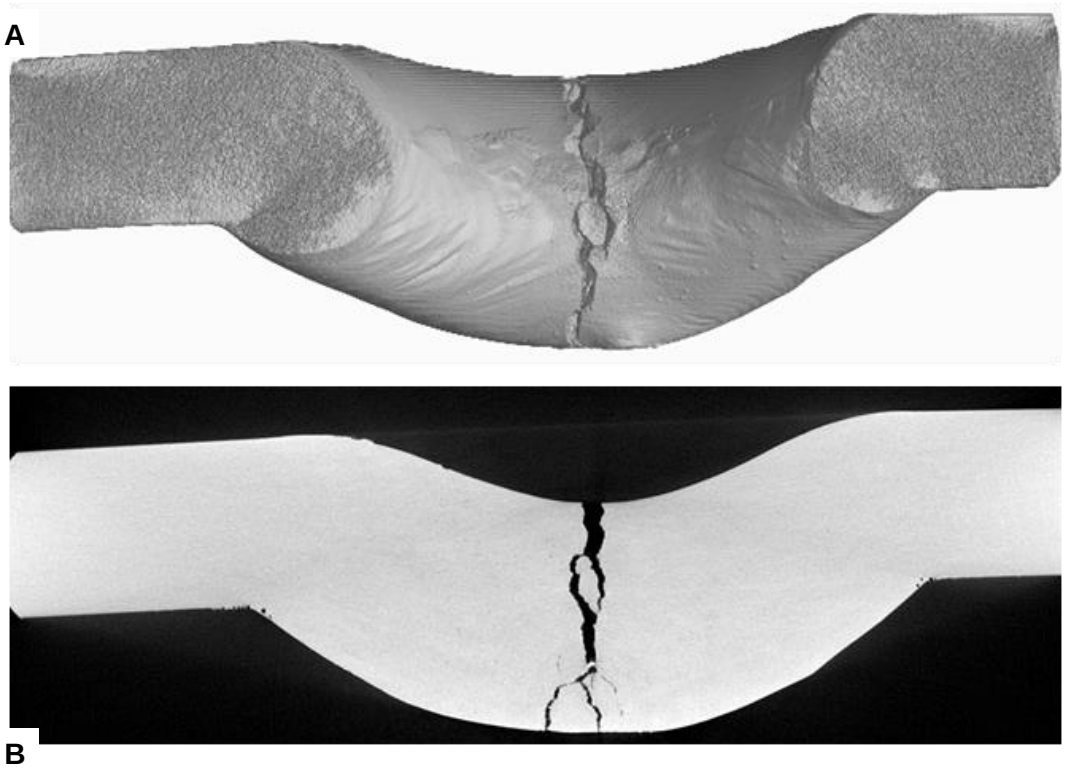

Figure 43: (A) CT surface rendering and (B) CT cross-section of AlMgSi0.5 alloy

The aim of laminography reconstruction and computed tomography is the reconstruction of depth information of the material, which is lost during the 2D projection in radiographic testing. In this way, weld imperfections such as gas pores, cracks and inclusions can be reconstructed in the real depth extension. However, the only setback of computed tomography is to have a

complete data set of the 360° projections. This cannot be achieved by using a welding plate. Therefore, typically small blocks of weld material are cut out for CT analysis, see Fig. 44 (**A**). This drawback of sectioning for computer tomography failed in the aim of non-destructive testing. The scanning of the entire material without intrusions is only achieved with laminography reconstruction (as seen Fig. 44 (**B**)). This is the main advantage of laminographic reconstruction; it does not require the sectioning of the weld material.

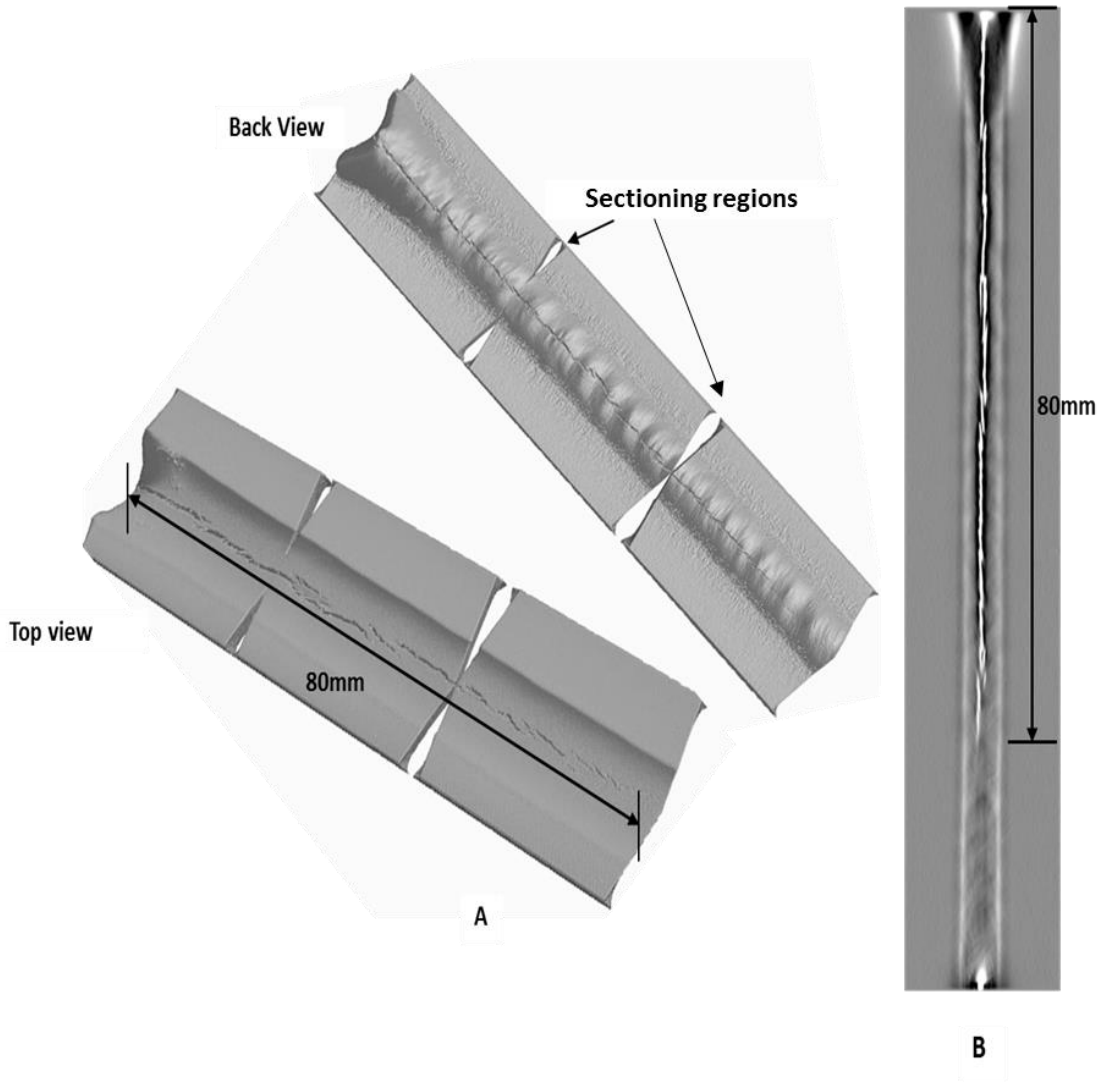

Figure 44: (A) CT surface rendering of the front and back and (B) Centre slice of laminographic reconstruction of the aluminium alloy before sectioning

The segmentation processes needed for 3D rendering to visualise flaw indications are identical for CT and laminographic data. Typical image analysis steps are pattern recognition, edge detection, thresholding and segmentation of the flaw volume. The segmentation techniques

usually result in the grouping of adjacent pixels in a region within the volume. For this research, the region-based segmentation was applied using VG Studio software.

7.5.1 Segmentation of laminographic data

The segmentation of the laminographic data enables the extraction of flaws from the laminographic reconstructions. The porosity and inclusion analysis module of the VG Studio software was used to assign parameters for the detection of pores or imperfections with low contrast. The extraction of microcavities such as gas pores that are visible in the laminographic reconstruction was necessary for further studies into weld imperfection as shown in Fig. 45.

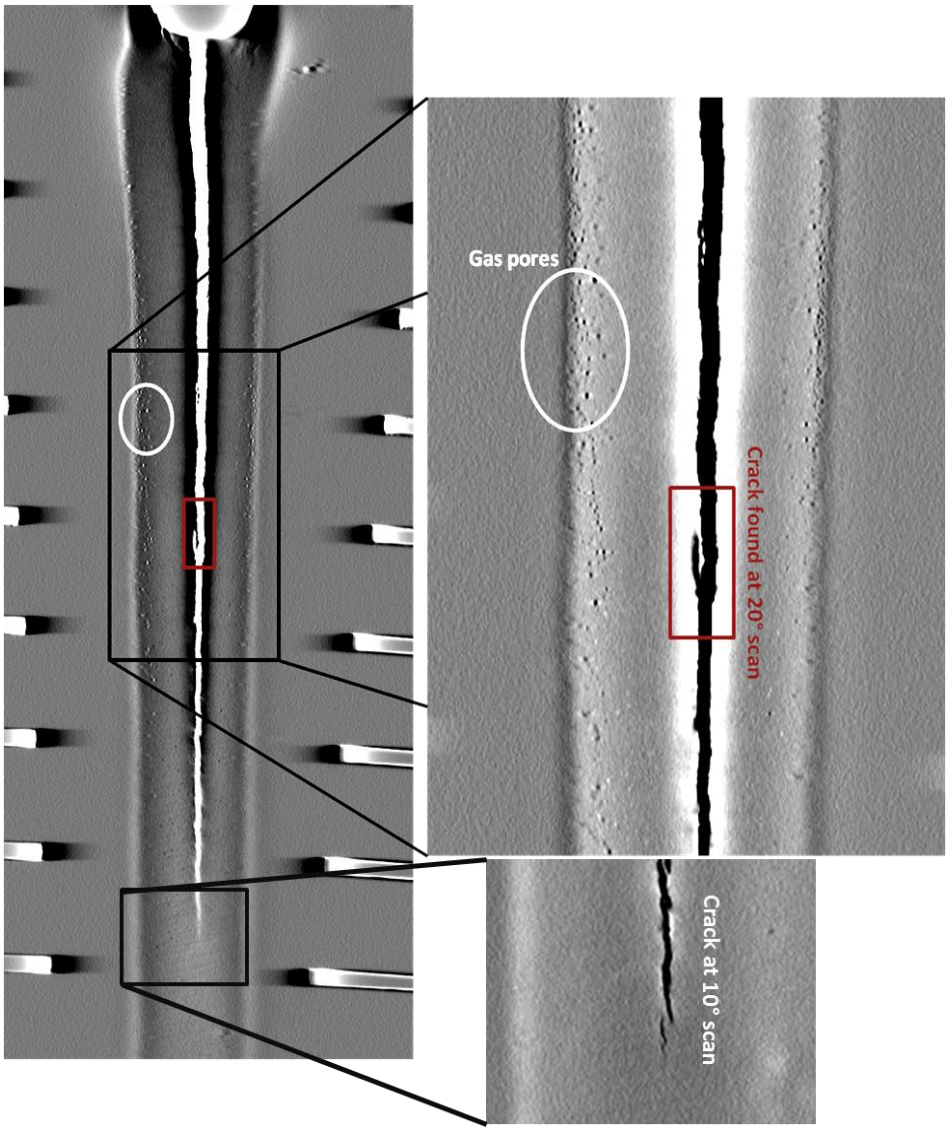

Figure 45: Weld imperfection observation with laminography

A region of interest of the volume was extracted for further processing, such as recognition and classification of the flaw indication. The shift average algorithm was an effective reconstruction method used to improve the image quality for defect detections.

7.5.2 Discussion

The non-destructive technique laminography provided a detailed reconstruction of weld defects.

The laminography technique was used as an alternative approach for real-time observation and determination of weld defects. Flaw parameters after reconstruction of the weld material (such as crack length, crack depth and inclusions) were determined. The advantage of laminography is the possibility for complete in situ 3D inspections of a welding plate. For CT only smaller sections can be inspected but with higher resolution (typically 1/1000th of the sectioning size of the material samples used for the preparation of the CT) than laminography (see Fig. 44 (A)).

7.6 Isosurface extraction from laminographic data

The isosurface extraction from volumetric data sets is an essential step for volume rendering. The volumetric data sets contain scalar grey values, density values being assigned to the vertices of a voxel grid to visualize and process the geometric surface information. These density values have to be segmented for visualisation.

Starting from a regular voxel grid the extracted isosurface can be very complex. In practice, it turns out that the geometrical complexity of isosurfaces is due to measurement inaccuracies and noise in the scalar data. Suitable imaging processing tools are used to reduce this complexity. The purpose of this section is to apply image segmentation to be able to extract isosurfaces from reconstructed laminographic data for further studies of crack imperfections.

7.6.1 Three-dimensional segmentation

The segmentation and visualization of the reconstructed data were carried out with VG Studio for Isosurface extraction. The software offers a large set of segmentation tools, ranging from manual to fully automatic segmentation. Other tools such as the region growing, thresholding, contour interpolation and extrapolation with various filters including smoothing, cleaning and connected component analysis also helped in the further analysis of the 3D data. These are commonly applied segmentation tools in reconstruction analysis for surface segmentation. The surface segmentation provided efficient segmentation of globally optimal surfaces representing the object boundaries in the volumetric data set.

7.6.2 Flaw segmentation

The flaw segmentation aims to compute a map called volume labelling, which classifies pixels in an image or voxels in a volume. The most general and robust method for image segmentation is the selection of the relevant structure, on each slice of the radiological data. This type of segmentation was used for low contrast images and hard-to-select shapes. The principle is to select pixels from the target structure and then aggregate successively neighbouring pixels to obtain a connected volumetric region. The flaw segmentation is based on voxel intensity values in a specific threshold interval. This threshold-based segmentation is a method of region growing by the generation of a binary image. This type of segmentation extracts inclusions and porosities in both CT and laminographic data. The results were

analysed with defect measurement algorithms to determine defect parameters such as length, width and depth. The defect determination involves grey level modifications such as equalisation, normalisation, brightness and contrast adjustment and filtering (to remove noise for improved contrast resolution). The grey level in the reconstruction is proportional to the local attenuation changes.

Sequential erosion and dilation operations were also applied to the images with increasing sizes of structural elements. The measured parameters were pore diameter and pore location. A separation procedure was used to separate the pores from each other. A volume of the region of interest in Fig. 46 (**A**) was rendered to obtain the 3D data set to visualize weld inclusions and cavities as shown in Fig. 46 (**B**).

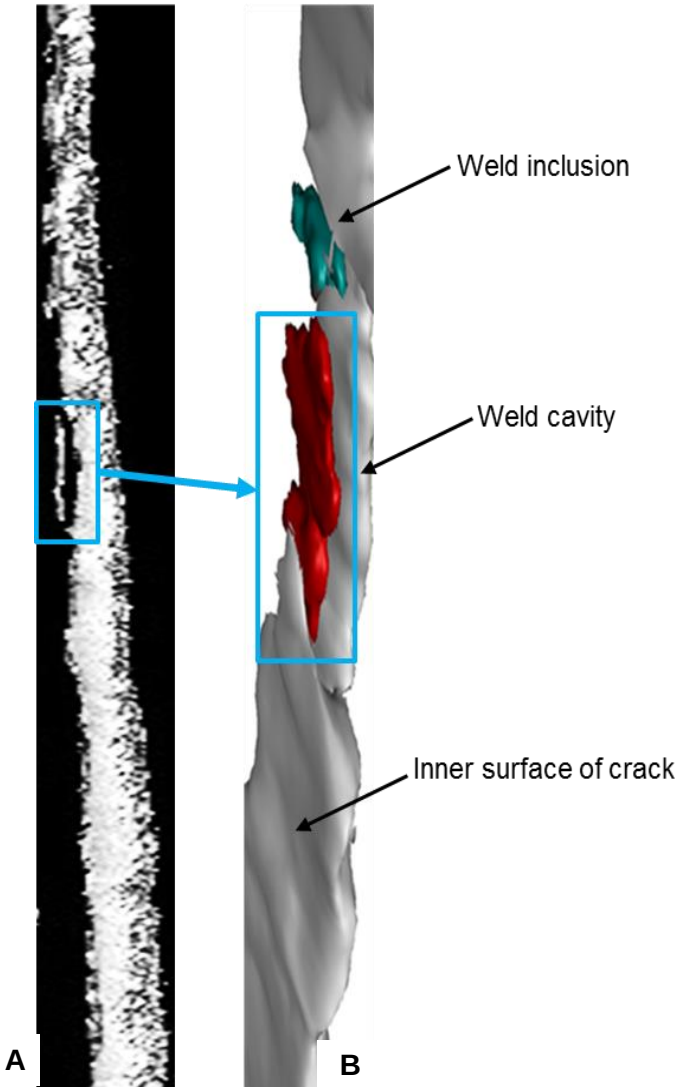

Figure 46: (A) Slice of laminography reconstruction and (B) Volumetric surface rendering of 3D laminography for flaw segmentation of the AlSi1MgMn sample

7.6.3 Porosity characterization

Weld pores are common defects in aluminium alloys that significantly affects the fatigue of the weld. The accurate determination of weld pore diameter and its depth is essential for weld fracture analysis. Porosity in welding occurs as a result of dissolved gas or gases entrapped in the material during welding because of insufficient time to escape before solidification.

As seen in Fig. 45, the porosity displayed is concentrated along the rim of the weld. This type of porosity was observed for all welding speeds.

The differences in porosity diameter depend on the amount of weld power associated with each set of welding parameters. The measured pore diameter and its correlation to the pore location for all the welded alloys were analysed.

The various welding parameters influence the segregation of the porosity formed. It was observed, that the pore location in depth depends linear on the power input for all alloys. The power input is directly proportional to the welding current and voltage. A change in current influences the welding power. The reason for this observation could not be clarified within this work.

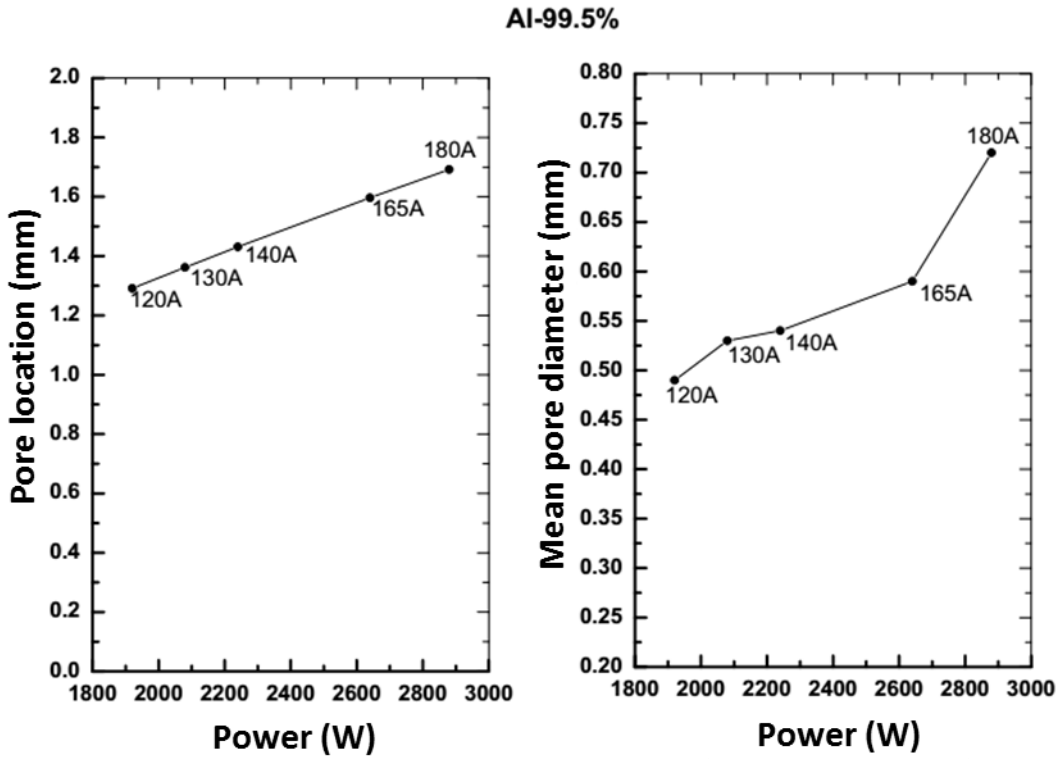

Figure 47: Pore location (measured as a distance from the lower surface of the weld material) and mean pore diameter for Al-99.5% alloy depending on the power input

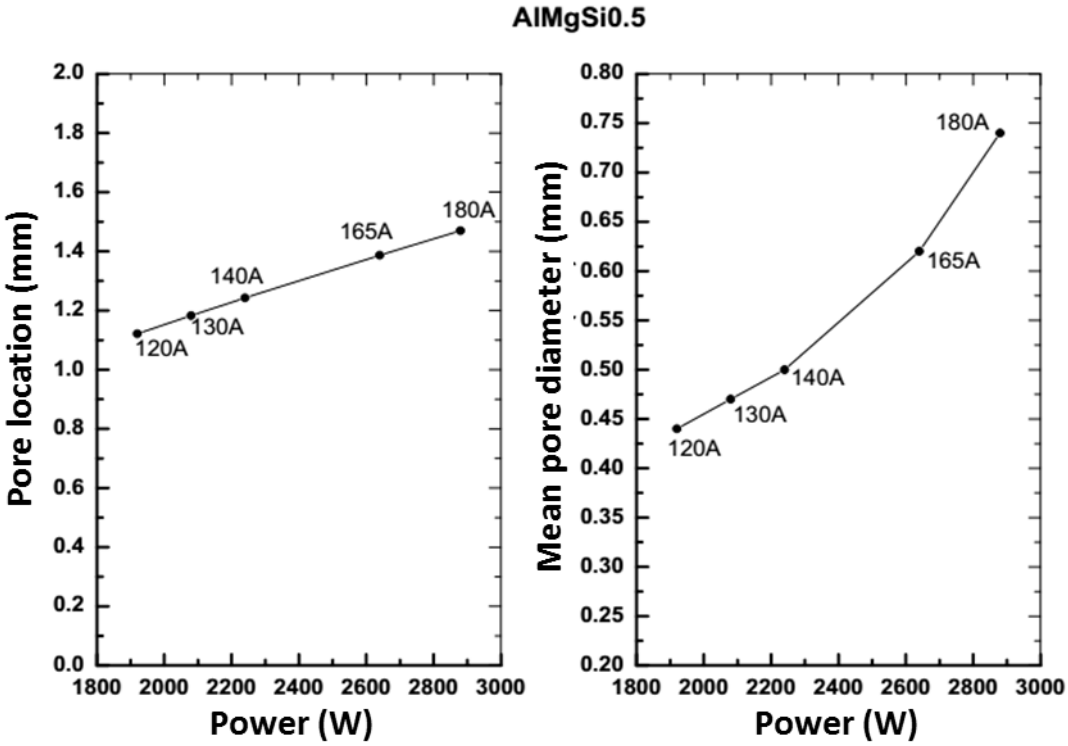

Figure 48: Pore location (measured as a distance from the lower surface of the weld material) and mean pore diameter for AlMgSi0.5 alloy depending on the power input

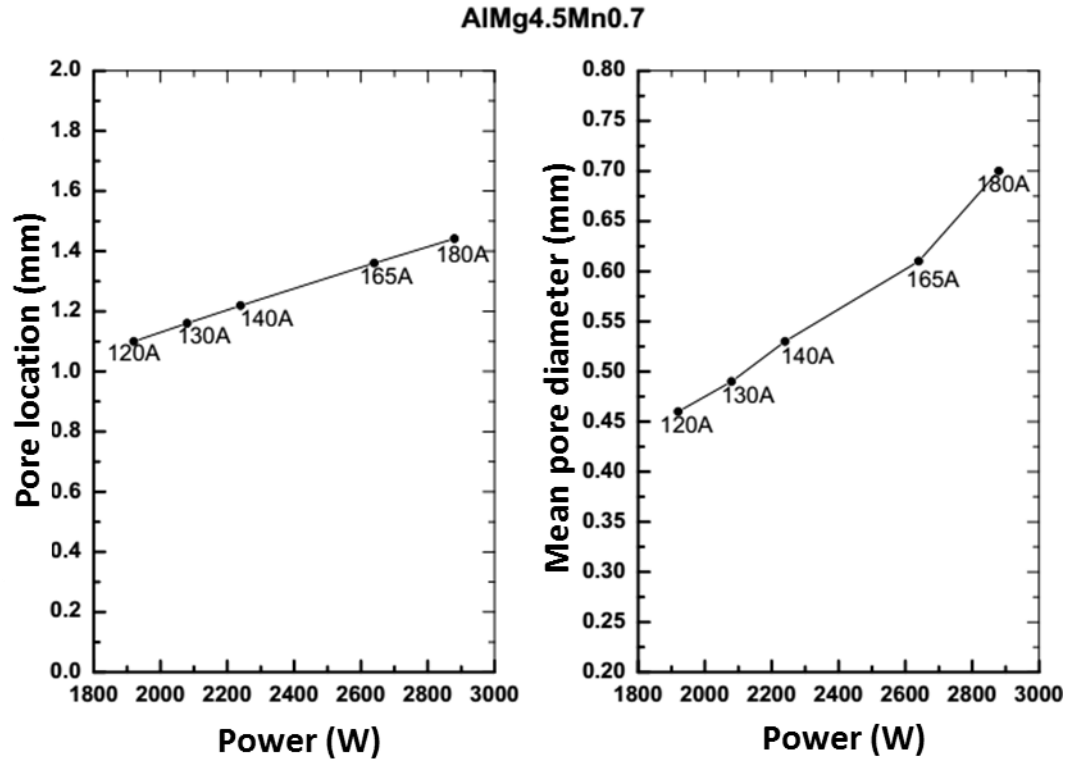

Figure 49: Pore location (measured as a distance from the lower surface of the weld material) and mean pore diameter for AlMg4.5Mn0.7 alloy depending on the power input

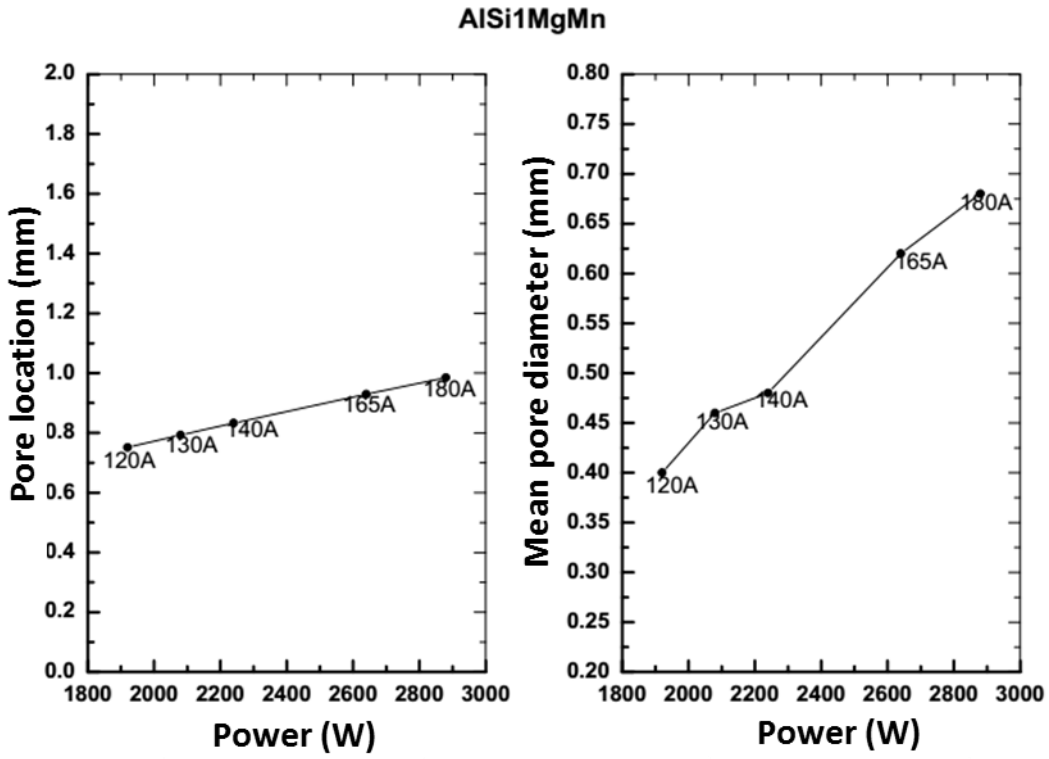

Figure 50: Pore location (measured as a distance from the lower surface of the weld material) and mean pore diameter for AlSi1MgMn alloy depending on the power input

As shown in Fig. 47, the pore location for Al-99.5% alloy was observed to be highest for all welding currents. This is caused by the lowest solidification rates of all weld alloys (see Fig. 25). All alloys showed a close relation between pore location and the pore diameter as shown in Fig. 47, Fig. 48, Fig. 49 and Fig. 50 respectively. The porosities were observed in all five experimented aluminium alloys but only alloys with cracks were analysed.

7.6.4 Discussion

Laminography is particularly suited to precisely determine the position of defects within the welded material volume. The main objective is the depth determination of defects such as pores, cracks or inclusions within the volume. The flaws in an aluminium weld are influenced by the alloys composition, the welded design and power input (i.e welding parameters). It was observed that the welding current plays a major role in the pore-forming tendencies within the alloy. The weld pore location and the mean pore diameter as a function of power input were determined from the reconstructed data. At an increasing power input, increasing pore diameters were observed at a linear increasing depth of pores within the weld volume.

In Fig. 47, the diameters of the mean pores of 0.49 mm and 0.72 mm were obtained for welding currents 120 A and 180 A respectively. This shows for increasing power input and increasing pore diameter and pore depth. This is a result of the solidification rate of the weld pool depending on the weld heat input. For all alloys, the pore location shows a close relation in the pore location and the diameter of the measured pores as shown In Fig. 47- Fig. 50. The effect of the heat input on the thermal distribution within the welded material influenced the size and location of porosity. However, Fig. 50 measured mean pore diameters of 0.40 mm and 0.69 mm for welding currents 120 A and 180 A at pore locations 0.7 mm and 0.9 mm respectively. The reason for the smaller pore diameters for AlSi1MgMn can be attributed to the alloy composition of 0.70w% of Si and 0.25w% of Cr (refer to Table 7).

8 General conclusions and future work

The implementation of the time-resolved digital X-ray radiography technique for the observation of crack growth during welding for different aluminium alloys was successfully achieved.

The experimental setup was proven to measure crack initialization and propagation. The varied weld parameters are listed in Table 8, which generates variations in crack length and temperature distribution during welding.

The radiography with an exposure time of 40milliseconds is suitable for crack growth observation of aluminium alloy of 3 mm thickness. However, the image quality for 1 frame at an exposure time of 40 milliseconds is limited by the signal to noise ratio in this short exposure. The achieved basic spatial image resolution is 100 µm (D10 of Duplex IQI), which corresponds to testing class A of ISO 17636-2 “Radiographic testing of welds” as shown in Fig. 12.

A major outcome is a discovery, that high pass filtered X-ray projection has to be used for correct measurements of the crack tip distance to the rim of the mushy zone. Visual surface images or raw X-ray projections do not allow precise measurements.

The maximum crack lengths were observed in the X-ray projections of 0° because the observed crack orientations are perpendicular to the weld surface.

A laminographic reconstruction algorithm (BAM TomoPlan software) was used on the post-weld 2D projection data for depth reconstruction and enhancement of the image quality to detect welding flaws that were not visible in the on-line radiographic data. Detailed information was generated from three-dimensional (3D) visualization of the assembly by cross-sectioning of the reconstructed volume. The experimental results have shown that this technique is sensitive in detecting cracks in full length or porosity down to the detector pixel size of 75 µm, as well as measuring pore locations and depths in the welded material.

One benefit of the laminographic technique is a lower number of projections for reconstruction in comparison to computed tomography. Typically, 400 projections were used for laminography and 2500 projections for CT.

The laminographic images of the weld show that cracks propagate not only along the weld direction but also through the thickness. After reconstruction of the scanning data cracks, initiation and growth coalescence with the elongated pores can be visualized**.**

CT is particularly suited to precisely determine the extent and position of defects within the material volume. A non-interactive segmentation algorithm allows for automated detection and evaluation of pores within the volume.

Different defects parameters such as pore diameter and pore locations can be quantified by CT and laminography. The segmentation procedure facilitates a simplified representation of the crack structure and the 3D distribution of gas pores within the weld.

Based on the results of this research, the following topics can be a possible framework for future works to expand the understanding of cracking behaviour and its observation:
The observation of crack initiation and propagation of hot cracks in the mushy zone was achieved here. Crack lengths were compared from a high-speed camera, from real-time 2D radiographs and laminographic reconstruction. However, the limited angle of the laminographic reconstructions limits the depth resolution of the weld. In addition, structures within the weld that are located on the edges of the weld were affected due to reconstruction artefacts.
However, increasing the number of projections and a larger angular range of probably 120° will enhance the resolution of the reconstruction.
The following topics will advance the studies into hot cracking observation.

1. Achieving a testing class B according to ISO 17636-2 will help for more detailed information of the weld pool and its respective crack formation.
2. Having a geometry that enables online reconstruction of the acquired 2D radiographs in real-time during welding.
3. An investigation of the fusion region for a better understanding of the weld pool mechanics and other materials such as steel.
4. Application of swing laminography perpendicular to the welding direction will allow for real-time 3D reconstruction and not only post welding as shown in this work.

9 Bibliography

1. Kannengiesser, T. and T. Boellinghaus, *Hot cracking tests-an overview of present technologies and applications.* Welding in the World, 2014. **58**(3): p. 397-421.
2. Kannengiesser, T., et al., Assessment of hot cracking behaviour in welds. International Journal of Materials Research, 2011. 102(8): p. 1001-1006.
3. Rindler, W., E. Kozeschnik, and B. Buchmayr, Computer simulation of the brittle-temperature-range (BTR) for hot cracking in steels. Steel Research, 2000. 71(11): p. 460-465.
4. Drezet, J.M. and D. Allehaux, Application of the Rappaz-Drezet-Gremaud Hot Tearing Criterion to Welding of Aluminium Alloys. Hot Cracking Phenomena in Welds Ii, ed. T. Bollinghaus, et al. 2008. 19-37.
5. Ewen, D., *Shrinkage of the antimony-lead alloys and the aluminium-zinc alloys during and after solidification.* Journal of the Institute of Metals, 1910. **4**: p. 130-162.
6. Kannengiesser, T., et al., *The influence of local weld deformation on hot cracking susceptibility*, in *Mathematical Modelling of Weld Phenomena 6*, H. Cerjak, Editor. 2002. p. 803-818.
7. Garland, J.G. and G.J. Davies, A MODIFIED HOULDCROFT HOT-CRACKING TEST WITH IMPROVED REPRODUCIBILITY. Metal Construction and British Welding Journal, 1969. 1(12): p. 565-&.
8. Wien, M., The history of the discovery of X-ray radiations. Physikalische Zeitschrift, 1935. 36: p. 536-536.
9. Watson, E.C., THE DISCOVERY OF X-RAYS. American Journal of Physics, 1945. 13(5): p. 281-291.
10. Stark, J., *The history of the discovery of the X-rays.* Physikalische Zeitschrift, 1935. **36**: p. 280-283.
11. Wien, M., The history of the discovery of the X-ray beams. Physikalische Zeitschrift, 1935. 36: p. 536-537.
12. Gerlach, W., X-RAYS IN HISTORY OF SCIENCE. Strahlentherapie, 1970. 140(3): p. 245-&.
13. Zscherpel, U., U. Ewert, and M. Jechow, *NEW REQUIREMENTS FOR DIGITAL RADIOGRAPHIC TESTING OF WELDS ACCORDING TO ISO STANDARDS*, in *Review of Progress in Quantitative Nondestructive Evaluation, Vols 32a and 32b*, D.O. Thompson and D.E. Chimenti, Editors. 2013. p. 1112-1119.

14. Blakeley, B. and K. Spartiotis, *Digital radiography for the inspection of small defects.* Insight, 2006. **48**(2): p. 109-112.
15. Garcia, G., et al., *QUANTITATIVE NONDESTRUCTIVE EVALUATION OF RAILROAD TANK CARS*. Proceedings of the ASME/ASCE/Ieee Joint Rail Conference. 2012. 201-208.
16. Drezet, J.M. and M. Rappaz, *Prediction of hot tears in DC-cast aluminium billets*, in *Light Metals 2001*, J.L. Anjier, Editor. 2001. p. 887-893.
17. Ewert, U., *ADVANCES IN DIGITAL INDUSTRIAL RADIOLOGY - NEW APPLICATION AREAS BEYOND FILM RADIOGRAPHY*, in *Review of Progress in Quantitative Nondestructive Evaluation, Vols 32a and 32b*, D.O. Thompson and D.E. Chimenti, Editors. 2013. p. 18-32.
18. Gros, X.E., *REAL-TIME RADIOGRAPHY OF UNDERWATER PIPELINES.* British Journal of Non-Destructive Testing, 1993. **35**(9): p. 492-495.
19. Jantsch, M., *THE HISTORY OF X-RAY DIAGNOSTIC IN UROLOGY.* Wiener Klinische Wochenschrift, 1984. **96**(17): p. 637-642.
20. Rossi, R.P., et al., *X-RAY-EQUIPMENT PERFORMANCE - A 35 YEAR CASE-HISTORY.* American Journal of Roentgenology, 1981. **136**(6): p. 1199-1205.
21. Bhandal, G.S. and K. Singh, *STUDY OF PHOTON ATTENUATION COEFFICIENTS OF SOME MULTIELEMENT MATERIALS.* Nuclear Science and Engineering, 1994. **116**(3): p. 218-222.
22. Ogilvie, R.E., *A NEW MASS ABSORPTION-COEFFICIENT EQUATION.* Institute of Physics Conference Series, 1993(130): p. 75-78.
23. Wang, D.C., et al., *X-RAY ATTENUATION COEFFICIENTS AND PHOTOELECTRIC CROSS-SECTIONS OF CU AND FE IN THE RANGE 3 KEV TO 29 KEV.* Nuclear Instruments & Methods in Physics Research Section B-Beam Interactions with Materials and Atoms, 1992. **71**(3): p. 241-248.
24. Sharma, A.K., *Surface engineering for thermal control of spacecraft.* Surface Engineering, 2005. **21**(3): p. 249-253.
25. Bellet, M., G.H. Qiu, and J.M. Carpreau, *Comparison of two hot tearing criteria in numerical modelling of arc welding of stainless steel AISI 321.* Journal of Materials Processing Technology, 2016. **230**: p. 143-152.
26. Schempp, P., et al., *Influence of grain size on mechanical properties of aluminium GTA weld metal.* Welding in the World, 2013. **57**(3): p. 293-304.
27. Cross, C.E., *On the origin of weld solidification cracking*. Hot Cracking Phenomena in Welds, ed. T. Bollinghaus and H. Herold. 2005. 3-18.

28. Schempp, P. and M. Rethmeier, *Understanding grain refinement in aluminium welding Henry Granjon Prize 2015 winner category B: materials behaviour and weldability.* Welding in the World, 2015. **59**(6): p. 767-784.
29. Matsuda, S., *ON THE SUPERLATTICE FORMATION IN TERNARY ALLOYS.* Journal of the Physical Society of Japan, 1953. **8**(1): p. 20-25.
30. Matsuda, T., *On the quenching and tempering of brass, bronze, and "aluminium-bronze".* Journal of the Institute of Metals, 1928. **39**: p. 67-108.
31. Kromm, A., et al., *Residual Stresses in Multilayer Welds with Different Martensitic Transformation Temperatures Analyzed by High-Energy Synchrotron Diffraction*, in *Residual Stresses Viii*, P. Scardi and C.L.A. Ricardo, Editors. 2011. p. 37-42.
32. Gollnow, C. and T. Kannengiesser, *Hot cracking analysis using in-situ digital image correlation technique.* Welding in the World, 2013. **57**(3): p. 277-284.
33. Schroepfer, D., T. Kannengiesser, and A. Kromm, *Influence of Heat Control on Welding Stresses in Multilayer-component Welds of High-strength Steel S960QL*, in *Residual Stresses Ix*, M. Francois, et al., Editors. 2014. p. 475-480.
34. Mousavi, M.G., et al., *Grain refinement due to grain detachment in electromagnetically stirred AA7020 welds.* Science and Technology of Welding and Joining, 2003. **8**(4): p. 309-312.
35. Yakhushin, B., *Morphology of hot cracks in single-phase weld metal*. Hot Cracking Phenomena in Welds, ed. T. Bollinghaus and H. Herold. 2005. 104-115.
36. Wolf, M. and T. Kannengiesser, *Modern test methods for assessing the hot cracking resistance during welding of high-alloyed steels and nickel base alloys.* Soldagem & Inspecao, 2007. **12**(1): p. 73-77.
37. Carnevali, F., *Autogenous welding by means of oxygen and acetylene of copper and its principal alloys, and of aluminium.* Journal of the Institute of Metals, 1912. **8**: p. 282-311.
38. Chouriguine, *The alloys of platinum with aluminium.* Comptes Rendus Hebdomadaires Des Seances De L Academie Des Sciences, 1912. **155**: p. 156-158.
39. Boellinghaus, T. and T. Kannengiesser, *An overview on cold cracking tests - Part 2: Self-restraint tests.* Soldagem & Inspecao, 2007. **12**(3): p. 244-260.
40. Chou, C.C., K.C. Tsai, and W.C. Yang, *Self-centering steel connections with steel bars and a discontinuous composite slab.* Earthquake Engineering & Structural Dynamics, 2009. **38**(4): p. 403-422.

41. Balasubramanian, K. and V. Balusamy, *Effect of vibratory treatment on hot cracking resistance in AA6061 alloy*, in *Recent Trends in Advanced Materials*, D.R. Babu, Editor. 2012. p. 516-520.
42. Schwenk, C., T. Kannengiesser, and M. Rethmeier, *Restraint Conditions and Welding Residual Stresses in Self-Restrained Cold Cracking Tests*. Trends in Welding Research, ed. S.A. David, et al. 2009. 766-773.
43. Wolf, M., H. Schobbert, and T. Bollinghaus, *Influence of the weld pool geometry on solidification crack formation*. Hot Cracking Phenomena in Welds, ed. T. Bollinghaus and H. Herold. 2005. 245-268.
44. Anderson, W.C. and G. Lean, *"The properties of the aluminium-tin alloys.".* Proceedings of the Royal Society of London, 1903. **72**(482): p. 277-U5.
45. Coniglio, N. and C.E. Cross, *Weld Parameter and Minor Element Effects on Solidification Crack Initiation in Aluminium*. Hot Cracking Phenomena in Welds Ii, ed. T. Bollinghaus, et al. 2008. 277-310.
46. Otarawanna, S. and A.K. Dahle, *Casting of aluminium alloys.* Fundamentals of Aluminium Metallurgy: Production, Processing and Applications, 2011: p. 141-154.
47. Edwards, C.A. and J.H. Andrew, *The constitution and properties of the aluminium-copper-tin alloys.* Journal of the Institute of Metals, 1909. **2**: p. 29-57.
48. *Aluminium and its alloys.* Nature, 1902. **66**: p. 655-657.
49. Pecheux, H., *A property of tin-aluminium, bismuth-aluminium, magnesium-aluminium alloys.* Comptes Rendus Hebdomadaires Des Seances De L Academie Des Sciences, 1905. **140**: p. 1535-1536.
50. Seligman, R. and F.J. Willott, *The analysis of aluminium and its alloys.* Journal of the Institute of Metals, 1910. **3**: p. 138-150.
51. Boellinghaus, T. and T. Kannengiesser, *An overview on cold cracking tests - Part 1: Externally loaded tests (Reprinted from International Institute of Wilding (IIW/IIS)).* Soldagem & Inspecao, 2007. **12**(2): p. 160-166.
52. Eder, A., S. Jaber, and N. Jank, *Using Simulation for Investigations of Hot Cracking Phenomena in Resistance Spot Welding of 6xxx Aluminium Alloys (AA6016 and AA6181)*. Hot Cracking Phenomena in Welds Ii, ed. T. Bollinghaus, et al. 2008. 311-325.
53. Kim, K.Y., J. Park, and R. Sohmshetty, *Prediction measurement with mean acceptable error for proper inconsistency in noisy weldability prediction data.* Robotics and Computer-Integrated Manufacturing, 2017. **43**: p. 18-29.

54. Pu, J., S.F. Yu, and Y.Y. Li, *Effects of Zr-Ti on the microstructure and properties of flux aided backing submerged arc weld metals.* Journal of Alloys and Compounds, 2017. **692**: p. 351-358.
55. DuPont, J.N., et al., *Physical and welding metallurgy of Gd-enriched austenitic alloys for spent nuclear fuel applications - part II: Nickel-based alloys - tests proved Gd-enriched Ni-based alloys are excellent candidates for use in storing spent nuclear fuels.* Welding Journal, 2004. **83**(12): p. 319S-329S.
56. Grigorev, Y.Y., V.E. Saenko, and N.A. Shostak, *ACCELERATED METHOD FOR HOT CRACK TESTING OF WELD METAL.* Welding Production, 1969. **16**(2): p. 88-&.
57. Perfilev, A.N. and T.A. Chernyshova, *COMPARISON OF METHODS OF ASSESSING HOT CRACKING SUSCEPTIBILITY OF WELD METAL.* Welding Production, 1976. **23**(12): p. 52-56.
58. Kou, S., *A criterion for cracking during solidification.* Acta Materialia, 2015. **88**: p. 366-374.
59. Makhenko, V.I., *DEVELOPMENT OF HOT CRACKS ON COMPLETION OF HIGH SPEED ARC WELDING.* Automatic Welding Ussr, 1967. **20**(8): p. 6-&.
60. Dahl, W., C. Duren, and H. Musch, *EFFECT OF VARIOUS ALLOYING ELEMENTS ON SUSCEPTIBILITY TO HOT CRACKS OF AN AUSTENITIC STEEL DURING WELDING.* Stahl Und Eisen, 1973. **93**(18): p. 813-822.
61. Lai, W.J. and J. Pan, *Failure mode and fatigue behavior of weld-bonded lap-shear specimens of magnesium and steel sheets.* International Journal of Fatigue, 2015. **75**: p. 184-197.
62. John, R. and W.G. Richards, *HOT CRACKING IN 5 PERCENT NICKEL STEEL WELD-METAL.* Metal Construction and British Welding Journal, 1972. **4**(4): p. 127-&.
63. Schempp, P., et al., *Weld Metal Grain Refinement of Aluminium Alloy 5083 through Controlled Additions of Ti and B.* Materials Testing, 2011. **53**(10): p. 604-609.
64. Kannengiesser, T., et al., *Analysis of welding reaction stresses and welding reaction moments in component tests - Stress characteristics dependent on the intensity of restraint*. Advances in Mechanical Behaviour, Plasticity and Damage, Vols 1 and 2, Proceedings, ed. D. Miannay, et al. 2000. 145-150.
65. Reddy, G.M., et al., *Effect of welding techniques on microstructure and mechanical properties of aluminium-lithium alloy welds*, in *Aluminium Alloys: Their Physical and Mechanical Properties, Pts 1-3*, E.A. Starke, T.H. Sanders, and W.A. Cassada, Editors. 2000. p. 1751-1756.

66. Korber, F., *Applicability of ideal law of mass action on metallurgical processes.* Naturwissenschaften, 1932. **20**: p. 409-412.
67. Korber, F. and E. Siebel, *On the theory of figurative changes of shape.* Naturwissenschaften, 1928. **16**: p. 408-412.
68. Pellini, W.S. and B.R. Queneau, *DEVELOPMENT OF TEMPER BRITTLENESS IN ALLOY STEELS.* Transactions of the American Society for Metals, 1947. **39**: p. 139-161.
69. Afshari, D., et al., *An approach in prediction of failure in resistance spot welded aluminum 6061-T6 under quasi-static tensile test.* Proceedings of the Institution of Mechanical Engineers Part B-Journal of Engineering Manufacture, 2012. **226**(B6): p. 1026-1032.
70. Bottger, B., et al., *Relationship Between Solidification Microstructure and Hot Cracking Susceptibility for Continuous Casting of Low-Carbon and High-Strength Low-Alloyed Steels: A Phase-Field Study.* Metallurgical and Materials Transactions a-Physical Metallurgy and Materials Science, 2013. **44A**(8): p. 3765-3777.
71. Wodie, J.C. and T. Levy, *NONLINEAR RECTIFICATION OF DARCY LAW.* Comptes Rendus De L Academie Des Sciences Serie Ii, 1991. **312**(3): p. 157-161.
72. Nacereddine, N., et al., *Weld defect detection in industrial radiography based digital image processing*, in *Proceedings of World Academy of Science, Engineering and Technology, Vol 2*, C. Ardil, Editor. 2005. p. 112-115.
73. Coniglio, N. and C.E. Cross, *Mechanisms for Solidification Crack Initiation and Growth in Aluminum Welding.* Metallurgical and Materials Transactions a-Physical Metallurgy and Materials Science, 2009. **40A**(11): p. 2718-2728.
74. Krantz, B.M. and Coppolec.Vd, *EFFECTS OF PULSED GAS METAL-ARC WELDING PARAMETERS ON WELD COOLING RATES.* Welding Journal, 1971. **50**(11): p. S474-&.
75. Vindt, B.F. and K.I. Zaitsev, *EFFECTS OF TECHNOLOGICAL PARAMETERS ON SHAPE OF PENETRATED ZONE IN HEATED TOOL WELDING OF THERMOPLASTIC SUBSTANCES.* Automatic Welding Ussr, 1969. **22**(10): p. 28-&.
76. Kou, S. and Y. Le, *GRAIN-STRUCTURE AND SOLIDIFICATION CRACKING IN OSCILLATED ARC WELDS OF 5052 ALUMINUM-ALLOY.* Metallurgical Transactions a-Physical Metallurgy and Materials Science, 1985. **16**(7): p. 1345-1352.
77. Goldak, J., et al., *HEAT AND FLUID-FLOW IN WELDS*. Advanced Joining Technologies, ed. T.H. North. 1990. 69-82.

78. Sun, J.S., C.S. Wu, and Y.M. Zhang, *Heat transfer modeling of double-side arc welding.* Acta Physica Sinica, 2002. **51**(2): p. 286-290.
79. Winkler, C., et al., *Effect of surfactant redistribution on weld pool shape during gas tungsten arc welding.* Science and Technology of Welding and Joining, 2000. **5**(1): p. 8-20.
80. Goldak, J., et al., *Predicting Distortion and Residual Stress in Complex Welded Structures by Designers*. Trends in Welding Research, Proceedings, ed. S.A. David, et al. 2006. 531-539.
81. Bonifaz, E.A., *Finite element analysis of heat flow in single-pass arc welds.* Welding Journal, 2000. **79**(5): p. 121S-125S.
82. Arribas, I., J.M. Martin, and F. Castro, *The initial stage of liquid phase sintering for an Al-14Si-2.5Cu-0.5Mg (wt%) P/M alloy.* Materials Science and Engineering a-Structural Materials Properties Microstructure and Processing, 2010. **527**(16-17): p. 3949-3966.
83. Makino, T., et al., *Effect of defect shape on rolling contact fatigue crack initiation and propagation in high strength steel.* International Journal of Fatigue, 2016. **92**: p. 507-516.
84. Helfen, L., et al., *Laminographic imaging using synchrotron radiation - challenges and opportunities*, in *11th International Conference on Synchrotron Radiation Instrumentation*, J. Susini and P. Dumas, Editors. 2013.
85. Cecilia, A., et al., *High resolution 3D imaging of bump-bonds by means of synchrotron radiation computed laminography.* Journal of Instrumentation, 2013. **8**.
86. Helfen, L., et al., *Synchrotron and neutron laminography for three-dimensional imaging of devices and flat material specimens.* International Journal of Materials Research, 2012. **103**(2): p. 170-173.
87. Griesche, A., E. Dabah, and T. Kannengiesser, *Neutron imaging of hydrogen in iron and steel.* Canadian Metallurgical Quarterly, 2015. **54**(1): p. 38-42.
88. Griesche, A., et al., *Three-dimensional imaging of hydrogen blister in iron with neutron tomography.* Acta Materialia, 2014. **78**: p. 14-22.
89. Lindgren, E. and H. Wirdelius, *X-ray modeling of realistic synthetic radiographs of thin titanium welds.* Ndt & E International, 2012. **51**: p. 111-119.
90. D. Shiozawa, N. Nakai, T. Kurimura, Y. Morikage, H. Tanaka, H. Okado, T. Miyashita, K. Kajiwara, Observation of Cracks in Steels Using Synchrotron Radiation X-ray Micro Tomography, Journal of the Society of Materials Science, Japan, Vol. 56, No. 10, 2007 951-957.

91. Ewert, U., et al., *First experience with luminescence imaging plates in industrial radiography and comparison to the film*. 4th International Conference of Slovenian Society for Nondestructive Testing - Application of Contemporary Nondestructive Testing in Engineering, Conference Proceedings, ed. J. Grum. 1997. 115-120.
92. Moreira, E.V., et al., *Digital Radiography Using Digital Detector Arrays Fulfills Critical Applications for Offshore Pipelines.* Eurasip Journal on Advances in Signal Processing, 2010.
93. Zscherpel, U., U. Ewert, and M. Jechow, *CONCEPTS FOR EVALUATION OF IMAGE QUALITY IN DIGITAL RADIOLOGY*, in *Review of Progress in Quantitative Nondestructive Evaluation, Vols 31a and 31b*, D.O. Thompson and D.E. Chimenti, Editors. 2012. p. 589-596.
94. Graeve, T. and G.P. Weckler, *High-resolution CMOS imaging detector*, in *Medical Imaging 2001: Physics of Medical Imaging*, L.E. Antonuk and M.J. Yaffe, Editors. 2001. p. 68-76.
95. Kim, H.K., et al., *Development and evaluation of a digital radiographic system based on CMOS image sensor.* Ieee Transactions on Nuclear Science, 2001. **48**(3): p. 662-666.
96. Ewert, U., et al., *New Compensation Principles for Enhanced Image Quality in Industrial Radiology with Digital Detector Arrays.* Materials Evaluation, 2010. **68**(2): p. 163-168.
97. Dolby, R.E., et al., *Welds, their quality and inspection ability for high integrity structures and components*. Fracture, Plastic Flow and Structural Integrity, ed. P. Hirsch and D. Lidbury. 2000. 45-63.
98. Ewert, U., H. Heidt, and D. Schnitger, *New European standards in industrial radiology*. Trends in Nde Science and Technology - Proceedings of the 14th World Conference on Ndt, ed. C.G.K. Nair, et al. 1996. 1901-1904.
99. Zhang, D.H., et al., *Accurate and efficient calibration method for a selenium flat-panel detector-based volume tomographic angiography imaging system*, in *Medical Imaging 1999: Physics of Medical Imaging, Pts 1 and 2*, J.M. Boone and J.T. Dobbins, Editors. 1999. p. 626-636.
100. Bavendiek, K. and U. Zscherpel, *Limits of radiographic testing - New high contrast sensitivity technique - Examples and analysis by system theory.* Materialprufung, 2007. **49**(11-12): p. 610-616.
101. Ewert, U., et al., *Image Quality in Digital Industrial Radiography.* Materials Evaluation, 2012. **70**(8): p. 955-964.

102. Hasenkamp, F.A., *RADIOGRAPHIC LAMINOGRAPHY.* Materials Evaluation, 1974. **32**(8): p. 169.
103. Lovejoy, C.O. and A.H. Burstein, *GEOMETRICAL PROPERTIES OF BONE SECTIONS DETERMINED BY LAMINOGRAPHY AND PHYSICAL SECTION.* Journal of Biomechanics, 1977. **10**(9): p. 527-528.
104. Bolliger, B. and M. Stewart, *X-ray laminography improves functional-test yield.* Ee-Evaluation Engineering, 1996. **35**(11): p. 40-41.
105. Gondrom, S., et al., *X-ray computed laminography: an approach of computed tomography for applications with limited access.* Nuclear Engineering and Design, 1999. **190**(1-2): p. 141-147.
106. Cmar-Mascis, N.A., W.P. Winfree, and F.R. Parker, *Advanced radiographic methods for visualization of corrosion in aircraft structures*, in *Nondestructive Evaluation of Aging Aircraft, Airports, and Aerospace Hardware Iii*, A.K. Mal, Editor. 1999. p. 332-341.
107. Ewert, U., V. Baranov, and K. Borchardt, *Cross-sectional imaging of building constructions by new non-linear tomosynthesis techniques using imaging plates and Co-60-radiation*. Nondestructive Testing in Civil Engineering - 1995 International Symposium, Vols 1 & 2, International Symposium, ed. G. Schickert and H. Wiggenhauser. 1995. 1267-1274.11
108. Fu, J., et al., *Computed Laminography Imaging Inspection Method for Aeronautical Plate and Shell Components*. Istm/2009: 8th International Symposium on Test and Measurement, Vols 1-6, ed. T.D. Wen. 2009. 1932-1935.
109. Helfen, L., et al., *Neutron laminography-a novel approach to three-dimensional imaging of flat objects with neutrons.* Nuclear Instruments & Methods in Physics Research Section a-Accelerators Spectrometers Detectors and Associated Equipment, 2011. **651**(1): p. 135-139.
110. Chlewicki, W., et al., *CLASSIFICATION PROCEDURE IN LIMITED ANGLE TOMOGRAPHY SYSTEM*, in *Review of Progress in Quantitative Nondestructive Evaluation, Vols 30a and 30b*, D.O. Thompson and D.E. Chimenti, Editors. 2011. p. 1613-1619.
111. Cho, Z.H., I.S. Ahn, and C.M. Tsai, *COMPUTER ALGORITHMS AND DETECTOR ELECTRONICS FOR TRANSMISSION X-RAY TOMOGRAPHY.* Ieee Transactions on Nuclear Science, 1974. NS21(1): p. 218-227.

112. Bajpai, M., P. Gupta, and P. Munshi, *Fast multi-processor multi-GPU based algorithm of tomographic inversion for 3D image reconstruction.* International Journal of High Performance Computing Applications, 2015. **29**(1): p. 64-72.
113. Zhou, J., et al., *Computed laminography for materials testing.* Applied Physics Letters, 1996. 68(24): p. 3500-3502.
114. Kroupa, M. and J. Jakubek, *High contrast laminography using iterative algorithms.* Journal of Instrumentation, 2011. **6**.
115. Hebert, T.J., S.S. Gopal, and Ieee, *AN IMPROVED FILTERED BACK-PROJECTION ALGORITHM USING PREPROCESSING*. Conference Record of the 1991 Ieee Nuclear Science Symposium and Medical Imaging Conference, Vols 1-3. 1991. 2068-2072.
116. Kruger, R.P. and J.R. London, *THE INDUSTRIAL USE OF FILTERED BACK PROJECTION AND MAXIMUM-ENTROPY RECONSTRUCTION ALGORITHMS.* Materials Evaluation, 1982. **40**(12): p. 1285-&.
117. Xu, X.L., J.S. Liow, and S.C. Strother, *A NONITERATIVE LINEAR ALGEBRAIC ALGORITHM FOR IMAGE-RECONSTRUCTION*. Conference Record of the 1992 Ieee Nuclear Science Symposium and Medical Imaging Conference, Vols 1 and 2, ed. G.T. Alley. 1992. 1198-1200.
118. Fieker, C. and C. Friedrichs, *On reconstruction of algebraic numbers*, in *Algorithmic Number Theory*, W. Bosma, Editor. 2000. p. 285-296.
119. Delaney, A.H. and Y. Bresler, *A fast and accurate Fourier algorithm for iterative parallel-beam tomography.* Ieee Transactions on Image Processing, 1996. **5**(5): p. 740-753.
120. Kazantsev, I.G. and S.O.C. Ieee Signal Proc, *A new formula of the radon transform inversion*. International Conference on Image Processing - Proceedings, Vol I. 1997. 189-191.
121. Clarkson, E., *Projections onto the range of the exponential Radon transform and reconstruction algorithms.* Inverse Problems, 1999. **15**(2): p. 563-571.
122. Klebanov, L.B. and S.T. Rachev, *Computer tomography and quantum mechanics.* Advances in Applied Probability, 1997. **29**(3): p. 595-606.
123. Hawkins, W.G., *Fourier transform resampling: Theory and application.* Ieee Transactions on Nuclear Science, 1997. **44**(4): p. 1543-1551.
124. Gustafsson, B., *Mathematics for computer tomography.* Physica Scripta, 1996. **T61**: p. 38-43.

125. Placidi, G., et al., *Fourier reconstruction as a valid alternative to filtered back projection in iterative applications: Implementation of Fourier spectral spatial EPR imaging.* Journal of Magnetic Resonance, 1998. **134**(2): p. 280-286.
126. Robert-Coutant, C. and A. Marc, *Introduction to reconstruction methods*. X-Ray Tomography in Material Science, ed. J. Baruchel, et al. 2000. 61-75.
127. Manzoor, M.F., et al., *Image reconstruction of simulated specimens using convolution back projection.* Defence Science Journal, 2001. **51**(2): p. 175-187.
128. Lu, W.G. and T.R. Mackie, *Tomographic motion detection and correction directly in sinogram space.* Physics in Medicine and Biology, 2002. **47**(8): p. 1267-1284.
129. Chen, L.G., et al., *A novel method for reducing high attenuation object artifacts in CT reconstructions*, in *Medical Imaging 2002: Image Processing, Vol 1-3*, M. Sonka and J.M. Fitzpatrick, Editors. 2002. p. 841-850.
130. Goddard, I. and M. Trepanier, *High-speed cone-beam reconstruction: an embedded systems approach*, in *Medical Imaging 2002: Visualization, Image-Guided Procedures, and Display*, S.K. Mun, Editor. 2002. p. 483-491.
131. THIESSENHUSEN, K.U., EWERT, U., REDMER, B. and BAVENDIEK, K., 2011. Geometric Corrections in Coplanar Translational Laminography. In *International Symposium on Digital Industrial Radiology and Computed Tomography, Berlin*.
132. https://www.vareximaging.com/products/flat-panel-detectors/1512
133. https://www.volumegraphics.com
134. http://www.vision-in-x.com
135. https://fiji.sc

List of Figures

List of Tables

Appendix A: Real-time acquisition Script used by ISee! Professional

```
-- This script is designed for high-speed acquisition
--Image series using ISee! Professionals Acquisition Center.
-- Execute using "dofile" command, e.g.:
--dofile( " Image_Aquisition_Manipulator_control.txt" )
FRAME_TIME = 0
AVERAGING = 0
IMAGES = 0
DEST_DIR = "----- "
NAME_PREFIX = "-----"
-- EXPERT CODE UNDER THIS LINE
---------- STEPPER MOTOR CONTROLS AND WELD TORCH ----------
-----StepperMotor Parameters----------
 serial_open{ port="COM1" , speed=9600 , data_bits="Data8" , parity="NoParity" ,
stop_bits="OneStop" }
--serial_open{ port="COM6" , speed=115200 , data_bits="Data8" , parity="NoParity" ,
stop_bits="OneStop" }
speed = "bits_per_seconds",
--data_bits ="Data5"|"Data6"|"Data7"|"Data8"|"UnknownDataBits",
--parity = "NoParity"|"EvenParity"|"OddParity"|"SpaceParity"|"MarkParity"|"UnknownParity",
--stop_bits="OneStop"|"OneAndHalfStop"|"TwoStop"|"UnknownStopBits" } - Open the serial
port
--specified by the "port" parameter.
--serial_send{ port="COM1" , message="@01\\r" }
--serial_send{ port="COM1" , message="@0i\\r" }--- initialization
--serial_send { port="COM1" , message="@0M  10,3000\\r" }
open_imager{ index=0, signal="opened" }
wait{ signal="opened", interval=15 }
setup_acquisition{ frame_duration=FRAME_TIME, averaging=AVERAGING,
sequence_size=1, preview="off", autostart="off" }
close_all_images{}
wait{ signal="*", interval = 1, granularity=1 }
--serial_send{ port="COM1" , message="@0M 25000,3000\\r" } -- motion to initialposition
--serial_send{ port="COM1" , message="@0M -38000,400\\r" } -- for motion to "max"
--serial_send{ port="COM6" , message="R0=2\\r" }
--serial_send{ port="COM6" , message="P0.1=1\\r" } --switch on
--serial_send{ port="COM1" , message="@0M -26000,300\\r" } -- for motion to "max"
serial_send{ port="COM1" , message="@0A -26000,150,-20000,150\\r" }
start_time = time{}
--start_acquire{ name=NAME_PREFIX, signal="ready", show="no", keep_running=IMAGES }
--for i = 0, IMAGES-1 do
--  im_name = NAME_PREFIX..i
--  wait{ signal="ready", interval = 100*FRAME_TIME }
--  save_image{ image=im_name.."#0", file=DEST_DIR..im_name..".vff", format="VFF",
preserve_meta="yes" }
--  close_image{ id=im_name }
--end
-- All-In-One approach
```

```
--setup_acquisition{ gain=1, frame_duration=FRAME_TIME, averaging=1, calibration="off",
preview="no", autostart="no", sequence_size=IMAGES, sequence_mode="stack" }
--start_acquire{ name=NAME_PREFIX, signal="fin", show="no" }
--wait{ signal="fin" }
--finish_time = time{}
--save_image{ image=NAME_PREFIX.."#0", file=DEST_DIR..NAME_PREFIX..".tif",
format="TIFF" }
--close_image{ id=NAME_PREFIX }
--print( "Acquision of "..IMAGES.." images" )
--print( "started  at: "..start_time )
--print( "finished at: "..finish_time )
--close_imager{}
--show{ message="Finished" }
--serial_close{ port="COM1" }
--serial_close{ port="COM6" }
-- acquire sequence and store separate images
setup_acquisition{ gain=1, frame_duration=FRAME_TIME, averaging=1, calibration="off",
preview="no", autostart="no", sequence_size=IMAGES, sequence_mode="separate" }
start_acquire{ name=NAME_PREFIX, signal="fin", show="no" }
wait{ signal="fin" }
finish_time = time{}
for i = 0, IMAGES-1 do
  save_image{ image=NAME_PREFIX.."#"..i, file=DEST_DIR..NAME_PREFIX.."-"..i..".tif",
format="tif" }
end
close_all_images{}
print( "Acquision of "..IMAGES.." images" )
print( "started  at: "..start_time )
print( "finished at: "..finish_time )
close_imager{}
show{ message="Finished" }
serial_close{ port="COM1" }
--serial_close {port="COM6" }
-----------------Move to Starting Position--------------
Reset = show{ question="Continue (y/n)?" }
if Reset == "yes" then
  serial_open{ port="COM1" , speed=9600 , data_bits="Data8" , parity="NoParity" ,
stop_bits="OneStop" }
  --serial_send{ port="COM1" , message="@0R1\\r" }
  --serial_send{ port="COM1" , message="@01\\r" }
  --serial_send{ port="COM1" , message="@0M 10,3000\\r" }
  --serial_send{ port="COM1" , message="@0M 26000,1000\\r" }
serial_send{ port="COM1" , message="@03\\r" }
serial_send{ port="COM1" , message="@0R3\\r" }
serial_send{ port="COM1" , message="@0A 26000,1000,20000,1000\\r" }
  wait{ interval=3, granularity=10 }
  serial_close{ port="COM1" }
end
-- EOF
```

Appendix B: Detector Adjustment Script used by ISee! Professional

```
-- This script is used to adjust the detector using a set of images inside a directory.
-- To use it one precondition is needed: The image name must contain an index counter.
-- Execute using "dofile" command, e.g.:
-- dofile ( "" )
-- USER SPECIFIED PARAMETERS
SOURCE_DIR = "--/"
DEST_DIR = "--/"
IMAGE_NAME = "--"
IMAGE_INDEX_FIRST = ---
IMAGE_INDEX_LAST = --
IMAGE_EXTENSION_IN = "tif"
IMAGE_EXTENSION_OUT = "TIFF"
CALIBRATION_FILE = ""
-- iterate index
For index = IMAGE_INDEX_FIRST, IMAGE_INDEX_LAST do
-- *** load image ***
  -- build current file name
  current_file = IMAGE_NAME .. tostring(index) .. "." .. IMAGE_EXTENSION_IN
  current_file_full_path = SOURCE_DIR .. "/" .. current_file
  -- print( "current_file: " .. current_file ) -- debug code
--  print( "current_file_full_path: " .. current_file_full_path ) -- debug code
  load_image{ file=current_file_full_path } -- Load image(s) from the file.
-- *** apply calibration ***
  adjust_pixels{ config=CALIBRATION_FILE, image=current_file_full_path.."#0" } -- apply
detector calibration and do bad pixel detection/correction.
-- *** save calibrated image ***
  current_file_full_path_out = DEST_DIR .. "/" .. current_file
  -- image is the full path! + #0...#n (the modifacation index)
  save_image{ image=current_file_full_path.."#1", file=current_file_full_path_out,
format=IMAGE_EXTENSION_OUT } -- save_image{ [image==<image_id>,] file=<filename>,
format=<format> } - Save the image version specified by the optional "image" parameter.  If
this parameter is missing then the command aplies to the image currently active.
-- *** close all images ***
--  print( "current_file: " .. current_file )
  close_image{ id=current_file_full_path.."#1" }
  close_image{ id=current_file_full_path.."#0" }
  --print( "CALIBRATION COMPLETE" )
  --wait{interval=5}
end
-- EOF
```

Appendix C: Reconstruction configuration file (TomoPlan)

```
--(C) Bundesanstalt für Materialforschung und -prüfung
debuglevel=2
width=645
height=1872
pixelsize=0.075
nproj=1600
nbatches=1
slicez0=35.5
nslices=60
slicezdist=0.1
stride=1
SourceZ=970
SourceY1= +460.8
SourceY2= -46
#crop_t=10
#crop_b=10
#filetype=FLD
# FLD16 files: 16bit unsigned
#datatype=uint16
# big endian
#endian=BE
# scan direction x
flipxy=true
# 2048 bytes ignorieren (fld)
#inputskip=2048
first_proj=1
write_filtered=false
enable_filtering=true
enable_interpolation=true
enable_hammingwindow=false
enable_normalize=true
enable_halfprecision=false
input_prefix=D:\Bead_on_plate_welds\3.6mm_per_Sec\3mm_ALMgSi\3mm_ALMgSi_B_Y_a
xis
numberwidth=0
input_suffix=.tif
#input_suffix=.fld
filter_prefix=filtered/HammingTest
output_prefix=D:\Reco\Bead-on-
platewelds\3.6mm_per_Sec\3mm_ALMgSi_B_Y_axis\reko_B
single_file=false
ofiletype=TIFF
debuglevel=1
multitex=16
```